Searches for Dark Matter

by

Daniel James Phalen

A dissertation submitted in partial fulfillment
of the requirements for the degree of
Doctor of Philosophy
(Physics)
in The University of Michigan
2010

Doctoral Committee:

Assistant Professor Aaron Thomas Pierce, Chair
Professor Dante Eric Amidei
Professor Gordon L. Kane
Associate Professor Leopoldo A. Pando-Zayas
Assistant Professor Oleg Y. Gnedin

A.M.D.G.

ACKNOWLEDGEMENTS

I would like to thank my advisor, Aaron Pierce, for his guidance and collaborations. It has been a pleasure working with him for these past four years.

I would like to thank my collaborators for these projects. On the second chapter, Gordon Kane, Aaron Pierce, Phill Grajek, and Scott Watson co-authored the paper. On the third chapter Aaron Pierce and Tim Cohen co-authored the paper. On the fourth chapter Aaron Pierce and Neal Weiner co-authored the paper. Finally, on the fifth chapter Manoj Kaplinghat and Kathryn Zurek co-authored the paper. I would to thank my other collaborators for projects not included in this thesis: James Wells, Leopoldo Pando-Zayas, Brooks Thomas, Tom Flacke, Arjun Menon, Cesar Terrero, Teng Jiag Khoo, Michael Gerbush, and David Tucker-Smith.

I would like to thank Finn Larsen and Eric Kuflik for their conversations.

I would of course like to thank my beloved wife for all her help, especially her concise explanations of what I do. I would also like to thank my parents for their love and support, without which I would not have gotten to where I am now.

TABLE OF CONTENTS

LIST OF FIGURES

Figure

LIST OF APPENDICES

Appendix

CHAPTER I

Introduction

The Standard Model (SM) is a fantastically successful model of particle physics. It has passed every laboratory test to date. However, we know that it is not the end of the story. Dark matter (DM) makes up 80% of the matter in our universe and is unaccounted for in the SM. Discovering the nature of DM is the focus of this thesis.

In 1933, Fritz Zwicky observed that the velocities of galaxies in the Coma cluster far exceeded the velocities expected based on the gravitational potential of the luminous matter [224]. He postulated the existence of a non-luminous matter that made up the remaining mass of the cluster. Since then, numerous other studies have pointed to the existence of dark matter: rotation curves of stars in galaxies [194], gravitational lensing studies [213], and temperature fluctuations of the cosmic microwave background (CMB) [144]. The WMAP experiment, which maps the CMB, provides the best value for the dark matter (DM) relic density [144],

$$\Omega_{\rm DM}\, h^2 = 0.1131 \pm 0.0034. \tag{I.1}$$

Separate measurements of the baryon density show that this cannot be baryons. While a host of astrophysical measurements have precisely determined the amount of dark matter in our universe, we do not yet know its identity. At present one could imagine that the dark matter is a Weakly Interacting Massive Particle (WIMP), an axion, or something

more exotic. This situation could change, perhaps soon.

In this thesis we will focus on WIMP dark matter candidates and their prospect for detection. There are three different ways of searching for a WIMP: collider experiments, direct detection, or indirect detection. In collider experiments, one collides standard model particles in a laboratory setting. Most of the resulting particles will be picked up in a detector. Since a WIMP will not interact with the detector, the result is missing transverse momentum in the detector. Thus we infer the WIMP was created in the collision. In direct detection experiments one looks for evidence of dark matter scattering off of a nucleus. In indirect detection experiments, one looks for cosmic rays created by dark matter annihilations in our galaxy.

1.1 Thermal Relic Abundance vs. Non-thermal relic Abundance

Assuming the universe is in thermal equilibrium at the time the dark matter decouples from the thermal bath, a stable particle with a weak scale mass and weak interaction cross section provides the correct order of magnitude of the relic density [147]. This has been dubbed the "Wimp Miracle". We will briefly review the argument for thermal matter relics (see [143, 132] for a detailed review).

The evolution of a species in the thermal bath of the early universe obeys the Boltzman equation

$$\frac{dn_\chi}{dt} + 3Hn_\chi = -\langle\sigma_A|v|\rangle(n_\chi^2 - n_{eq}^2), \tag{I.2}$$

where n_χ is the number density of WIMPs particles per co-moving volume, H is the Hubble "constant", $\langle\sigma_A|v|\rangle$ is the thermally averaged annihilation cross section, and n_{eq} is the equilibrium number density. The second term on the left hand side of equation I.2 describes the dilution due to the expansion of the universe and the right hand side works

to restore equilibrium. The annihilation rate is given by $\Gamma_{ann} = \langle \sigma_A |v| \rangle n_\chi$. When

$$\Gamma_{ann}(T_f) \approx H(T_f), \tag{I.3}$$

the dark matter stops tracking its equilibrium value, or "freezes out". Using the freeze out condition we can solve for the freeze out temperature T_f, which for weak scale inputs has $T_f \approx m_\chi/20$. Then using this temperature we can solve for the co-moving number density at freeze out. The Hubble constant as a function of temperature is $H = 1.66 g_*^{1/2} T^2/m_{Planck}$. Since the ratio of co-moving number density to entropy is approximately constant as the universe cools, use the entropy as a function of temperature, $s \approx 0.4 g_* T^3$, to solve for the number density today

$$\begin{aligned} \left(\frac{n_\chi}{s}\right)_{today} &= \left(\frac{n_\chi}{s}\right)_f = \\ &\approx \frac{10^2}{m_\chi m_{Planck} g_*^{1/2} \langle \sigma_A v \rangle}. \end{aligned} \tag{I.4}$$

Finally, we convert the number density today to units of the critical density, $\rho_c = 10^{-5} h^2$ GeV cm^{-3}, using the entropy today $s \approx 4000\ cm^{-3}$

$$\Omega_{DM} h^2 = \frac{m_\chi n_\chi}{\rho_c} \approx 0.1 \left(\frac{3 \times 10^{-26}\ \mathrm{cm}^3/\mathrm{s}}{\langle \sigma_A |v_f| \rangle} \right), \tag{I.5}$$

where $v_f = 1/\sqrt{20}$ at freeze out. These approximations are usually accurate to about 10%. So requiring a thermal relic density for the dark matter constrains the annihilation cross section.

A particle without the correct thermal relic abundance can still be the dark matter. For example, a late time injection of entropy into the thermal bath can dilute the relic abundance [195]. A particle surviving to the time of freezout can annihilate with the dark matter to decrease the relic density [110]. A particle that decays to the dark matter after the dark matter freezes out can increase the relic abundance [165], or the late time decay of a moduli field that reheats the universe could set the relic abundance [98].

While there does exist a WIMP miracle, one should realize that the DM need not be thermal relic. The relic abundance could depend on the details of the model.

1.2 Supersymmetry and Dark Matter

The first two chapters of this thesis will focus on detection of supersymmetric dark matter candidates. In supersymmetry (for a review, see [111, 160]), every SM particle has a partner of opposite statistics. These opposite spin partners, called superpartners, stabilize the weak scale against quantum corrections.

In the Standard Model baryon and lepton number are accidental symmetries resulting from the particle content and gauge symmetries. In supersymmetric versions of the Standard Model, baryon and lepton number violating operators are allowed. To forbid operators dangerous for proton decay, a discrete $\mathbb{Z}_2$ symmetry called R-parity is imposed. All superpartners are odd under R-parity, and so the lightest superpartner (LSP) is stable. If neutral, this can serve as a dark matter candidate.

In the minimal supersymmetric standard Model (MSSM), a favored dark matter candidate is a neutralino LSP. It is a mixture of the superpartners of the Higgs boson, Z boson, and photon. It is neutral and weakly interacting, and therefore can realize the WIMP miracle. At colliders they would appear as missing energy in the decays of the superpartner of the gluon (gluino) or any of the quark partners (squarks).

1.3 Indirect Detection

Recently there has been a lot of attention on indirect signals of DM annihilations. In many models, the DM is its own antiparticle and annihilates with itself. This is expected to produce equal numbers of particles and antiparticles. Since most astrophysical processes favor matter over antimatter, the products of these dark matter annihilations in the galaxies would produce an antiparticle signal in cosmic rays. Recently there have been observations

of an excess of high energy cosmic ray positrons and electrons. The excess was originally observed by the HEAT [39, 41] and AMS [11] experiments, and was confirmed more recently by the PAMELA [9, 8] and PPB-BETs [212] experiments. The Fermi Large Area Telescope also observes excess cosmic ray electrons and positrons over the predicted background [3], though their excess is not nearly as large as that observed by ATIC [56] (and seems to indicate that the ATIC excess is instrumental in origin). These anomalies are very exciting, and have cause a lot of activity in the field.

Interpreted as a dark matter signal, the PAMELA result places strong constraints on annihilation channels. The sharp rise indicates a hard lepton spectrum [68, 66], while the lack of an accompanying rise in the $\bar{p}/p$ ratio strongly constrains hadronic annihilation modes [82]. Consequently, if PAMELA results are taken at face value, the dark matter particle annihilates primarily to leptons — hadronic channels are suppressed. These conclusions can be avoided by using a non-standard propagation model [108] or multiple contributions combining to make up each anomaly [134].

There exist other searches that are much more dependent upon the astrophysical backgrounds. While we will not focus on them in the paper due to the astrophysical uncertainties, for reference they are radio observations of the Galactic center and gamma rays from the Galactic center and Galactic ridge [68, 47].

Other cosmological searches include fits to the ionization depth of the surface of last scattering [201](which constrain how much ionization power is injected into the plasma and the time of recombination), and diffuse gamma rays from halo formation at earlier times [187].

1.4 Direct Detection

A particle with weak interactions can interact through weak force carriers with the Standard Model. Direct detection experiments attempt to capitalize on this by looking

for dark matter particles passing through the earth scattering off of nuclei [107, 85]. They are buried deep underground to eliminate backgrounds from other cosmic rays. There are two types of interactions that are relevant for this dissertation. Spin-independent (SI) scattering is where the dark matter couples to the mass of the nucleus. Spin-dependent (SD) scattering is where the dark matter couples to the spin of the nucleus.

The operator responsible for SI DM-nucleus interactions is

$$\mathcal{O}_q^{SD} = c_q(\bar{\chi}\chi)(\bar{q}q). \tag{I.6}$$

SI scattering with a nucleus gets a A^2 enhancement, where A is the nuclear atomic number. Due to this enhancement, heavier target nuclei are favored when searching for spin independent scattering, and the bounds on SI scattering are very strong.

The operator responsible for SD DM-nucleus interactions is

$$\mathcal{O}_q^{SD} = d_q(\bar{\chi}\gamma^\mu\gamma^5\chi)(\bar{q}\gamma_\mu\gamma^5 q). \tag{I.7}$$

Since this axial coupling to the quarks gets no enhancement from large spin, the bounds on the SD cross section are weak compared to the SI cross section. However, a new generation of larger experiments plans to push down the bounds on the SD cross section.

Many direct detection experiments are planning to release data in near future. The CDMS II [12] experiment and XENON10 [19] experiment are currently the most sensitive to SI scattering. For terrestrial experiments, PICASSO [37] and KIMS [148] are currently the most constraining for SD scattering off of protons, and XENON10 [18] is the most constraining for SD scattering off of neutrons.

1.5 Collider experiments

Finally, the Large Hadron Collider (LHC) is coming online. Protons are accelerated and collided with protons, with a design center of mass energy of 14 TeV. In these collisions a host of new particles are created and their energy and momenta are measured.

If in an event there is a large amount of unbalanced momentum that is transverse to the beam, conservation of momentum implies that another particle escaped out the other side undetected. If the escaping particles are stable on time scales of the universe, these missing transverse momentum events could be signals of dark matter being created in the laboratory.

For the LHC to provide complementary data on the dark matter[53, 31], it must be kinematically accessible. Often, the dark matter is most efficiently searched for in the cascade decays of colored particles. However, there can be a large gap between the dark matter mass and the lightest colored particle. In supersymmetric models with gaugino mass unification, there is roughly a factor of seven between the WIMP candidate mass and the gluino mass. In anomaly mediated models of supersymmetry breaking, the ratio is a factor of nine; in other models with non-universal gaugino masses, it can be a factor of a few. Thus, if the gluino is to be produced copiously (say with a mass less than 2 TeV), the dark matter should not be too heavy.

1.6 Outline

This thesis is based on five papers [109, 108, 71, 181, 139]

In Chapter 2 we will focus on indirect signals for a neutralino candidate that is composed primarily of Wino, the superpartner of the W gauge bosons. The preferred annihilation channel is the W^+W^-. Annihilations into gauge bosons produce antiprotons, so an non-traditional propagation model for cosmic rays is necessary to fit the PAMELA signal.

In Chapter 3 we will discuss direct detection of LSPs in the MSSM and comment on direct detection prospects for more general models of dark matter. We show that for an MSSM dark matter candidate, dark matter discovery in the next round of experiments is likely. This argument will rely on fine tuning arguments in the MSSM and thermal relic abundances.

In Chapter 4 we will discuss a model of dark matter that fits the PAMELA excesses in positrons while not overproducing antiprotons. This will consist of increasing the average yield of positrons relative to antiprotons in a given dark matter annihilation by having the dark matter annihilate to a new, heavy lepton. This lepton then decays to a light SM lepton and a gauge boson.

In Chapter 5 we will discuss possible astrophysical origins of the excesses in the WMAP haze. Pulsars are known to produce electron-positron pairs by gamma rays scattering in the strong magnetic fields. These are then accelerated to high energies in the magnetic field of the pulsar. The distribution of pulsars has been shown to be a possible origin of the PAMELA and Fermi excesses. We examine whether it can be shown to fit the WMAP haze.

In Chapter 6 we will conclude and discuss the outlook for the future experiments.

CHAPTER II

Indirect Detection of Supersymmetric Dark Matter

In this chapter, we will assume that the dark matter is a WIMP, in particular the lightest supersymmetric particle (LSP). The identity of the LSP depends on the details of supersymmetry breaking. Determining its identity will be a necessary step towards understanding the cosmological history of our universe, and an important clue towards the determination of the underlying theory. A phenomenologically attractive candidate is the lightest neutralino. We concentrate on a case that is both physically well-motivated and potentially gives large signals for dark matter indirect detection: a non-thermally produced LSP with large annihilation cross section. This scenario does not require additional anomalously large astrophysical "boost factors" to produce interesting signals.

By now, a large literature on the indirect detection of dark matter exists. For reviews, see [132, 122]. We will place particular emphasis on a dark matter interpretation of positrons, for earlier work on this subject see, e.g., [32, 137, 136, 34, 33, 188].

2.0.1 Thermal vs. Non-Thermal Production

Often, SUSY dark matter candidates are assumed to be produced from the primordial thermal plasma in the early stages of the universe (see e.g. [132] for a review). Under this assumption, the relic density of the LSP depends inversely on the annihilation cross

section. For a neutralino, χ, one finds [216, 143]:

$$\Omega_\chi h^2 \approx 0.1 \left(\frac{3 \times 10^{-26} \mathrm{cm}^3 \mathrm{s}^{-1}}{\langle \sigma_A v \rangle} \right) \tag{II.1}$$

For the case of a light neutralino LSP (a few hundred GeV or less), this typically restricts the neutralino to have a substantial bino component as pure wino and Higgsino states (co)-annihilate very effectively to weak gauge bosons. But precisely because of the smaller annihilation cross section, the annihilation signals from bino-like dark matter can be disappointingly small unless one appeals to large "boost factors." This issue is further exacerbated by the fact that bino annihilations are p-wave suppressed in the early universe, and are thus suppressed by powers of the final state masses today. If, as is often the case, the final state is b-quarks, the annihilation rate in our galaxy can be very small.

Models with gaugino mass unification often do typically give rise to a bino LSP, with its associated small annihilation cross section. One is then challenged to reduce the relic density to the observed value. However, if one does not assume a simple unification of gaugino masses at the high scale, other possibilities arise, well-motivated by top-down models of supersymmetry breaking. One attractive possibility is a wino LSP. This naturally occurs in theories where anomaly mediation gives the dominant contribution to the gaugino masses[191, 103]. It also occurs in string compactifications, see, e.g. [5]. This type of dark matter can also occur in the simplest models of split-supersymmetry [23, 102, 22, 214], where the gauginos get anomaly mediated masses (with attendant loop suppression), but scalars receive large masses, suppressed only by the Planck scale.

A light wino has a large annihilation cross section,

$$\begin{aligned} \langle \sigma_A v(\chi\chi \to W^+W^-) \rangle &= \frac{g^4}{2\pi} \frac{1}{m_\chi^2} \frac{\left(1 - \frac{m_W^2}{m_\chi^2}\right)^{3/2}}{\left(2 - \frac{m_W^2}{m_\chi^2}\right)^2} \\ &\approx 2 \times 10^{-24} \frac{cm^3}{s^{-1}} \left(\frac{200 \text{ GeV}}{m_\chi} \right)^2 , \end{aligned} \tag{II.2}$$

which is good for indirect detection, but also implies a small thermal relic abundance. The solution to recovering the correct relic abundance comes from non-thermal production. Often, the very same models that predict a wino LSP also provide mechanisms by which the LSP is produced non-thermally. If particles decay into the wino below its freeze-out temperature, this can provide the correct relic abundance[135]. Excellent candidates for the decaying particle include gravitinos and weakly coupled moduli [165, 104, 6]. Non-thermal production of dark matter leads to WIMPs with larger cross sections, since the standard thermal relic abundance calculation no longer applies. Since the flux of anti-particles coming from dark matter annihilations depends linearly on the cross section, this implies that non-thermal production of dark matter may lead to larger fluxes that may be detectable in future indirect experiments.[1]

In the remainder of the chapter, we review elements that enter any discussion of the indirect detection of dark matter. First, we briefly review basics of cosmic ray propagation, as well as the form of the source term arising from dark matter annihilation. We then discuss constraints from both anti-protons and synchrotron radiation. We then discuss prospects for observations of non-thermally produced wino dark matter in positrons and gamma rays. Throughout, we attempt to point out where astrophysical assumptions enter.

2.1 Cosmic Rays

2.1.1 Production

Our emphasis will be on the identification of high energy cosmic rays from dark matter annihilation. However, disentangling this component relies on an understanding of the other components of cosmic rays. Cosmic rays can be observed directly, e.g. from supernova ejecta (primaries). Alternately, these cosmic rays can interact with the interstellar medium producing secondaries. Both components contribute to the cosmic ray background, and

[1] While we will concentrate on wino dark matter, the results are a bit more general. In the region of interest, the winos annihilate nearly exclusively to W bosons. So, basically what we are probing is a dark matter candidate that annihilates to W's with a given cross section.

typically have a flux that is a power-law as a function of their kinetic energy. This is an anticipated property of cosmic rays of astrophysical origin.

The annihilation products of a dark matter particle will be associated with a given energy scale (its mass), and thus can conceivably be distinguished from power law backgrounds. These annihilations will act as a source term:

$$Q = \frac{1}{2}\left(\frac{\rho(r)}{m_\chi}\right)^2 \langle\sigma v\rangle \frac{dN}{dp}(p), \tag{II.3}$$

where $\rho(r)$ is the dark matter profile, and $\frac{dN}{dp}(p)$ is the spectrum of stable particles resulting from the annihilation. We simulated $\frac{dN}{dp}(p)$ using PYTHIA [200] and altered the dark matter source code in GALPROP[205] to accept this as input.

When looking at most indirect signals of dark matter, the profile of the dark matter is an important ingredient. N-body simulations seem to favor cusped profiles at the center of the galaxy such as the Navarro-Frenk-White (NFW) [173] and Merritt [164] profiles, while dynamical observations of galaxies seem to favor cored profiles of the isothermal variety [99]. Current dark matter simulations do not yet include the effects of baryons. Baryons dominate the gravitational potential in the center of our galaxy, so we find it prudent to consider three dark matter profiles. The first is the Navarro-Frenk-White profile:

$$\rho(r) = \rho_\odot \left(\frac{r_\odot}{r}\right)\left(\frac{1+(r_\odot/r_s)}{1+(r/r_s)}\right)^2, \tag{II.4}$$

with $r_s = 20$ kpc, where $r_\odot = 8.5$ kpc is the galactocentric distance of the sun and $\rho_\odot = 0.3$ GeV/cm^3 is the local dark matter density. The second is the isothermal profile

$$\rho(r) = \rho_\odot \frac{1+(r_\odot/r_s)^2}{1+(r/r_s)^2}, \tag{II.5}$$

with $r_s = 3.5$ kpc, and finally the Merritt et al. profile

$$\rho(r) = \rho_\odot \exp\left[-\left(\frac{2}{\alpha}\right)\frac{r^\alpha - r_\odot^\alpha}{r_s^\alpha}\right], \tag{II.6}$$

with $\alpha = 0.17$ and $r_s = 25$ kpc.

2.1.2 Cosmic Ray Propagation

Charged particles from dark matter annihilation must traverse part of the galaxy before arriving at detectors near Earth. This propagation has a non-trivial effect on the form of the signal.

Annihilations will take place in both the galactic plane and the dark matter halo. Once these particles are produced, they will either become confined by the galactic magnetic field to an approximately cylindrical region or escape the galaxy forever. Their propagation may be described by a diffusion equation, whose details we will now review. Some of the parameters entering this equation are uncertain, and will give rise to uncertainties in the observed dark matter signals.

In modeling propagation of cosmic rays through the galaxy, we will assume cylindrical symmetry (Fig. 2.1). We will adopt a cylinder with height $2L$, and some maximum radius R. The stars and dust will be confined to the galactic plane $z = 0$. The dark matter halo has a spherical symmetry. The particles are allowed to freely escape at the boundaries, and propagation within the cylinder is described by the diffusion-loss equation [205]:

$$\begin{aligned} \frac{\partial}{\partial t}\frac{dn}{dp}(\vec{x},t,p) &= \vec{\nabla}\cdot(D_{xx}(\vec{x},E,t)\vec{\nabla}\frac{dn}{dp} - \vec{V}\frac{dn}{dp}) - \frac{\partial}{\partial p}(\dot{p}\frac{dn}{dp} - \frac{p}{3}(\vec{\nabla}\cdot\vec{V})\frac{dn}{dp}) \\ &\quad + \frac{\partial}{\partial p}(p^2 D_{pp}\frac{\partial}{\partial p}(\frac{1}{p^2}\frac{dn}{dp})) + Q(\vec{x},t,p). \end{aligned} \tag{II.7}$$

The Diffusion coefficient: Cosmic rays diffuse out of the galaxy by scattering off inhomogeneities in the magnetic field. The diffusion coefficient

$$D_{xx} = \beta K_0 \left(\frac{\mathcal{R}}{\mathcal{R}_0}\right)^{\delta}, \tag{II.8}$$

is a function of the rigidity $\mathcal{R} \equiv p/Z$ where Z is the atomic number. K_0 is a constant, $\mathcal{R}_0$ is some reference rigidity, β is velocity, and δ is the scaling with respect to the momentum. We take a default value $K_0 = 5.8 \times 10^{28}$ cm^2 s^{-1}. The scaling, δ, is set by the spectrum of magneto-hydrodynamic turbulence in the interstellar medium. It is 0.33 for a Kolmogorov

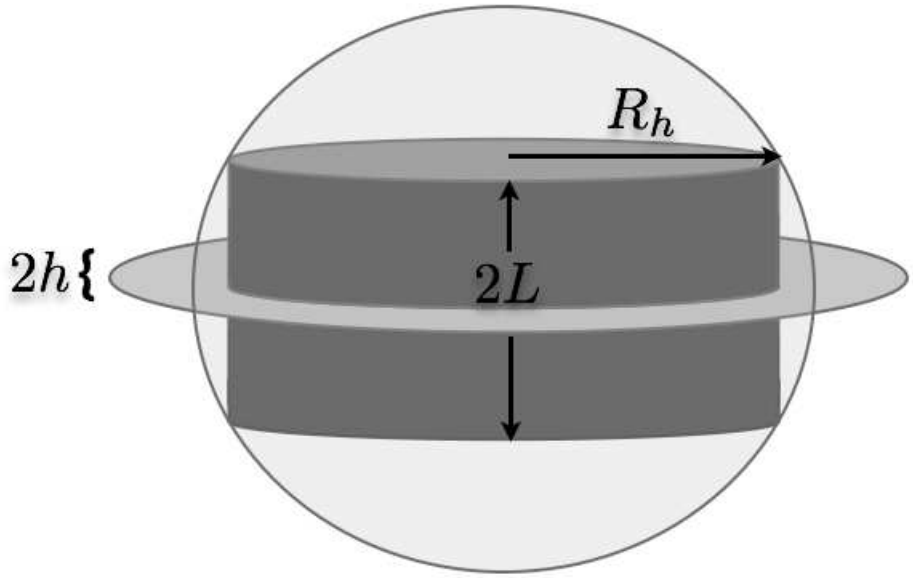

Figure 2.1: The diffusion zone (cylinder) is taken to have a height $2L$, with L in the range of 4-12 kpc [206], whereas the radial direction is taken as $R_h = 20$ kpc (see figure 1). Most of the interstellar gas is confined to the galactic plane at $z = 0$, which represents a slice through the cylinder and has a height of $2h = 100$ pc. Our solar system is then located in this plane at a distance of around $r_0 = 8.5$ kpc from the galactic center. All of this is enveloped by a spherically symmetric dark matter halo.

type spectrum, and 0.5 for a Kraichnan type spectrum[189]. Values in this region are reasonable. The dependence on β can be understood simply: higher β increases collisions with the inhomogeneities, and hence the diffusion.

Energy Loss: The energy loss, $\dot{p}$, comes from several sources: bremsstrahlung, Coulombic interactions with ionized gasses, inverse Compton scattering with starlight and with the CMB, and synchrotron radiation. Inverse Compton scattering and synchrotron radiation are the largest contributors to energy loss for electrons and positrons and not important for anti-protons. In the case of electrons the energy loss time is sometimes parametrized by τ, with $\dot{p} \propto p^2/\tau$. A typical value is $\tau \approx 10^{16}$ sec.

Re-acceleration: Re-acceleration comes from second order Fermi processes and is described as diffusion in momentum space. It enters the diffusion equation via the term

proportional to D_{pp} in Eqn. (II.7). If magnetic fields move randomly in a galaxy, cosmic rays can be speed up when reflected from a magnetic mirror coming them. Likewise, they are slowed down by reflecting from a mirror moving away. The diffusion coefficient D_{xx} and the re-acceleration coefficient D_{pp} are related via the Alfvén velocity [197]. These magnetic field waves are moving slowly with respect to higher energy cosmic rays, so re-acceleration only will effect the low energy cosmic rays.

Convection: The convection current $\vec{V}$ can be thought of as a wind streaming in the z direction outward from the galactic plane. It is due to the outgoing plasmas from the galaxy, and in our galaxy can be thought of as coming from cosmic rays accelerating the plasma [223]. For the case of positrons, convection and annihilations in the disk can be neglected.

Source terms and radioactive decays: For astrophysical sources, the source term Q is expected to proportional to a power law $\propto p^{-\gamma}$ localized in the galactic plane. It may also contain sources and sinks due to unstable cosmic rays.

We will employ GALPROP [205] for numerical solutions to the diffusion-loss equation. For a critical discussion of this method of cosmic ray propagation, see [140]

2.1.3 Some Uncertainties

Measurements of the boron to carbon ratio help to fix the ratio of primary to secondary cosmic rays. Boron is produced purely as a secondary, while carbon is mostly primary. This observation helps fix both the height of the diffusion zone and the diffusion parameters K_0 and δ. However, there can exist a large degeneracy between these parameters[83, 45]. Increasing the height of the diffusion zone traps more cosmic rays. This can be compensated by a simultaneous change in the diffusion parameter that allows cosmic rays to quickly escape the galactic plane. Since anti-protons of a non-dark matter origin are produced in the galactic plane as secondaries, just as boron is, this apparent degeneracy of parameters

does not give rise to a large uncertainty in the background prediction. Once the primary flux of protons is fixed (measured), the B/C ratio gives a rather precise prediction for the (astrophysical) anti-proton flux.

Unfortunately, the dark matter does not share the same independence of the astrophysical parameters. Depending upon which set of diffusion parameters are chosen, different dark matter signals result. The reason is that dark matter annihilations are not confined to the galactic plane. Rather, they occur throughout the halo, and increasing the diffusion zone includes more primary cosmic rays from dark matter. This change in L is not completely compensated by an increase in the diffusion out of the galactic plane as in the case of the background. Moreover, this increase in the height of the diffusion zone will affect positrons and anti-protons differently, as we will discuss in the following sections.

2.2 Experimental Constraints on Non-thermal Neutralinos

In this section we use GALPROP [205] to numerically solve the propagation equation (II.7) and find the expected flux of positrons and anti-protons, as well as the synchrotron radiation coming from the annihilation products of neutralino dark matter. When appropriate, we have checked these results explicitly using DarkSUSY [106], and found similar results for similar values of the astrophysical parameters. We discuss the possibility of neutralino dark matter annihilations to explain an excess of positrons as suggested by the HEAT [38, 39] and AMS-01[177] data, while simultaneously respecting the observed flux of anti-protons as measured by BESS [178]. At present, the anti-protons do not show any peculiar spectral features (though their flux is perhaps somewhat lower than expected). We use this data to set bounds. We also discuss bounds on the neutralino annihilation cross section from synchrotron radiation in the "WMAP haze" [92, 93, 125] obtained from the WMAP3 data [202], and discuss implications for the Fermi experiment.

2.2.1 Anti-Proton Bounds

Before attempting to fit the HEAT data or PAMELA data, we must take into account bounds from anti-protons. We will compare to the BESS 95 + 97 data [178] taken at the solar minimum, and modulate the interstellar spectrum with a potential of 550 MV. More recent data from both the 1998 BESS data[154] and the BESS-Polar data [4] will have a different modulation potential but display the same trends. In Figure 2.2, we show the anti-proton flux for varying mass of the wino-like neutralino. As expected, increasing the mass of the wino pushes the spectrum to slightly harder energies. The dominant effect, however, is that an increase in the wino mass results in a decrease in the annihilation cross section as well as number density in the profile, which changes the overall normalization of the curve. Apparently, a wino mass of 150 GeV gives too high a flux, but 200 GV is (marginally) consistent. Finally, the PAMELA anti-proton to proton ratio and its impact on wino dark matter.

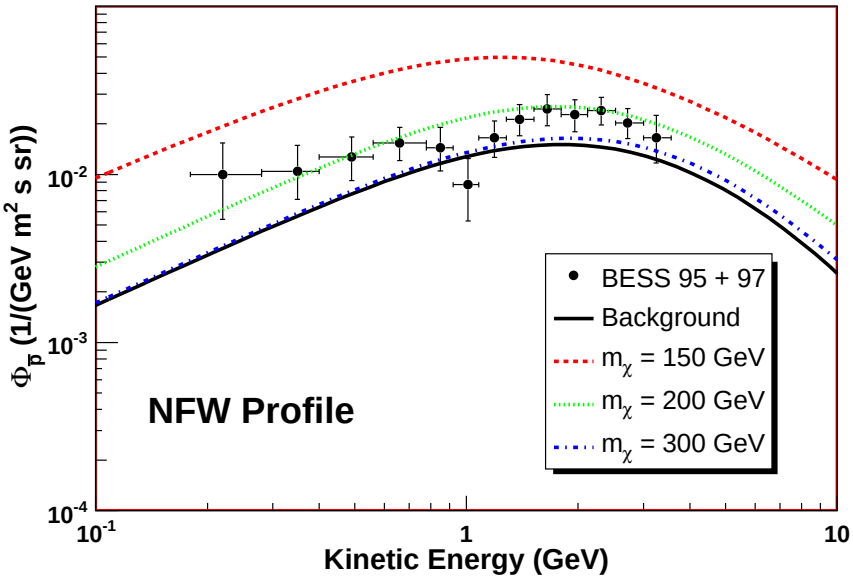

Figure 2.2: The flux in anti-protons for varying neutralino mass ($m_\chi = 150, 200, 300$ GeV). We have taken a diffusion zone height of $L = 4$ kpc.

As can be seen in Figure 2.3, these constraints are sensitive to the diffusion zone height. Here, we fix the neutralino mass at 200 GeV, and vary the diffusion height, L. Clearly the diffusion height directly affects the anti-proton flux. Again, we see that for a height of $L = 4$ kpc, $m_\chi = 200$ GeV is accommodated by the anti-proton data, but for larger diffusion cylinders, heavier winos would be required to be consistent with the anti-proton data.

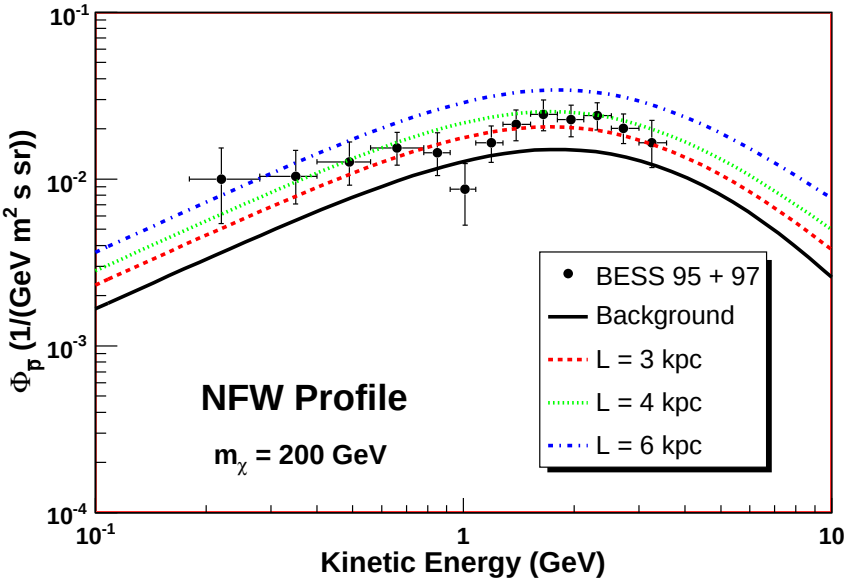

Figure 2.3: The flux in anti-protons for varying height of the diffusion zone cylinder with and NFW dark matter profile. We have taken a $m_\chi = 200$ GeV wino.

This minimum allowed wino mass is also a function of the dark matter distribution in the galaxy. Because anti-protons do not lose energy very efficiently (relative, to say, positrons), they come to us from a large region, and can potentially sample the inner portion of the galaxy, where the dark matter distribution can vary dramatically among different choices of profile. To assess the dependence of the profile on potential dark matter flux from anti-protons, we varied the profile in Fig. 2.4. Note that going from an NFW profile to another profile changes the flux of anti-protons from the dark matter particle by roughly $\pm 15\%$.

Our investigation of the anti-proton flux indicates that a pure wino of approximately

200 GeV is consistent with the data. To achieve significantly lower masses, one would have to push the astrophysical uncertainties. A 150 GeV pure Higgsino, however, is consistent with the data. At this mass, its annihilation cross section is approximately one order of magnitude below that of the wino.

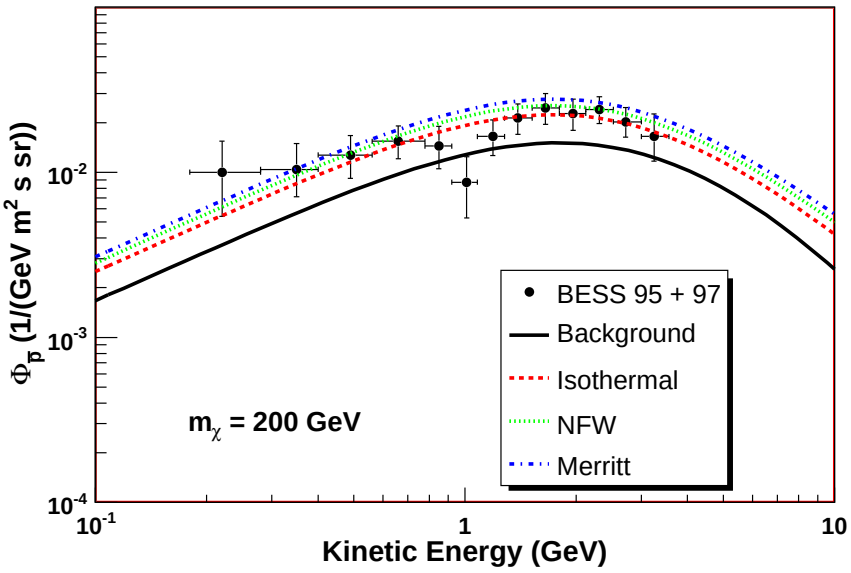

Figure 2.4: The flux of anti-protons is shown using different dark matter distributions. We have fixed $L = 4$ kpc, and the wino mass to be $m_X = 200$ GeV. Since the anti-protons may sample the inner region of the galaxy, the cuspiness of the profile does effect the anti-proton flux.

Measurements of cosmic ray anti-proton fluxes can also be used to put constraints on light neutralino candidates. In fact, the PAMELA experiment will measure anti-proton fluxes in the energy range 80 MeV - 190 GeV. It has already reported early data [51] which seems consistent with and extends earlier results, e.g. [154, 178, 4].

Taken at face value, the anti-proton data would appear to exclude a 200 GeV wino as an explanation of the PAMELA data, see e.g. [68]. However, anti-proton constraints suffer from theoretical uncertainties in cosmic ray propagation, as has been demonstrated in [81] (see also the discussion in [45]). One approach to bound the uncertainties and set propagation parameters for anti-protons is to parametrically fit models to well measured

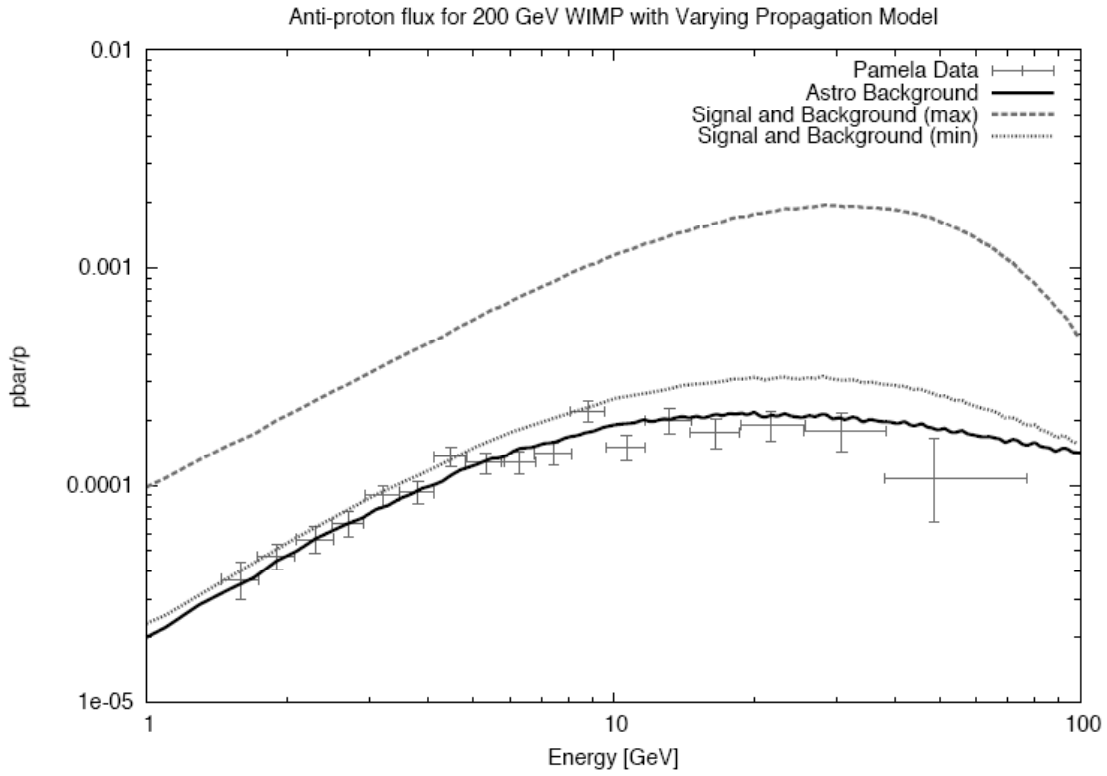

Figure 2.5: The anti-proton flux ratio for a 200 GeV wino-like neutralino as a function of kinetic energy. The lowest curve represents the conventional astrophysical background, whereas the remaining curves are the signal plus background for the 200 GeV candidate. These curves are the flux from dark matter annihilations given different choices for propagation model – all of which have been parametrically fixed by matching to the well known spectrum of secondary/primary fluxes (e.g. B/C ratio) [81].

secondary/primary fluxes such as the Boron to Carbon (B/C) ratio. In [81] it was found that this technique suffers from a number of degeneracies, as mentioned earlier. These degeneracies arise from the fact that the effective size of the confining region in which the cosmic rays propagate and the amount of energy lost to diffuse processes can be varied in combination, giving a good fit to the B/C ratio for a variety of values.

For the 200 GeV candidate we consider here, and assuming an NFW profile, the uncertainties in the propagation can lead to variations in the Dark Matter induced anti-proton flux by as much as an order of magnitude. This can be seen in Figure 2.5, where we present the dark matter signal for the benchmark propagation models appearing in [81] that yield

the minimum and maximum anti-proton signal. Both models are consistent with the B/C ratio. The order of magnitude variation in the theoretical prediction might cause the reader to be hesitant to conclude a 200 GeV wino is excluded from the data. At present, even for the minimal choice of propagation model, the 200 GeV candidate still gives a prediction that is about two times that expected from the recent observations of PAMELA [51]. If a 200 GeV wino is to explain the data, there must be additional problems with the models used to propagate the anti-protons.

2.2.2 Synchrotron Radiation

An excess of synchrotron radiation in the WMAP three year data [202], particularly significant for angles south of the galactic plane, has been suggested by subtracting out known foregrounds[92, 93, 125]. The residual component has a harder spectrum than other known sources for microwave emission, and has been dubbed the WMAP haze. Thus it seems that there is an unknown source of relativistic electrons and positrons moving in the galactic magnetic field, contributing to synchrotron emission. These electrons and positron could potentially come from dark matter [93].

While the exact interpretation of the haze is unclear at present, at minimum one should at least check that any potential dark matter candidate does not super-saturate the amount of synchrotron radiation. This has been noted by Hooper [121], who uses this observation to potentially place bounds on dark matter candidates. Here, we briefly revisit these bounds and semi-quantitatively discuss the astrophysical uncertainties that enter them.[2]

First, we discuss the particles that contribute to the WMAP bands. These electrons have energy greater than 5 GeV. This can be shown by analyzing the equation for synchrotron

[2]It should be noted that very strong bounds from X-rays might result if strong B-fields exist near the black hole near the galactic center[192]. These bounds are also very dependent upon the extrapolation of the dark matter profile to the inner few parsecs of the galaxy. We do not pursue these bounds further here.

emission. We use the formula of [100],

$$\epsilon_S(\nu,\gamma) = \frac{4\pi\sqrt{3}e^2\nu_B}{c}x^2(K_{4/3}(x)K_{1/3}(x) - \frac{3}{5}x(K^2_{4/3}(x) - K^2_{1/3}(x))) \tag{II.9}$$

with

$$x = \frac{\nu}{3\gamma^2\nu_B}, \tag{II.10}$$

γ is the boost factor, and the critical frequency is $\nu_B = eB/2\pi m_e c$. Here, K_n is the modified Bessel function of order n. This formula gives the synchrotron emission of the electron into all angles, averaged over an isotropic pitch angle distribution of the electrons with the magnetic field.

Figure 2.6 shows the amount of synchrotron radiation into the 22 GHz band as a function of the electron energy for a few different values of the magnetic field. This band is observed by WMAP, and it gives the most statistically significant contribution to the haze. Error bars in other bands are larger. Emission from energies below 5 GeV is negligible. This demonstrates the link between the haze and high-energy electrons and positrons. Thus, the excess in the HEAT data and the synchrotron emission can be linked to the relativistic electrons of similar energy. Indeed, any positron excess from a future experiment will potentially contribute to the haze at some level. If both the haze and positron excess arise from dark matter, then reconciling them will probe the astrophysical parameters of our galaxy.

As a point of reference, [121] argues that a pure wino that gives the full dark matter abundance would be excluded by the haze unless its mass exceeds 700 GeV. This is a very strong bound, and as we will see, would largely preclude any interpretation of any current or future excess in positrons as simple supersymmetric dark matter.

Central to placing this bound is an understanding of how electrons and positrons lose energy within the galaxy. This is controlled by the relative importance of the radiation field

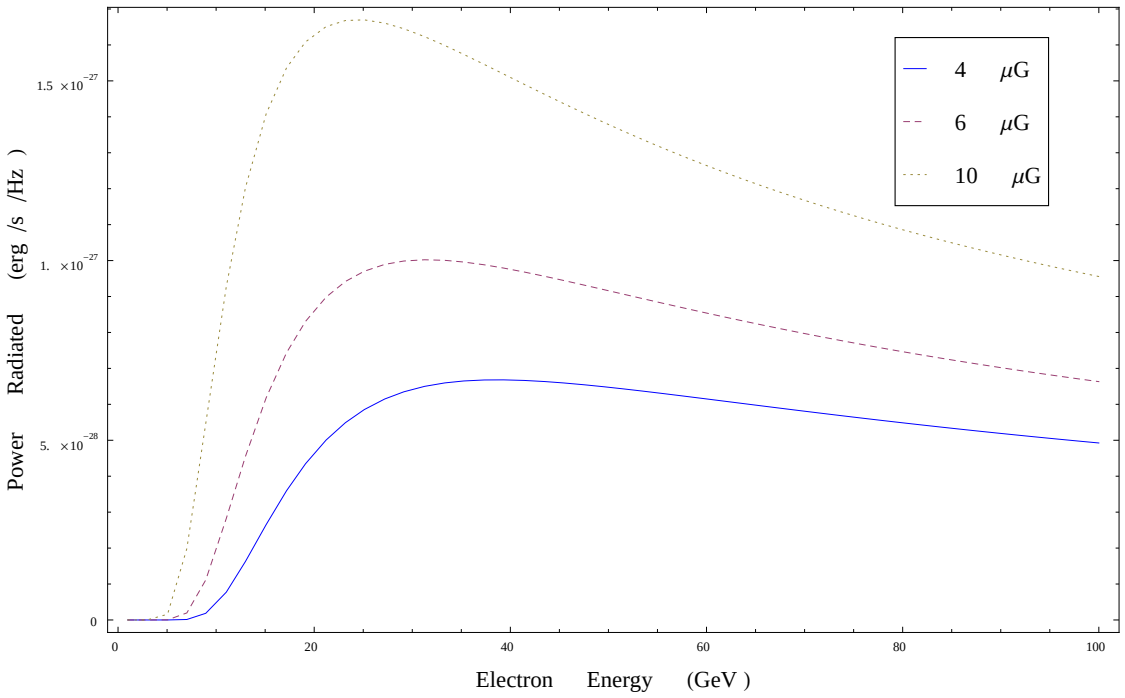

Figure 2.6: Power radiated into 22 GHz as a function of electron energy for different values of the galactic magnetic field. Notice that for energies below 5 GeV, there is negligible radiation.

and magnetic field in the region of interest. Large magnetic fields will cause the energy loss due to synchrotron radiation to dominate (and hence yield strong bounds from the haze). Large radiation fields will cause inverse Compton scattering to dominate. Reference [121] assumes a relationship between the energy density in the magnetic field and in the radiation field as: $U_B/(U_B + U_{rad}) \sim 0.26$. With a naive equipartition relation one would find this ratio ~ 0.5. There is no tight argument for equipartition between these two contributions. However, it is not unlikely that this relation should roughly hold at least approximately. After all, the B-field is related to cosmic rays, whose source is astrophysical objects. These, in turn, should roughly trace that radiation distribution.[3]

Having argued that the bound will sensitively depend on the choice of the magnetic and radiation field, we set about to semi-quantitatively investigate this effect by using a

[3]We thank Dan Hooper for discussion of this point.

different initial set of assumptions. Our view is that our starting point is not obviously less motivated than that of [121]. Our results might then give some indication of the size of the astrophysical uncertainties. Alternately, if one wishes to have a light dark matter particle with large cross section, our discussion will tell you what properties the galaxy must have to accommodate such a candidate.

To find the synchrotron sky map arising from our dark matter annihilation, we use GALPROP 50.1 [205] for the propagation of our dark matter derived electrons. We use the parameters $K_0 = 5.8 \times 10^{28}$ cm^2 /s, $\delta = 0.5$ (consistent with a Kraichnan spectrum of interstellar turbulence) [189], and L = 4 kpc, but find our results are relatively insensitive to these choices. Other choices for propagation parameters yield changes of roughly 10% in the results. The energy loss term is set by the relativistic Klein-Nishina cross section of cosmic rays on the interstellar radiation field combined with the synchrotron radiation from the magnetic field. The injection spectrum of dark matter is modified to accept input from PYTHIA 6.4 [200]. Following [125], we average emission over 20 degrees in longitude. For the interstellar radiation field, we use the fields from [183, 170] that are provided with the GALPROP package. We model the magnetic field by an exponential decay

$$B(r, z) = B_0 e^{-|r|/r_0 - |z|/z_0}. \tag{II.11}$$

We chose the characteristic distance r_0 such that the local magnetic field is $3\,\mu G$, and chose z_0 such that the field falls off quickly away from the galactic plane that is supposed to be responsible for creating this field. Also, we will use equation II.9 to find the synchrotron radiation. With sky-map in hand, following the same approach as [121], we use the synchrotron data of [93] to constrain possible dark matter candidates. Again, we do not assume a thermal history, and instead impose that our dark matter candidates make up all the relic density by fiat. We find a 90% confidence level upper bound on the annihilation cross section by using a χ^2 fit, allowing the addition of a constant background synchrotron

piece, independent of angle from the galactic center (relating to possible uncertainty in the subtraction procedure of Finkbeiner, et al.). [4]

It should be noted that we do not recalculate the residual haze for each choice of the magnetic field. However, since the approach of [93] was simply to derive the haze by doing a comparison of sky-maps close to and away from the core, we view this as a reasonable first approximation.

For a cuspy profile, most of the dark matter annihilations will happen in the galactic core. These then propagate outward until they are in the region we are looking at, 1 - 3 kpc from the center. They then radiate into the frequency band observed. Taking the approach outlined above, with $z_0 = 2$ kpc, we find the results in the top panel of Fig. 2.7. In particular, for a pure wino, for an NFW profile we find the bound of 300 GeV, much less stringent than the original bounds from [121]. This is dominantly due to our choice of radiation field maps [183, 170]. For these maps, $U_B/(U_B + U_{rad}) \sim 0.1$ for $B_0 = 10\ \mu G$ in the inner few kpc. A larger value for this ratio pushes us towards the limits of [121]. If an even smaller B field were present, near the galactic center, perhaps as small as 5 μG, this would further degrade the limits to the point where the bounds from anti-protons become competitive with (or exceed) these bounds.

Finally, we briefly discuss the effect of the z profile of the magnetic field. It is not clear exactly what form the z dependence of the B field should take. Taking z_0= 1 kpc again loosens the bound relative to our default choice of z_0= 2 kpc. This is shown in the lower panel of Fig. 2.7. Here, the bound on the pure wino dark matter only excludes 125 GeV wino dark matter, even for the relatively peaked NFW profile. In short, the local B-field (i.e. where synchrotron radiation is being measured) has a large effect on the size of the synchrotron radiation signal.

Figure 2.7 also shows the dependence on the galactic profile. Those that have a steeper

[4] Unlike [121], we impose the fit over the entire interval from 5 to 35 degrees south of the galactic plane.

rise towards the galactic center will give a larger contribution to synchrotron radiation. If the profile is somewhat softer than NFW then the bound is further weakened (this effect was also very clearly shown in [121] where a flat and NFW profile were shown). If the less-peaked isothermal profile is chosen, for example, all bounds due to synchrotron radiation are eliminated, even in the case where the B field falls off with z relatively slowly.

Also shown in the figure are the annihilation cross sections for pure wino and pure Higgsino at low velocity. For masses above M_W, both types of dark matter will annihilate almost exclusively to W bosons. Thus, discussions of γ-rays, synchrotron, $\bar{p}$ and positron signals will be identical for wino and Higgsino dark matter of the same mass, once this cross section difference is accounted for.

There is a very clear relationship between the halo profile and what types of experiments are best suited to look for dark matter. If the halo is quite peaked towards the center of our galaxy, then experiments that look for photons from this region, either gamma rays or synchrotron, will be best suited to find the dark matter. If, however, the dark matter distribution rises more slowly, then it is no longer clear that the center of the galaxy is the best place to look. Indeed, one can then look for electrons and positrons directly (perhaps from annihilation to W bosons), rather than looking for indirect by-products of annihilation (synchrotron, or continuum gamma rays). We now discuss this possibility.

2.2.3 Positrons

In the case of positrons, it is useful to consider the positron fraction, which includes both the primary flux of positrons $\Phi_{e^+}^{prim}$ as well as the background $\Phi_{e^+}^{sec}$ and the analogous fluxes for electrons, i.e.

$$\Phi = \frac{\Phi_{e^+}^{prim} + \Phi_{e^+}^{sec}}{\Phi_{e^+}^{prim} + \Phi_{e^+}^{sec} + \Phi_{e^-}^{prim} + \Phi_{e^-}^{sec}}, \tag{II.12}$$

as this ratio allows for cancellation of systematic errors and the effects of solar modulation (if we assume no charge bias). Preliminary indications from PAMELA data [9] indicate,

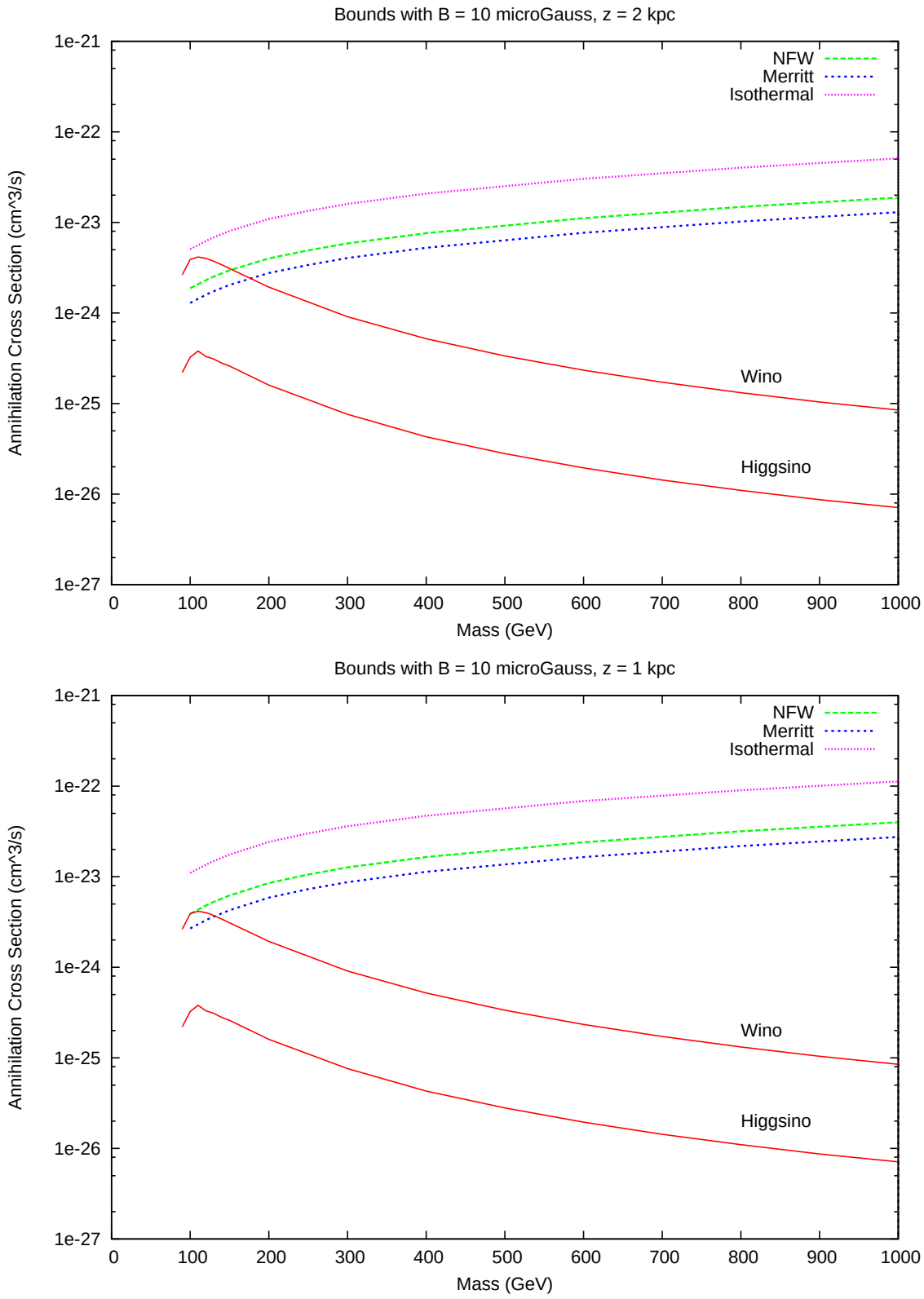

Figure 2.7: Bounds on the annihilation cross section into W^+W^- from synchrotron radiation. We have used the propagation parameters described in the text and only vary the magnetic field properties here.

however, that this charge bias may be important for low energies. Since the dark matter signals we will consider will involve production of electron and positrons at multi-GeV energies, we believe charge bias should be safely negligible in this regime.

In Figure 2.8, we consider a purely wino-like neutralino for masses in the range $150-300$ GeV. We have also included in the figure the data from the 1994 and 1995 HEAT missions [38, 39], as well as the data from AMS-01 [177]. The background curve is generated using the parameters of [67], with an Alfvén velocity of 20 km/s. At present the data begins to deviate from the background curve around 10 GeV, though the error bars are still large. The error bars should shrink dramatically with new data from PAMELA, at which point one might attempt to fit the data with a WIMP signal.

One might be able to determine the mass of the WIMP from this data. We see that the spectrum peaks slightly below $m_\chi/2$. This arises from annihilation to W-boson pairs and then subsequent decays to e^+/e^- near threshold. At present, there is no turn-over in the data. If PAMELA sees a turn-over in the data, then this would make a indirect measurement of the WIMP mass. A pure wino of up to 400 GeV might be eventually observed by PAMELA (see [188, 161]).

We find similar results for neutralinos that contain some bino or Higgsino component in addition to the wino, however in the case of the bino-like neutralino this can not be too large, otherwise the dark matter will not make a large contribution above the background.

For the case of $\bar{p}$ and synchrotron radiation, there were important astrophysical uncertainties. In particular, the distribution of of dark matter in the halo had a strong effect on the synchrotron bounds. The size of the cylindrical region to which the dark matter annihilation products are confined by the galactic magnetic field has a large effect on the $\bar{p}$ flux.

These two systematics have a much smaller effect on the signal from positrons. The

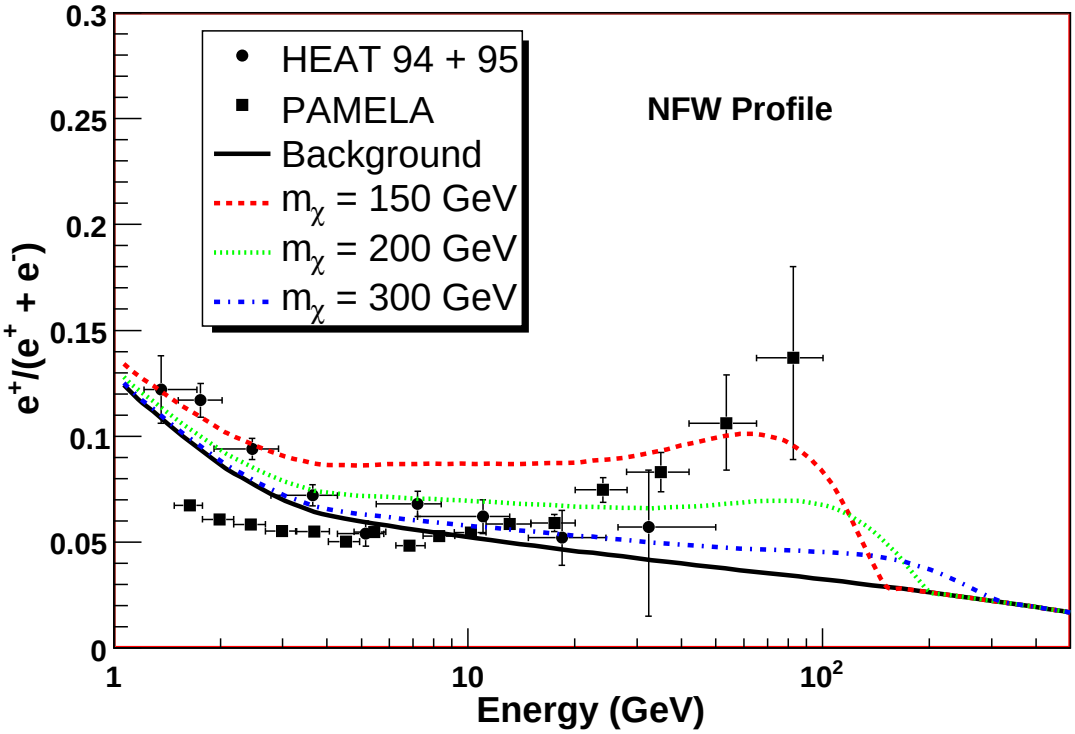

Figure 2.8: The positron flux from annihilations of non-thermally produced wino-like neutralinos for varying masses ($m_\chi = 150, 200, 300$ GeV) keeping an NFW profile. We have also included the data from the 1994-95 HEAT balloon based observations [38, 39] and measurements from AMS-01 [177].

reason is that positrons come from nearby: the typical diffusion length is only a few kpc. Errors in the background are typically much larger than the differences induced in the signal by astrophysical uncertainties. In this section we adopt the NFW halo profile as our canonical choice, noting that we find no significant changes for other profiles. Changing the height of the diffusion cylinder also does not have a very large effect on the positron ratio. We investigated the same cylinder height as shown in the anti-proton section, and again found variations that were small when compared with other uncertainties in the astrophysical backgrounds.

Re-acceleration can have an effect on the positron signal, however. In Figure 2.9 that using different backgrounds compatible with B/C will vary the positron signal as well. We

have used backgrounds with varying Alfvén velocities from [67]. The change in Alfvén velocity affects the low energy spectrum. Once the low energy background is normalized to data, this affects the prediction at high energies.

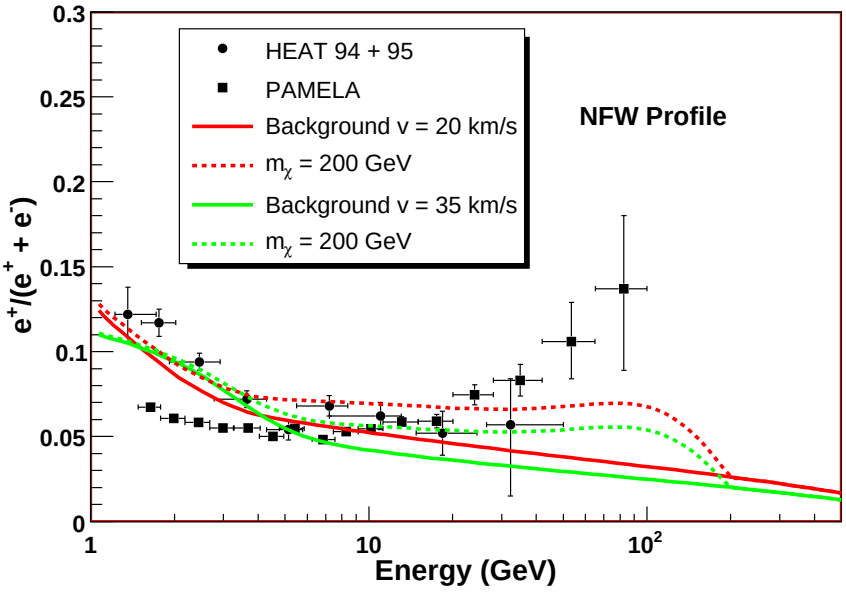

Figure 2.9: The positron ratio is shown for two different background curves, with (dashed) and without (solid) a Dark Matter contribution. The two background curves correspond to different values of the Alfvén velocity, $v = 20$ km/s (red/dark) and $v = 35$ km/s (green/light).

In all our discussions, we have not assumed any "boost factor". If there is some additional substructure in the halo within the diffusion length of the positrons, it is possible to enhance this signal somewhat. However, this substructure could also affect the signal in anti-protons, though not in a precisely identical way as they have a different diffusion length.

Now switch gears and take a phenomenological approach to the positron data. We vary the propagation parameters to examine how well a light neutralino can account for the positron excess. As standard values we take a diffusion coefficient of $K = 3 \times 10^{27} \epsilon^{0.6}$ cm^2 s^{-1}, a half height for the confinement region of $L = 4$ kpc, and an energy loss time of $\tau = 10^{16}$ s. The background is heavily dependent on the source distribution for electrons

and positrons, so we adopt the power-law $\Phi = \left(4.5\epsilon^{0.7}\right) / \left(1 + 650\epsilon^{2.3} + 1500\epsilon^{4.2}\right)$ from [32], where ϵ is the energy in units of GeV.

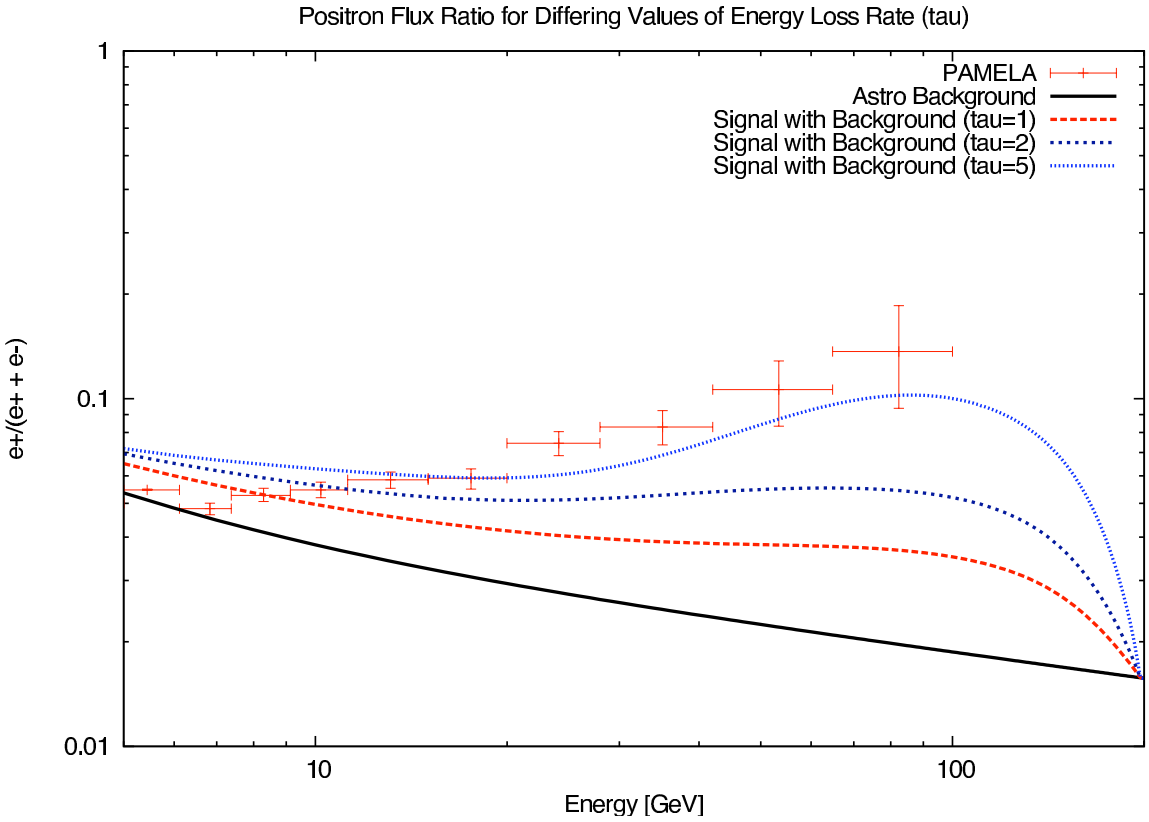

Figure 2.10: Positron flux ratio for Wino-like Neutralino with a mass of 200 GeV, normalized to the local relic density. We set the height of the propagation region at 4 kpc and consider varying values for the energy loss rate ($\tau = 1, 2, 5$) in units of 10^{16} s. The solid bottom line represents a conventional astrophysical background [32].

Our results for a 200 GeV particle that annihilates to W bosons appear in Figure 2.10. We have set the annihilation cross section, by assuming that the particle is a pure wino. The data of PAMELA are also shown [9], along side the anticipated signal in the presence of a 200 GeV wino[5]. The bottom (solid) curve represents the astrophysical background. The next higher curve represents the 200 GeV wino for the NFW halo profile and de-

[5]Below 10 GeV, the effects of charge bias on the solar modulation are expected to be non-negligible. We have checked that solar modulation [69] can bring the PAMELA data into improved agreement with the theoretical estimate, but do not attempt a detailed accounting of the solar modulation which would require additional detailed data on the solar B field. As the dark matter signal is dominant at higher energies, we focus on the region above 10 GeV where these effects are not important.

fault propagation parameters discussed above. The dark matter signal does not provide a convincing explanation for the excess reported by PAMELA.

However, we find that by varying the rate of energy loss of the positrons a better fit to the data is possible. Positrons lose energy via synchrotron radiation and via inverse Compton scattering off diffuse starlight and the cosmic microwave background. These energy losses are parametrized by the energy loss time τ. At the energies of interest this is dominated by the interaction of the positrons with starlight. While we have seen that the typically chosen default value of $\tau = 10^{16}$ s gives a poor fit to the data, claims in the literature [176], indicate that there are theoretical uncertainties in τ at the level of a factor of 2. So, we provide a curve for $\tau = 2 \times 10^{16}$ s, still a poor fit. A $\tau = 5 \times 10^{16}$ s gives a qualitatively good fit to the data. It is unclear that such a value is consistent with extant maps of starlight [168]. To clarify whether a neutralino could fit the data, it is important to determine this with certainty.

Depending on the distribution of the dark matter (e.g., if there are significant over densities of the dark matter close by) astrophysical boost factors could also contain a dependence on the energy (see e.g. [146]). This would largely mimic the effects of a change in τ, and could act to change the spectrum from the dark matter annihilation. An extreme example of this effect appeared recently in [126], where a local clump of 800 GeV wino Dark Matter was able to give the desired spectrum. We stress that the results appearing in Figure 2.10 do not include any astrophysical boost factors.

In summary, allowing for uncertainties in the energy loss rate and/or allowing for a small energy dependent boost factor may lead to an *effective* value of τ that could allow the 200 GeV candidate to account for the excess reported by PAMELA. Without invoking these uncertainties, an additional source of positrons is required.

Variation of the propagation parameters will also influence the positron spectrum. Once

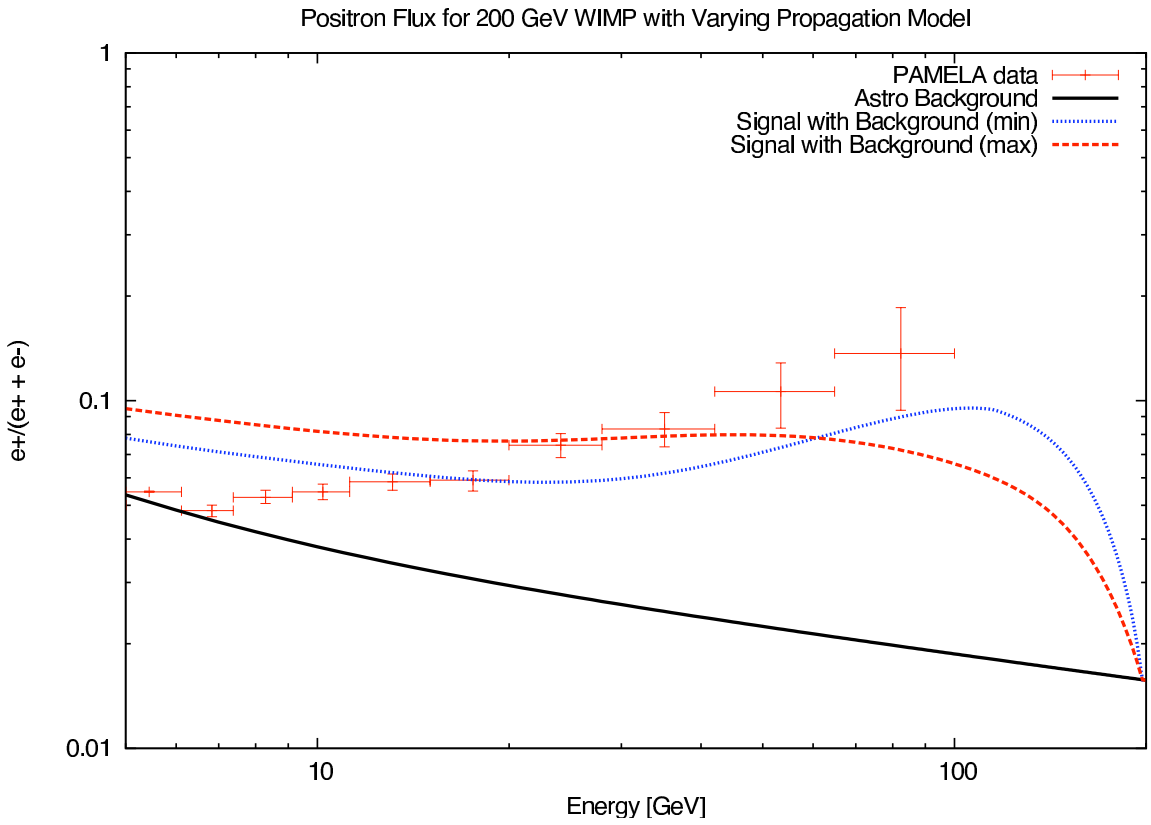

Figure 2.11: Positron flux ratio for a wino-like neutralino with a mass of 200 GeV. The lowest curve represents the astrophysical background, whereas the remaining curves are the flux ratio for (large) energy loss rate of $\tau = 5 \times 10^{16}$ s and varying propagation model (as discussed in the text).

the anti-proton flux is minimized, what happens to the positrons? This effect is not that pronounced, primarily because the high-energy positrons relevant for PAMELA originate within a couple kpc of Earth. Propagation uncertainties are thus reduced relative to those for anti-protons. Fig. 2.11 shows the effect on positrons of using the "min" and "max" models used for Fig. 2.5.

2.2.4 Gamma Rays

We begin with a brief review of γ-ray fluxes coming from dark matter annihilations, which are sensitive to both the halo profile and the diffuse γ-ray background. We then discuss existing constraints coming from the Energetic Gamma Ray Experiment Telescope (EGRET), which observed γ-rays coming from the galactic center.

Overview of γ-rays from dark matter Annihilation

We are interested in the continuum energy spectrum of gamma-ray flux coming from neutralino annihilations. The differential flux is given by

$$\frac{d^2\Phi_\gamma}{d\Omega dE_\gamma} = \frac{\langle\sigma v\rangle}{8\pi m_\chi^2}\sum_f \frac{dN_f}{dE_\gamma}B_f \int_{l.o.s}\rho^2(l)dl(\psi), \tag{II.13}$$

which is in units of photons/cm^2/s/GeV/steradians (sr).

The first factor depends only on the particle physics. $\langle\sigma v\rangle$ is the thermally averaged product of the annihilation cross section. dN_f/dE_γ is the differential photon yield for a particular decay with branching ratio B_f, and the sum is taken over all relevant decays. The second piece contains the distribution of dark matter, where $\rho(l)$ is the dark matter halo density profile and the integral is performed along the line of sight that originates from our location in the galaxy and continues through the full extent of the halo at an angle ψ relative to the ray passing through the galactic-center.

To isolate astrophysical uncertainties it is convenient to introduce the dimensionless

function $J(\psi)$

$$J(\psi) \equiv \frac{1}{r_\odot \rho_\odot^2} \int_{l.o.s} \rho^2(l) dl(\psi). \tag{II.14}$$

Ground and satellite based detectors will observe a finite patch of the sky with a given angular resolution. Therefore, when comparing theoretical predictions with what may be detected, we should average J over the minimum angular resolution of the detector,

$$\langle J \rangle = \frac{1}{\Delta\Omega} \int J(\psi) d\Omega \tag{II.15}$$

where $\Delta\Omega$ is the angular resolution (in steradians). This value is dictated by the experiment, e.g. this corresponds to $\Delta\Omega = 10^{-3}$ sr for EGRET, and $\Delta\Omega = 10^{-5}$ sr for Fermi Gamma-Ray Space Telescope (FGST). We fill focus on the Galactic Center as the best place to discover γ-rays from dark matter annihilations. Given the minimum angular resolution, the dark matter profile, and the source location we can perform the average in (II.15) using e.g. DarkSUSY. Some results for the line of sight integral to the galactic center appear in Table 1. An examination of Table 1 shows that the difference between a flat profile (Isothermal Cored) and NFW for EGRET can introduce two orders of magnitude difference in the signal. We also show the $\langle J \rangle$ for the Einasto profile, which has recently been favored by N-body simulations [172].

While isothermal cores are now disfavored by N-body simulations, it is still fair to say that the current lack of knowledge of the halo profile induces a large error in the predicted flux from the galactic center.

Using the expression for the flux (II.13) and averaging over the angular acceptance, the differential flux measured in the detector is

$$\begin{aligned} \frac{d\Phi_\gamma}{dE_\gamma} &= 9.40 \times 10^{-12} \left(\frac{\langle \sigma v \rangle}{10^{-27} cm^3 \cdot s^{-1}} \right) \\ &\times \left(\frac{100 \text{ GeV}}{m_\chi} \right)^2 \sum_f \frac{dN_f}{dE_\gamma} B_f \, \langle J \rangle \Delta\Omega, \end{aligned} \tag{II.16}$$

Profile	EGRET & Ground Based ($\Delta\Omega = 10^{-3}$ sr)	FGST ($\Delta\Omega = 10^{-5}$ sr)
Isotherm	30	30
NFW	$1,214$	$12,644$
Einasto	$1,561$	$5,607$

Table 2.1: The averaged line of site integral $\langle J \rangle$ to the galactic center for the NFW, Einasto, and Isothermal profiles with EGRET and FGST minimal resolution.

which is in units of photons/cm^2/s/GeV.

γ-ray signals from dark matter annihilations must compete with the diffuse γ-ray background. These include inverse Compton scattering of electrons with galactic radiation and bremsstrahlung processes from accelerated charges [207]. Thus, uncertainties in the propagation of cosmic rays and in the composition of the ISM (e.g. the distribution and density of hydrogen) lead to uncertainties in the expected diffuse background. It is vital to understand the diffuse background in order to confirm (or deny) the existence of dark matter annihilations and to distinguish between different theoretical predictions.

An analysis of the Fermi Data has led Dobler and collaborators [79] to conclude that there is an excess due to inverse Compton scattering of a hard electron population in the diffuse background near the galactic center. In their analysis, they take the Fermi all-sky maps and lump them into 6 different energy bins. They fit the data with 4 maps: a dust map [196] as a tracer for background pion emission, the Haslem 408 MHz map [117] as a tracer for background inverse Compton scattering, an isotropic background, and a "haze" component that is stretched around the center of the galaxy. This does mean that there could be dark matter, however a modeling of the diffuse background could eliminate the need for the haze component of the map.

At the present level of understanding, the differential flux for the diffuse γ-ray back-

ground may be fitted by a power-law of the form [48]

$$\frac{d^2\Phi_\gamma^{bg}}{d\Omega dE_\gamma} = \left(\frac{d^2\Phi_\gamma^{bg}}{d\Omega dE_\gamma}\right)_0 \left(\frac{E_\gamma}{1\text{GeV}}\right)^\alpha, \tag{II.17}$$

with $\alpha = -2.72$ and a normalization $\left(d^2\Phi_\gamma^{bg}/d\Omega dE_\gamma\right)_0 = 6 \times 10^{-5}$.

Constraints from EGRET

EGRET completed nine years of observations in June of 2000 and was sensitive to γ-rays in the energy range 30 MeV - 30 GeV. Using (II.17) for the diffuse background near the galactic center and integrating over the angular resolution of EGRET ($\Delta\Omega = 10^{-3}$) for the energy range of interest (1 GeV $\lesssim E_\gamma \lesssim$ 30 GeV) we find a background flux of $\Phi_\gamma^{bg} \simeq 10^{-8}$ photons cm^{-2} s^{-1}. For dark matter candidates that give a flux in excess of this, EGRET should have detected a signal. From (II.13), a neutralino annihilating to W-bosons with a mass of a couple hundred GeV and cross section $\langle\sigma v\rangle \approx 10^{-24}$ cm^3 s^{-1} yields a flux comparable to the background $\Phi_\gamma^{dm} \simeq 4 \times 10^{-8}$ photons cm^{-2} s^{-1}. This gives the first indication of the tension between a 200 GeV wino and the EGRET data. Of course, this result depends on the dark matter profile – assumed here to be NFW.

Extracting robust constraints on dark matter candidates from EGRET is subtle for reasons extending beyond the choice of the profile: there are uncertainties in both the diffuse background, as well as the EGRET data itself.

EGRET has detected a possible excess above 1 GeV in all sky directions. Addressing the discrepancy between the expected diffuse background and the EGRET data has been considered by a number of authors [80, 55, 94, 209, 207, 204, 73, 45]. These authors have argued for explanations that range from the possibility of annihilating dark matter[6] [73] to systematic errors in the EGRET experiment [204].

A key challenge for addressing the possible excess is developing an accurate model

[6]This explanation relies on a non-standard (anisotropic) choice for the halo profile, and seems to be at odds with other sources of indirect detection [45].

of the astrophysical background. This is particularly challenging given the inability to disentangle various components. These include the weak extragalactic contribution to the diffuse background, as well as a number of possible unresolved point sources [80, 30]. Due to the uncertainties, proposed models for the background can vary significantly. Compared to the background in Eqn. (II.17),

The 'conventional' GALPROP model [205] assumes a larger contribution from inverse Compton scattering, giving a higher contribution to the background and therefore to any signal that would be seen by EGRET. Yet other choices of background exist, including the 'Optimized' background [205], chosen to fit the EGRET excess without any additional Dark Matter component. At present, the take-home message is that there are large uncertainties in the astrophysical background.

In addition to the uncertainties associated with the diffuse background and the halo profile, there are other reasons for concern in regards to the quality of the EGRET data. Indeed, EGRET was only designed to operate for two of its nine year mission and an aging spark chamber introduced time-dependent uncertainties and systematic errors into the high end data products [169]. In [204] is was found that the most likely explanation of the EGRET excess was an error in the estimation of the EGRET sensitivity at energies above a GeV. This was argued to be convincing given that the 'excess' is seen in all sky directions, not just towards the galactic center. This seems to be the case, since preliminary Fermi data disagrees with the high energy EGRET data away from the Galactic plane [166].

With these caveats in mind, we use the EGRET data to constrain the 200 GeV wino at the Galactic Center. We state the constraint as a bound on the $\langle J \rangle$. Assuming EGRET correctly measured the background above a GeV and using the data from [162] to determine the diffuse background, we find that a 200 GeV wino has an annihilation cross section too large by a factor of three for an NFW profile – for a softer profile $\langle J \rangle \simeq 380$ this

would not be the case. These findings agree with already existing bounds in the literature [124, 80, 30]. However, we have also found that using the lower choice for the diffuse background in Eqn. (II.17) implies that the 200 GeV wino is already marginally consistent with the EGRET data for the NFW profile[7].

For now, it seems reasonable to consider the close proximity of the 200 GeV dark matter to the current bounds set by EGRET encouraging, since we will see that the improvements of FGST should clarify the situation.

We now consider the ability of FGST to detect the 200 GeV wino invoked above We focus on measurements of the galactic center, though measurements of the halo could be useful if progress is made in understanding the backgrounds there in detail.

FGST will offer a significant improvement over EGRET, probing energies from 20 MeV to 300 GeV with an angular resolution of around 0.1 degrees ($\approx 10^{-5}$ sr). The improved angular resolution will not only allow for separation of the point sources detected by EGRET, but the increased sensitivity will allow for a better opportunity to distinguish dark matter annihilation signals from the diffuse background. For the energy range of interest (around 1 GeV $\lesssim E_\gamma \lesssim$ 300 GeV) one finds a background flux from (II.17) of around $\Phi_\gamma^{bg} \simeq 10^{-10}$ photons cm^{-2} s^{-1} at a FGST angular acceptance of 10^{-5} sr. Compared with the EGRET result of $\Phi_\gamma^{EGRET} \simeq 10^{-8}$ photons cm^{-2} s^{-1}, this allows for an improved sensitivity by two orders of magnitude in terms of resolving signal from background. As in the case of EGRET, the diffuse background and halo profile are both sources of significant uncertainty. The better resolution and ability of FGST to resolve point sources should improve our knowledge of the diffuse background.

For our predictions for FGST we consider an $0.5^\circ \times 0.5^\circ$ region about the galactic center assuming an NFW profile and averaging with a minimum resolution set by FGST (i.e. 10^{-5}

[7] See [15] for a similar approach to dealing with uncertainties in the diffuse background and bounds on neutralinos coming from EGRET and FGST.

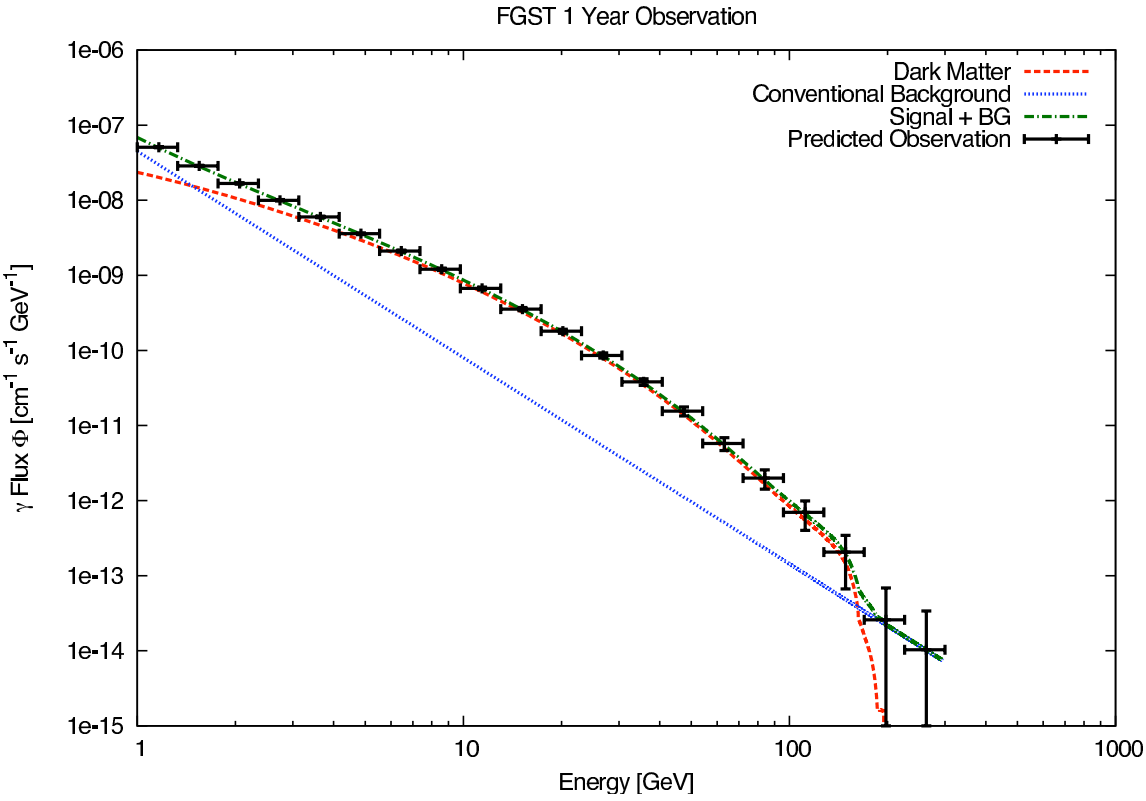

Figure 2.12: The differential flux for the 200 GeV wino-like neutralino and an NFW profile averaged over the minimum angular resolution of FGST (i.e. $\Delta\Omega = 10^{-5}$ sr) and integrated over a $0.5^\circ \times 0.5^\circ$ region around the galactic center. For the diffuse background we take the 'conventional' GALPROP model discussed in the text. The error bars represent the statistical uncertainty after one year of observations and do not account for systematical uncertainties.

sr). We have considered a number of choices for modeling the diffuse background. We find that for both a low choice of background given by the power-law with normalization in (II.17), as well as for higher backgrounds such as the 'conventional' and 'optimized' backgrounds mentioned above, that FGST will report a signal early. We find for the conventional background and a 200 GeV wino that a variation in the halo profile down to $\langle J \rangle \simeq 70$ in the region about the galactic center can still result in a detectable signal for FGST at the 5σ level within the first year of observation. In Figure 2.12 we present the prediction for the 200 GeV wino with an NFW profile, again after only one year of data. The error bars reflect statistical uncertainties. FGST should be capable of observing the

products of wino annihilation after the first year.

Here, we have focused exclusively on the bounds (and potentially signals) coming from our own galaxy. This approach will depend on the ability to successfully subtract away point sources and other diffuse backgrounds[80]. To avoid these sources, dwarf galaxies might be competitive places to look depending on their dark matter profiles. These have low backgrounds and good source identification, but suffer from low statistics. Preliminary searches are in progress [131], and are starting to constrain models that explain the PAMELA data.

CHAPTER III

Direct Detection of Supersymmetric Dark Matter

While the "WIMP miracle" motivates a stable particle with a weak scale mass and perturbative couplings, not just any weak scale stable particle will do. If the DM is weakly interacting in the strictest sense – *i.e.* has full-strength $SU(2)_L \times U(1)_Y$ gauge interactions – then DM may be excluded by existing direct detection (DD) experiments. In particular, a weak-scale Dirac (vector-like) fermion, $\chi_{\rm D}$, with $SU(2)$ interactions (which encompasses the simplest DM model of all, a Dirac neutrino), feels the weak force via the operator:

$$\mathcal{O}_{\rm vector} = (\bar{\chi}_{\rm D}\,\gamma^\mu\,\chi_{\rm D})\,Z^0_\mu. \tag{III.1}$$

When the coefficient of this operator is typical in size, namely $\mathcal{O}(g/\cos\theta_w)$, where g is the $SU(2)$ coupling constant and θ_w is the weak mixing angle, it leads to a huge DD signal – experiments constrain the DM mass to be greater than 50 TeV [198]. Furthermore, the thermal relic density for a 50 TeV Dirac neutrino will be far too large to explain the WMAP measurement. Thus, DM at the weak scale requires a strong suppression of this operator. In fact, it is straightforward to eliminate it entirely. If χ is a Majorana spinor, the operator $(\bar{\chi}\,\gamma^\mu\,\chi)\,Z^0_\mu$ identically vanishes due to the properties of Majorana bilinears. The DM may be Majorana if an $SU(2)$ singlet Majorana fermion mixes with a Dirac state. This mixing can only be accomplished via $SU(2)$ breaking in the WIMP sector, *i.e.* through a Higgs boson vacuum expectation value (vev). Then the resultant DM particle has a non-zero

coupling to a Higgs boson, h, and the dominant scattering process is due to the following operators:

$$\mathcal{O}_{\rm Higgs} = (\bar{\chi}\,\chi)\,h, \tag{III.2}$$

$$\mathcal{O}_{Z^0} = (\bar{\chi}\,\gamma^\mu\gamma^5\,\chi)\,Z^0_\mu. \tag{III.3}$$

In a multi-Higgs boson theory, h need not be *the* Higgs boson of the Standard Model (SM), but even in these theories, there often is a Higgs boson that has SM-like properties. We will explore the impact of these operators on Spin-Independent (SI) and Spin-Dependent (SD) scattering off of nuclei, paying particular attention to the expected correlation between the rates at these two types of experiments.

While we perform most of our analysis in the context of the Minimal Supersymmetric Standard Model (MSSM) (for a review of the MSSM, see [160]), we reference other models where appropriate to emphasize the generality of our arguments. We will review the assertion that post-LEP (largely due to the constraints on the chargino and slepton masses), one should consider a mixed or "well-tempered" neutralino as a likely DM candidate, if it is thermally produced [21]. We will show that in this case, light Higgs boson and Z^0 exchange will generically lead to a signal in the next generation of SI and SD experiments.

A thermal history for the WIMP is not the only possibility. For example, non-thermal mechanisms may populate the DM (*e.g.* through the decay of a modulus or gravitino [165]), or the DM can be overabundant and subsequently diluted by extra sources of entropy. These options allow a WIMP with a wider range of properties, since the annihilation rate is not fixed by the thermal history. In what follows, we do not rescale DD signals to the (too-low/too-high) thermal relic density. *In all cases, we assume that the* WIMP *constitutes the total* DM *density, determined from astrophysical measurements to be* $\rho_{\rm DM} \approx 0.3\,{\rm GeV/cm}^3$. We will be clear when we are making the assumption of a thermal history. For the purposes of this study, a "thermal" WIMP is one whose thermal relic density is within the generous

range $\pm 3\,\sigma$ of the WMAP measurement given in Eq. (I.1).

Related results already exist in the literature, including some comprehensive numerical scans. However, we find that often the (simple) underlying physics is left obscure. We hope to make clear the expected size of various contributions to DD and the relationship to the assumption of a thermal relic abundance. Assuming there are no conspiratorial cancellations, these typical sizes represent important targets for DD experiments.

There is an overwhelming literature in existence on the subject of DD, see reviews [97, 132] and references therein. Of particular interest to us is the relationship between the size of the SD and SI signals, which has recently been explored in [36, 43, 49].

In the next section, we begin by discussing the current experimental status and then make naive estimates for the SI and SD DD cross sections from h and Z^0 exchange respectively. In Sec. 3.2 we lay out the specific structure of the SI and SD operators in the MSSM and estimate the naive size of the SI and SD cross sections. Then in Sec. 3.3 we review the argument for a well-tempered neutralino and discuss some alternatives. Sec. 3.4 concentrates on illuminating the expected size of the SD cross section for mixed DM models with various restrictions. In Sec. 3.5 we describe the conditions under which SI and SD signals in the MSSM are expected to be correlated. Technical results are relegated to the appendices.

3.1 Direct Detection Preliminaries

The interactions in Eqs. (III.2) and (III.3) lead to SI and SD elastic signals in DD experiments, respectively. In Fig. 3.1 we have plotted the current experimental limits for SI and SD DD. Currently, the state of the art SI experiments are CDMS [13] and XENON [17]. XENON constrains $\sigma_{\rm SI}^{\chi p} < 4.5 \times 10^{-8}$ pb for $m_\chi = 30$ GeV. After combining their most recent run with previous data, CDMS-II has a 90% CL bound of 3.8×10^{-8} pb for a WIMP with a mass of 70 GeV [12]. In the most recent data set, two tantalizing events were

seen, but it is premature to attribute these to signal. In any case, XENON100 expects to place a limit on the order of $\sigma_{\rm SI}^{\chi p} \approx$ few $\times 10^{-9}$ pb by early 2010. Thus, we will consider SI cross sections greater than 5×10^{-9} pb as potentially probeable in the short-term, and hence "large."

There are two ways the SD cross sections are constrained. The first is via DD experiments. The current best bound on the SD DM-proton interaction comes from the KIMS experiment [148], $\sigma_{\rm SD}^{\chi p} < 1.6 \times 10^{-1}$ pb for $m_\chi = 70$ GeV; the best bound on the SD DM-neutron interaction coming from the XENON experiment, $\sigma_{\rm SD}^{\chi n} < 6 \times 10^{-3}$ pb for $m_\chi = 20$ GeV, with the strongest bounds for masses of $\mathcal{O}(10)$ GeV coming from PICASSO [20]. There are also bounds from DM capture in the sun, assuming (as is the case in the MSSM) that the DM has annihilation products which give rise to relatively hard neutrinos. Assuming annihilation of the DM to $W^\pm$ bosons is appreciable (as is appropriate for much of the parameter space considered here, see Sec. 3.3), IceCube [2] places very strong bounds for masses above 250 GeV with the strongest bounds coming at 250 GeV, $\sigma_{\rm SD}^{\chi p} < 3 \times 10^{-4}$ pb. At present, no limits exist from IceCube below this mass. For smaller masses, the best limits of this type come from SuperK [75], $\sigma_{\rm SD}^{\chi p} < 10^{-2}$ pb above $m_\chi > 20$ GeV.

Perhaps within the next two years [150], the COUPP [42] and PICASSO [37] experiments will take data with a projected sensitivity to SD scattering of $\sigma_{\rm SD}^{\chi p} \approx 10^{-4}$ pb. The will also have sensitivity down to much lower masses then the neutrino experiments. The XENON data will probe $\sigma_{\rm SD}^{\chi p} \approx 4 \times 10^{-3}$ pb for a 30 GeV WIMP. A 1 ton COUPP-like proposed experiment [49], might ultimately probe values as low as 10^{-7} pb. The DeepCore extension to the IceCube detector should be able to extend down to the 10^{-5} pb level with 5 years of data [215]. Bounds from neutrino experiments can be avoided if particular final states dominate WIMP annihilation, *e.g.* 1$^{\rm st}$ generation quarks, though this does not happen in the MSSM. We consider SD cross sections greater than 10^{-4} pb as potentially

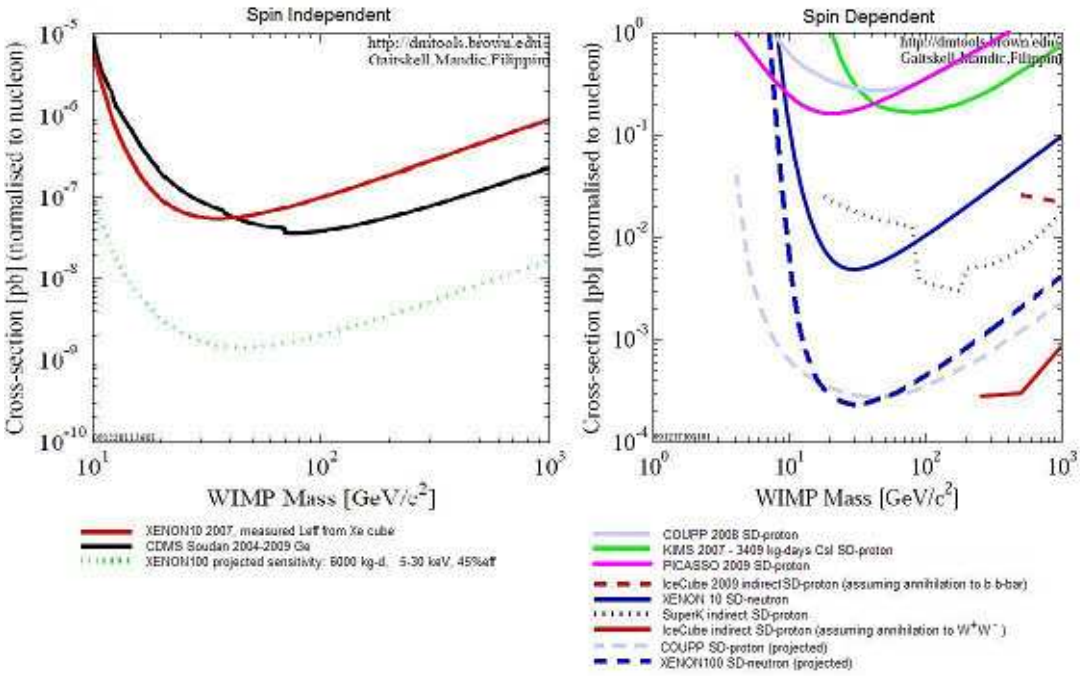

Figure 3.1: Current bounds on SI (left) and SD (right) DM-nucleon cross sections. The COUPP and XENON100 projected SD bounds are only estimates – we have scaled the current exclusion curve of COUPP by a factor of 10^{-3} [149] and the current SD exclusion curve of XENON10 by the factor which scales the XENON10 SI limit to the XENON100 SI limit.

achievable in the short-term, and hence "large."

3.1.1 Spin Independent

The operator responsible for SI DM-nucleus interactions is

$$\mathcal{O}_q^{\rm SI} = c_q\,(\bar{\chi}\,\chi)\,(\bar{q}\,q), \tag{III.4}$$

where χ is the DM and q is a quark. Taking the expectation value of this operator between two nucleon states ($N = p$ (proton) or n (neutron)) determines the effective interaction of the DM with a nucleon,

$$\langle N|m_q\,\bar{q}\,q|N\rangle = m_N\,f_{Tq}^{(N)}, \tag{III.5}$$

where the nuclear matrix element $f_{Tq}^{(N)}$ is determined in chiral perturbation theory from the pion nucleon-scattering sigma term. The coefficient of the effective DM-nucleon interaction,

$f_N(\bar{\chi}\,\chi)(\bar{N}\,N)$, is given by

$$\frac{f_N}{m_N} = \sum_{q=u,d,s} f_{Tq}^{(N)}\,\frac{1}{m_q}\,c_q + \frac{2}{27}\,f_{TG}^{(N)} \sum_{q=c,b,t} \frac{1}{m_q}\,c_q^{(h)}, \tag{III.6}$$

where $f_{TG}^{(N)} = 1 - \sum_{q=u,d,s} f_{Tq}^{(N)}$ and the h on $c_q^{(h)}$ refers to Higgs boson exchange [199].

The nucleon-Higgs interaction is coherent over the nucleus [96] resulting in the well known A^2 enhancement for SI cross sections. To compare between experiments using different nuclei, the elastic scattering cross section is normalized to a per nucleon value [97]:

$$\sigma_{\rm SI}(\chi\,N \to \chi\,N) = \frac{4}{\pi}\,m_r^2\,\frac{1}{A^2}\,(Z\,f_p + (A-Z)\,f_n)^2, \tag{III.7}$$

where m_r is the reduced mass between the DM and a nucleon.

We use the DarkSUSY package for numerical analysis [105], so for analytic estimates we will use the same values for the nuclear matrix elements, namely

$$f_{Tu}^{(p)} = 0.023 \quad f_{Td}^{(p)} = 0.034 \quad f_{Ts}^{(p)} = 0.14 \quad f_{TG}^{(p)} = 0.803$$
$$f_{Tu}^{(n)} = 0.019 \quad f_{Td}^{(n)} = 0.041 \quad f_{Ts}^{(n)} = 0.14 \quad f_{TG}^{(n)} = 0.800.$$

Since these values are derived from the pion nucleon scattering sigma term, their error bars are correlated.

If the Higgs boson, h, that mediates the interaction between the DM and the nucleon is SM-like, the coefficients c_q are given by

$$c_q = y_q\,y_\chi\,\frac{1}{m_h^2}, \tag{III.8}$$

where y_q (y_χ) is the yukawa coupling for the quark (DM) and m_h is the Higgs mass. The per nucleon cross section is then

$$\sigma_{\rm SI}(\chi\,N \to \chi\,N) \approx 5\times 10^{-8}\ \text{pb}\ \left(\frac{y_\chi}{0.1}\right)^2 \left(\frac{115\ \text{GeV}}{m_h}\right)^4 \qquad \text{(SI typical)}. \tag{III.9}$$

Estimates based on recent lattice simulations seem to favor smaller values for the nuclear matrix elements [101]. If these lattice results are correct, the dominant contribution to the

SI scattering cross section would be due to the heavy quark content of the nucleon (since $f_{TG}^{(N)} \to 1$ in the limit of small $f_q^{(N)}$) and the coefficient in Eq. (III.9) would be replaced by 2×10^{-8} pb. In cases where $c_d \gg c_u$, which can occur in models with multiple Higgs bosons such as the MSSM, then uncertainties in the $f_{Tq}^{(N)}$ can lead to as much as an order of magnitude variation in $\sigma_{\rm SI}(\chi\, N \to \chi\, N)$ [90].

3.1.2 Spin Dependent

The operator responsible for SD DM-nucleus interactions is

$$\mathcal{O}_q^{\rm SD} = d_q\, (\bar{\chi}\, \gamma^\mu \gamma^5\, \chi)(\bar{q}\, \gamma_\mu \gamma^5\, q). \tag{III.10}$$

Taking the expectation value of this operator between two nucleon states allows us to find the effective SD interaction of the DM with a nucleon ($N = p$ (proton) or n (neutron)),

$$\langle N|\bar{q}\, \gamma_\mu \gamma^5\, q|N\rangle = 2\, s_\mu^{(N)}\, \Delta q^{(N)}, \tag{III.11}$$

where $s_\mu^{(N)}$ is the spin of the nucleon and the $\Delta q^{(N)}$ are extracted from polarized deep elastic scattering. The coefficient of the effective DM-nucleon interaction, $2\, a_N (\bar{\chi}\, \gamma^\mu \gamma^5\, \chi)(\bar{N}\, s_\mu^{(N)}\, N)$, is given by

$$a_N = \sum_{q=u,d,s} d_q\, \Delta q^{(N)}. \tag{III.12}$$

The elastic scattering cross section quoted by the experiments is between the DM and a nucleon which is given by

$$\sigma_{\rm SD}(\chi\, N \to \chi\, N) = \frac{6}{\pi}\, m_r^2\, a_N^2, \tag{III.13}$$

where m_r is the reduced mass between the DM and a nucleon.

Again we follow DarkSUSY and use the following values for the SD calculations,

$$\begin{aligned} &\Delta_u^{(p)} = 0.77 \quad \Delta_d^{(p)} = -0.40 \quad \Delta_s^{(p)} = -0.12 \\ &\Delta_u^{(n)} = -0.40 \quad \Delta_d^{(n)} = 0.77 \quad \Delta_s^{(p)} = -0.12. \end{aligned} \tag{III.14}$$

The prediction for SD scattering is somewhat more robust to variation in the hadronic matrix elements than the SI case: the uncertainties in these values can lead to $\mathcal{O}(30\%)$ variation in the SD cross section [90].

If the SD interaction is mediated by the Z^0 boson, then the coefficients d_q are given by

$$d_q = \frac{g^2}{2\,c_w^2} T_3^q \left(\frac{Q_{Z-\mathrm{DM}}}{2}\right) \frac{1}{m_Z^2}, \tag{III.15}$$

where $Q_{Z-\mathrm{DM}}$ parametrizes the coupling of the DM to the Z^0 and $c_w \equiv \cos\theta_w$. For concreteness, (and since it is relevant for calculations of solar capture) when we quote values for SD scattering we will focus on the cross section off of protons. For SD scattering mediated by the Z^0, the neutron scattering is $\mathcal{O}(20\%)$ smaller. The SD cross section is

$$\sigma_{\mathrm{SD}}(\chi\, p \to \chi\, p) \approx 4 \times 10^{-4}\,\mathrm{pb} \left(\frac{Q_{Z-\mathrm{DM}}}{0.1}\right)^2 \qquad \text{(SD typical)}. \tag{III.16}$$

In the next section, we discuss the form that $Q_{Z-\mathrm{DM}}$ takes in the MSSM.

3.2 Direct Detection of Neutralino dark matter

The best DM candidate in the MSSM is the lightest neutralino, which is an admixture of Bino ($\tilde{B}$), Wino ($\tilde{W}$), and the up and down-type Higgsinos ($\tilde{H}_u$ and $\tilde{H}_d$). The stability of the lightest superpartner (LSP) is guaranteed by R-parity, which is introduced to avoid proton decay. The neutralino mass matrix is given by

$$\mathcal{M} = \begin{pmatrix} M_1 & 0 & -m_Z\, s_w\, c_\beta & m_Z\, s_w\, s_\beta \\ 0 & M_2 & m_Z\, c_w\, c_\beta & -m_Z\, c_w\, s_\beta \\ -m_Z\, s_w\, c_\beta & m_Z\, c_w\, c_\beta & 0 & -\mu \\ m_Z\, s_w\, s_\beta & -m_Z\, c_w\, s_\beta & -\mu & 0 \end{pmatrix},$$

where M_1 is the Bino mass, M_2 is the Wino mass, μ is the Supersymmetric (SUSY) Higgs boson mass parameter, m_Z is the Z^0 mass, $\beta = \arctan(v_u/v_d)$, $v_{u,d}$ are the up and down-type Higgs boson vevs, $s_w \equiv \sin\theta_w$, $c_w \equiv \cos\theta_w$, $s_\beta \equiv \sin\beta$, and $c_\beta \equiv \cos\beta$.

The composition of the lightest neutralino, which we denote χ, is specified by

$$\chi \equiv Z_B\,\tilde{B} + Z_W\,\tilde{W} + Z_{H_d}\,\tilde{H}_d + Z_{H_u}\,\tilde{H}_u. \tag{III.17}$$

If squarks are heavy, the only potentially sizable contributions to SI DD are from both CP-even Higgs bosons, h and H, where $m_h < m_H$. We comment on the typically subdominant squark exchange contributions in Appendix A. The Higgs boson exchange contributions are [35, 89],

$$\begin{aligned} \frac{c_u}{m_u} &= -\frac{g^2(Z_W - t_w\,Z_B)}{4\,m_W\,s_\beta} \\ &\times \left[\left(Z_{H_d} s_\alpha\,c_\alpha + Z_{H_u}\,c_\alpha^2\right)\frac{1}{m_h^2} + \left(-Z_{H_d} s_\alpha\,c_\alpha + Z_{H_u}\,s_\alpha^2\right)\frac{1}{m_H^2}\right] \end{aligned} \tag{III.18}$$

$$\begin{aligned} \frac{c_d}{m_d} &= \frac{g^2(Z_W - t_w\,Z_B)}{4\,m_W\,c_\beta} \\ &\times \left[\left(Z_{H_u} s_\alpha\,c_\alpha + Z_{H_d}\,s_\alpha^2\right)\frac{1}{m_h^2} + \left(-Z_{H_u} s_\alpha\,c_\alpha + Z_{H_d}\,c_\alpha^2\right)\frac{1}{m_H^2}\right], \end{aligned} \tag{III.19}$$

where $c_{u,d}$ are the SI operator coefficients given in Eq. (III.4), g is the $SU(2)$ gauge coupling, m_W is the $W^\pm$ mass, $t_w \equiv \tan\theta_w$, α is the Higgs mixing angle, $c_\alpha \equiv \cos\alpha$ and $s_\alpha \equiv \sin\alpha$. In the decoupling ($m_H \to \infty$ and $\alpha \to \pi/2 + \beta$) and large t_β limits, these expressions simplify:

$$\frac{c_u}{m_u} = \frac{-g^2}{4\,m_W}\,(Z_W - t_w\,Z_B)\,\frac{s_\beta}{m_h^2}\,Z_{H_u}, \tag{III.20}$$

$$\frac{c_d}{m_d} = \frac{c_u}{m_u}\left(1 - \frac{t_\beta}{s_\beta^2}\frac{m_h^2}{m_H^2}\frac{Z_{H_d}}{Z_{H_u}}\right), \tag{III.21}$$

where we have only kept the t_β enhanced contribution from H. We will use these expressions below in Sec. 3.5 when analyzing the allowed suppression of the SI cross section.

The lack of an observation of a Higgs boson at LEP makes it likely that we live in at least a moderate t_β regime (so that the tree-level contribution to the Higgs boson mass $m_h = m_Z \cos 2\beta$ is maximized), and constraints on the mass of the charged Higgs from flavor experiments point to the decoupling limit. Therefore, Eqs. (III.20) and (III.21) are

particularly useful for estimating the expected size of scattering. In Sec. 3.3 we will argue for the typical size of the various neutralino mixing angles which lead to SI cross sections of the order,

$$\sigma_{\rm SI}^{\rm MSSM}(\chi\, N \to \chi\, N) \approx$$
$$5 \times 10^{-9}\,{\rm pb}\left(\frac{115\ {\rm GeV}}{m_h}\right)^4 \left(\frac{(Z_W - t_w\, Z_B)\, Z_{H_u}}{0.1}\right)^2 \qquad \text{(MSSM: SI typical)}, \tag{III.22}$$

where we have used Eqs. (III.20) and (III.21) and taken $m_H \to \infty$.

In the heavy squark limit, contributions to SD DD come from Z^0 exchange. Since the Bino and Wino are both $SU(2)$ singlets, they do not couple to the Z^0. Therefore, SD is controlled by the Higgsino content of the WIMP. The Z^0 exchange contribution takes the form:

$$d_q = -\frac{g^2}{4\, m_Z^2\, c_w^2}\left(|Z_{H_d}|^2 - |Z_{H_u}|^2\right) T_3^q. \tag{III.23}$$

A non-zero Higgsino component (so that $Z_{H_{u,d}} \neq 0$) is insufficient to ensure a non-zero SD coupling. If $M_1,\ M_2 \to \infty$, so that a pure Higgsino is recovered, $|Z_{H_u}| = |Z_{H_d}| = 1/\sqrt{2}$, and the SD coupling vanishes. Instead, the Higgsino forms a Dirac state, and the large vector scattering of the Dirac neutrino is recovered. Hence, mixing with $\tilde{B}$ and/or $\tilde{W}$ (so that $|Z_{H_u}| \neq |Z_{H_d}|$) is required in order for the d_q's to be non-zero. This requirement also implies a non-zero SI cross section, giving the correlation demonstrated below.

The typical cross section for SD DD in the MSSM (again see Sec. 3.3) is given by

$$\sigma_{\rm SD}^{\rm MSSM}(\chi\, p \to \chi\, p) \approx$$
$$4 \times 10^{-4}\,{\rm pb}\left(\frac{|Z_{H_d}|^2 - |Z_{H_u}|^2}{0.1}\right)^2 \qquad \text{(MSSM: SD typical)}. \tag{III.24}$$

There are reasons to expect the squarks do not make a sizable contribution to the DD cross sections. In the MSSM, satisfying the LEP bound on the Higgs boson mass requires large radiative corrections from the stop loops. This implies that at least one stop must

have a TeV scale mass. Renormalization group flow tends to make the third generation sparticles lighter then the partners for the first and second generations. Therefore, it is plausible that squark contributions to DD scattering are negligible since only the first and second generation squarks contribute (see Appendix A for details about squark exchange). For concreteness, in all scans below we take the scalar superparters to be $\mathcal{O}(2\,\text{TeV})$. This is also why Eqs. (III.22) and (III.24) are expected to be good approximations. For a study which focuses on the effects of light squarks, see [43].

3.3 The Argument for a Well-Tempered Neutralino

Arkani-Hamed, Delgado and Giudice [21] argued that when one takes the LEP limits on charginos and sleptons into account, a pure neutralino (*i.e.* composed of only one gaugino eigenstate, usually taken to be Bino) is no longer the "natural" MSSM DM candidate, at least when one imposes the requirement of a thermal cosmology. They claim that one should instead consider a mixed neutralino, which they have dubbed "well-tempered." Since the relic density of mixed DM is set by annihilations to W^+W^- (and $t\bar{t}$ when kinematically allowed) there is a further condition that $m_\chi > m_W$. Hence, we will impose this requirement when we refer to "thermal" DM in the analysis that follows. In what follows, we review their argument and then discuss some non-thermal options. Note that SI DD has previously been studied for well-tempered models [29, 119], but no dedicated SD study exists.

3.3.1 Thermal history

We begin by considering the thermal history of a nearly pure Bino. If one does not allow for co- [110, 86, 87] or resonant [110, 84, 193, 78] annihilations, then Bino freeze-out is controlled by t-channel sfermion exchange. One can show [21] that in order to produce the observed DM relic density, the sfermion must be $\lesssim 110$ GeV. Since the LEP limits on

sfermions are $\mathcal{O}(100\,\mathrm{GeV})$, there is only a small experimentally allowed window for thermal Bino DM.

Either co-annihilations (*e.g.* with the stau or stop) or resonant annihilation through the pseudo-scalar Higgs (A^0) also allow dominantly Bino DM. However, both of these options involve numerical coincidences. In the first case the Boltzmann factor will exponentially suppress the density of the would-be co-annihilator unless $\exp(-\Delta M/T_f)$ is $\mathcal{O}(1)$, where $\Delta M = m_{\mathrm{NLSP}} - m_\chi$, m_{NLSP} is the mass of the next-to-lightest superpartner, and T_f is the DM freeze-out temperature. Since $T_f \approx m_\chi/20$, this requires a mass degeneracy, ΔM, of a few percent. To realize the second case requires a precise relationship between m_χ and m_A. When $m_\chi < m_W$, the Z^0 or h poles may be used to achieve the correct relic density, which requires a similar numerical conspiracy.

Located at the other extreme, far away from the pure Bino, is a pure Wino or a pure Higgsino. In these cases, the requirement of a thermal relic abundance fixes the mass to be $\mathcal{O}(2.5\,\mathrm{TeV})$ and $\mathcal{O}(1\,\mathrm{TeV})$ respectively. Thus, to realize either of these cases implies $\mu \gtrsim \mathcal{O}(100\,\mathrm{GeV})$. Since, in the MSSM, the Z^0 mass is given by

$$\frac{m_Z^2}{2} = -|\mu|^2 + \frac{m_{H_d}^2 - m_{H_u}^2 t_\beta^2}{t_\beta^2 - 1}, \tag{III.25}$$

where $m_{H_{u,d}}^2$ are the Higgs soft-mass squared parameters, this requires a substantial fine-tuning between μ^2 and $m_{H_{u,d}}^2$ in order to reproduce the measured Z^0 mass of 91 GeV. Therefore, the desire to alleviate fine-tuning in this expression leads to the requirement that $\mu \sim \mathcal{O}(100\,\mathrm{GeV})$. This will also naively lead to well-tempering since the neutralino mixing is proportional to m_Z/μ. Though the accuracy of the current measurement of the DM relic density (see Eq. (I.1)) requires a precisely determined neutralino composition, one can easily reproduce the DM abundance for any mass of $\mathcal{O}(100$ GeV).

A Higgs boson mass above the LEP bound requires large radiative corrections from a stop squark. This implies that the scale for these particles, m_{SUSY}, should be around

a TeV. These states yield additive corrections to $m^2_{H_{u,d}}$, proportional to $m^2_{\rm SUSY}$. Hence, even in the case when $\mu \sim \mathcal{O}(100\ {\rm GeV})$, there will naively be fine-tuning between these corrections and the bare value of $m^2_{H_{u,d}}$ in order to reproduce m_Z. Solutions to this "little hierarchy problem" have been proposed within the MSSM (*e.g.* [141]) – we will ignore this type of fine-tuning in our arguments, focusing instead on the model independent tuning implicit in Eq. (III.25).

3.3.2 Non-thermal options

A thermal history is not the only way to achieve the correct DM relic abundance [165]. It has even been argued [7] that there is a "non-thermal WIMP miracle" when there exist TeV scale states which decay to the DM via Planck suppressed operators. For example, a heavy gravitino (or string-theory moduli fields) can live long enough to dominate the energy density of the universe. Then when these states decay, they will produce superpartners which will decay down to the lightest neutralino, resulting in a neutralino relic density. This relaxes the relationship between the mass/composition and relic density of a neutralino.

A variety of other options have been proposed. Models where the energy density of the universe at the epoch of DM freeze-out was dominated by something other than radiation were studied in [133]. Alternately, if the DM interacts so feebly that it never achieves thermal equilibrium, one can achieve the correct value of the relic density via "freeze-in" production [112]. Since the total energy density of DM is close to that of the baryons, one can construct models where the DM relic density is set by an asymmetry which is determined by the baryon asymmetry [138]. In [98], it was shown that by varying the reheat temperature and allowing for non-thermal sources, any neutralino composition can result in the correct relic density. In [70], a low temperature phase transitions in the early universe changes the DM properties after freeze-out. All of these options involve either non-trivial cosmological histories or other model building challenges. We will focus on the

thermal – and hence well-tempered – case, with discussions of the deviations that arise when the thermal assumption is relaxed.

3.4 Spin Dependent Cross Sections for Mixed Dark Matter

In the MSSM, the neutralino mass mixing can often be approximately understood in terms of a two state system: a Dirac Higgsino mixing with either a Bino or a Wino. Thus, to understand the physics of SD scattering via Z^0 exchange, it is useful to consider the simple "Singlet-Doublet Model" (SDM) for DM, where the singlet has the same quantum numbers as either a Bino or a Wino, and the doublets have the same quantum numbers as the Higgsinos:

$$\mathcal{L}_{\rm SDM} \ni \mu_D \, D \, \bar{D} + \lambda \, \boldsymbol{h} \, S \, D + \lambda' \, \boldsymbol{h}^* \, S \, \bar{D} + \frac{\mu_S}{2} \, S^2. \tag{III.26}$$

Here D and $\bar{D}$ are a vector-like pair of $SU(2)$ doublet fermions, S is an $SU(2)$ singlet, $\boldsymbol{h}$ is the SM Higgs doublet, λ (λ') is the yukawa coupling which leads to the mixing between the $D\,(\bar{D})$ and S, μ_D is the vector-like mass for the D and $\bar{D}$, and μ_S is the Majorana mass for S. For the purposes of SD scattering it is sufficient to replace $\boldsymbol{h}$ by its vev, $\langle \boldsymbol{h} \rangle \equiv v = 174$ GeV. The exchange of the uneaten component of $\boldsymbol{h}$ leads to SI DD.

In the case where S plays the role of the Bino, the values of λ and λ' are constrained by the supersymmetric relations to be $\lambda \, v = -m_Z \, s_w \, c_\beta$ and $\lambda' \, v = -m_Z \, s_w \, s_\beta$, while in the case where S is the Wino, the values of λ and λ' are constrained by the supersymmetric relations to be $\lambda \, v = m_Z \, c_w \, c_\beta$ and $\lambda' \, v = m_Z \, c_w \, s_\beta$.

We now use this model to discuss the coupling of the Z^0 boson to the DM in the MSSM. In Appendix B we discuss the diagonalization of the 3×3 mixing matrix of the SDM. With appropriate substitutions, these expressions correspond to either Bino/Higgsino ($M_2 \to \infty$) and Wino/Higgsino ($M_1 \to \infty$) neutralinos. In these limits we can write down approximate expressions for the effective coupling of the DM to the Z^0. When there are no

degeneracies between parameters in the neutralino mass matrix and m_Z may be treated as a perturbation, we have (see [21] and Appendix B):

$$\text{(III.27)}\quad |Z_{H_d}|^2 - |Z_{H_u}|^2 = \begin{cases} \frac{c_{2\beta} s_w^2 m_Z^2}{\mu^2 - M_1^2} \\ \qquad \text{for } |M_1|, |\mu|, |\mu| - |M_1| > m_Z,\ M_2 \to \infty \\ \frac{c_{2\beta} c_w^2 m_Z^2}{\mu^2 - M_2^2} \\ \qquad \text{for } |M_2|, |\mu|, |\mu| - |M_2| > m_Z,\ M_1 \to \infty. \end{cases}$$

The largest values of $|Z_{H_d}|^2 - |Z_{H_u}|^2$ do not occur in this limit. Instead, they are found when two parameters of the neutralino mass matrix are degenerate. The reason is simple: a degeneracy allows a large gaugino–Higgsino mixing in spite of the relative smallness of the off-diagonal entries of the neutralino mass matrix (proportional to m_Z). It should be said that there is no particular reason to believe that a precise degeneracy should occur, since μ and the gaugino masses are SUSY preserving and breaking respectively. However, since this case maximizes the possible signal at SD experiments, it is worth noting. In the presence of these degeneracies, we have (see Appendix B):

$$\text{(III.28)}\qquad |Z_{H_d}|^2 - |Z_{H_u}|^2 = \begin{cases} \frac{(s_\beta - c_\beta) s_w\, m_Z}{2\sqrt{2}|\mu|} + \frac{(s_\beta^2 - c_\beta^2) s_w^2 m_Z^2}{8\mu^2} \\ \qquad \text{for } |M_1| = |\mu| > m_Z,\ M_2 \to \infty \\ \frac{(s_\beta - c_\beta) c_w\, m_Z}{2\sqrt{2}|\mu|} + \frac{(s_\beta^2 - c_\beta^2) c_w^2 m_Z^2}{8\mu^2} \\ \qquad \text{for } |M_2| = |\mu| > m_Z,\ M_1 \to \infty. \end{cases}$$

Perturbing away from the limit of exact degeneracy gives corrections to these expressions of $\mathcal{O}((M_i - \mu)/\mu)$. Note that DM with a mixed Wino/Higgsino has a SD DD rate enhanced relative to a Bino/Higgsino admixture by the appropriate power of $c_w/s_w = 1.8$.

What is the largest obtainable SD cross section in the MSSM? A numerical scan yields

$$\text{(III.29)}\qquad |Z_{H_d}|^2 - |Z_{H_u}|^2 < 0.4 \Rightarrow$$

$$\text{(III.30)}\qquad (\sigma_{\rm SD}^{\rm SUSY}) < 6 \times 10^{-3}\text{pb} \qquad (\text{General MSSM},\ \text{Non} - \text{thermal DM}),$$

when the squarks are heavy. This upper bound is largely a consequence of the LEP bounds on the chargino masses which force the mixing $\sim m_Z/\mu$ to be less than one. Eq. (III.28) provides a good analytic understanding of this number – it comes within approximately 10% of this value. The deviation is due to mixing effects that occur away from the large M_1 limit.

In many models of SUSY breaking the relation $M_1/\alpha_1 = M_2/\alpha_2 = M_3/\alpha_3$ holds. We refer to this condition as unified gaugino masses. Because this is equivalent to $M_2 \approx 2M_1$ at the weak scale, the LSP is mostly Bino and Higgsino. In this case,

$$|Z_{H_d}|^2 - |Z_{H_u}|^2 < 0.32 \Rightarrow \tag{III.31}$$

$$(\sigma_{\rm SD}^{\rm SUSY}) < 4 \times 10^{-3}\,{\rm pb} \qquad ({\rm Unified\ Gaugino\ Masses,\ Non-thermal\ DM}). \tag{III.32}$$

Finally, for $m_\chi > m_W$, a thermal relic density within $\pm 3\,\sigma$ of the WMAP measurement implies an upper limit on the amount of Higgsino in the DM particle. Therefore,

$$|Z_{H_d}|^2 - |Z_{H_u}|^2 < 0.24 \Rightarrow \tag{III.33}$$

$$(\sigma_{\rm SD}^{\rm SUSY})_{\rm thermal} < 2 \times 10^{-3}\,{\rm pb} \qquad ({\rm General\ MSSM,\ Thermal\ DM}). \tag{III.34}$$

This result holds for the case with unified gaugino masses as well.

To saturate the above bound (*i.e.* maximize $\sigma_{\rm SD}$ for thermal, well-tempered DM) requires a Bino/Higgsino mixture (recall that d_q vanishes for a pure Higgsino), with a negligible Wino contribution. The largest values of SD DD occur when the DM has the largest Bino/Higgsino mixing which happens for the lowest values of the DM mass. As the mass of the DM increases, a larger component of Higgsino or Wino is needed for the DM to efficiently annihilate down to the correct relic density, which in turn typically leads to a decrease in $\sigma_{\rm SD}$.

As shown in Fig. 3.2, there is a tight correlation between the SD cross section and the DM mass, in the decoupling limit when there is gaugino mass unification and a thermal

relic abundance.

For low masses, the neutralino is well-tempered for low masses and as $m_\chi \to \mathcal{O}(1\,\mathrm{TeV})$ the neutralino approaches a pure Higgsino. Examining Fig. 3.2, except for when the annihilation channel $\chi\chi \to t\bar{t}$ opens, σ_{SD} is a smooth, monotonically decreasing curve. An experiment sensitive to cross sections of $\mathcal{O}(10^{-4}\,\mathrm{pb})$ will probe $m_\chi \lesssim 200$ GeV. There is a spread in the points in this figure from the liberal range taken on the relic density constraint. For masses approaching $\mathcal{O}(1\,\mathrm{TeV})$, there is additional extent from the variation in the Bino content of the neutralino and from contributions from squark exchange. For masses at 1 TeV, σ_{SD} goes from $10^{-6}\,\mathrm{pb} \to 0$ for M_1 from $1300\,\mathrm{GeV} \to \infty$. Note that the projected reach of a 1 ton version of COUPP is $\mathcal{O}(10^{-6})$ pb for $m_\chi = 1$ TeV [49], *which would probe the entire range of* SD *cross sections for neutralinos excepting a nearly pure* TeV *Higgsino.*

Note that the imposition of the unified gaugino mass condition essentially imposes the requirement that there is a tiny Wino content in the LSP. The hatched region in Fig. 3.2 is filled in when non-unified gaugino masses are allowed. In this case, a thermal relic DM candidate can be obtained for a Bino tempered with Wino if $M_1 \approx M_2$, which implies that the SD cross section decreases, effectively filling in the region beneath the curve in Fig. 3.2. Note that when $\sigma_{\mathrm{SD}} \sim \mathcal{O}(10^{-6}\,\mathrm{pb})$, there is additional model dependence since the squark contribution becomes important (see Appendix A).

Finally, we note that there is a region of well-mixed Higgsino–Wino near 2 TeV with a thermal abundance (where $M_2 \approx \mu$). In this case, the second line of Eq. (III.28) applies, and we find an approximate SD cross section of 6×10^{-6} pb, perhaps able to be probed at a future 1 ton COUPP-like experiment. These are the neutralinos which account for the hatched region above the points in Fig. 3.2.

Not only is the SDM a simplified system useful for understanding the physics of SD

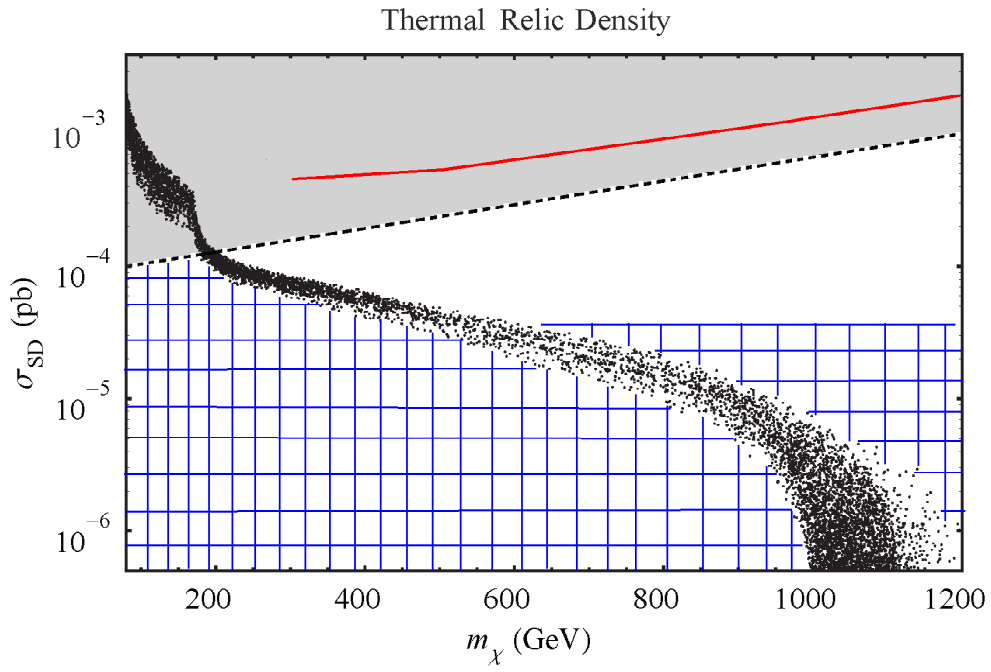

Figure 3.2: $\sigma^p_{\rm SD}$, as a function of m_χ for points satisfying the relic density constraint. We have imposed gaugino mass unification and taken the decoupling limit. The shaded region above the dotted line corresponds to "large" SD and will be probed in the near term. The solid red line is the current bound from IceCube, assuming annihilation to W^+W^-. The blue hatched region is filled in if the assumption of gaugino mass unification is relaxed. The sfermion masses are taken to be $\mathcal{O}(2\,\text{TeV})$.

scattering in the MSSM, it is potentially of independent interest. The DM may be unrelated to the solution to the hierarchy and simply given by the Lagrangian of Eq. (III.26) [24, 155]. Then the DD story is essentially unchanged except there is greater parametric freedom.

For example, the Higgs boson mass is no longer fixed by SUSY. Then the only constraint is $m_h \lesssim \mathcal{O}(\text{TeV})$ to unitarize $W^\pm_L$ scattering. For $m_h \sim$ TeV, the SI DD cross section is at most 10^{-12} pb which would not lead to a signal in the next round of SI experiments. While such a large Higgs boson mass is in tension with precision electroweak measurements, it could be reconciled with a contribution to the T parameter [180] in a way that factorizes from the DM phenomenology.

If one allows for a non-thermal history, the freedom of the SDM allows off-diagonal

parameters of the mixing matrix that give $|Z_{H_d}|^2 - |Z_{H_u}|^2 = 1$. This maximizes the SD DD signal from Z^0 exchange ($\sigma_{\rm SD}^{\rm SDM} \approx 4 \times 10^{-2}$ pb). Thus, the SDM with a non-thermal history predicts scattering anywhere up to (or even above) the current bounds. Requiring a thermal history limits the amount of doublet allowed in m_χ, decreasing $\sigma_{\rm SD}^{\rm SDM}$. For if a very large doublet component is chosen (in an attempt to maximize the SD cross section), the requirement of reproducing the relic density requires μ_S to be $\mathcal{O}$(TeV).

3.5 Spin Independent versus Spin Dependent

When a Majorana fermion couples to the Z^0, there is necessarily an interaction with a Higgs boson, which leads to SD and SI elastic scattering respectively. In the last section, we concentrated on the physics behind the size of the SD cross section. We now ask following questions: what is the expected correlation between the SI and SD signals? Is it possible to make one large while the other nearly vanishes?

Since m_h and m_Z are known in the MSSM, there exists a correlation between the SI and SD signals, at least in limit of heavy sfermions and Higgs boson decoupling. For this region of MSSM parameter space, the SI and SD DD cross sections are given by Eqs. (III.22) and (III.24), where only mixing factors and the Higgs boson mass are left unspecified. The light Higgs boson mass is constrained to lie in the tight range 114 GeV $< m_h <$ 130 GeV, where the lower bound is due to the LEP limit and the upper bound comes from considerations of fine-tuning. For the SplitSUSY model – where the decoupling and heavy sfermion limits certainly apply – the Higgs boson mass is allowed to be larger: $m_h < 160$ GeV.

In Figs. 3.3, 3.4 and 3.5, we have plotted the $\max(\sigma_{\rm SI}^p, \sigma_{\rm SI}^n)$ vs. $\sigma_{\rm SD}^p$ for neutralino scattering with various restrictions. We have taken the scalar superpartners to be $\mathcal{O}$(2 TeV).

As discussed in Section 3.1, we define "large" cross sections to be $\sigma_{\rm SI}^{\rm large} > 5\times10^{-9}$ pb and $\sigma_{\rm SD}^{\rm large} > 10^{-4}$ pb, motivated by the projected near term range of current DD experiments.

Hence, the shaded region delineates the (very approximate) reach of the next generation of SI and SD experiments. Note that this neglects the dependence of the sensitivity on the mass of the DM. The maximum for $\sigma_{\rm SD}$ in Fig. 3.3 is given by Eq. (III.30) and for Figs. 3.4 and 3.5 is given by Eq. (III.34).

In Fig. 3.3 we show points for both thermal and non-thermal neutralinos. This is the our most general framework, and in this case it is clear that the correlation between the relevant mixing angles (and hence cross sections) is weak. By only allowing points which have a thermal relic density within $\pm 3\,\sigma$ of the WMAP measurement (see Figs. 3.4 and 3.5), the correlation progressively improves. We will discuss this in detail in what follows.

We will pay special attention to the $m_H \to \infty$ limit. In any theory with multiple Higgs bosons, a small SI signal can occur when the diagrams from Higgs boson exchange cancel against one another. Two important points should be made. First, this cancellation is often incomplete and typically cannot be realized for scattering off of both protons and neutrons simultaneously. Second, such a cancellation is a conspiracy – it requires unexpected relationships between parameters in the Higgs sector and nuclear matrix elements. The finer the cancellation, the greater the conspiracy (for further discussion of this cancellation, see Sec. 3.5.3). If one takes the decoupling limit for Fig. 3.3, so that SI DD is determined by h exchange alone, the maximum SI cross section is $\sim 3 \times 10^{-8}$ pb. Note that even for $m_A \sim \mathcal{O}(\text{TeV})$ there can be nontrivial contributions for $t_\beta \sim \mathcal{O}(50)$ (see Eq. (III.21)).

There is a negative correlation between fine-tuning and the size of DD cross sections (see Eq. (III.25)) [158, 142]. To emphasize this point, in Figs. 3.3, 3.4 and 3.5 we have marked points with $|\mu| < 500$ GeV by blue dots and points with $|\mu| > 500$ GeV by red crosses. The apparent feature around $\sigma_{\rm SI} \approx 10^{-8}$ pb in Fig. 3.4 is due to the finite range of m_A taken in this scan ($m_A < 1\,\text{TeV}$) – the points above this gap have constructive contributions from h and H while the points below have destructive contributions. There

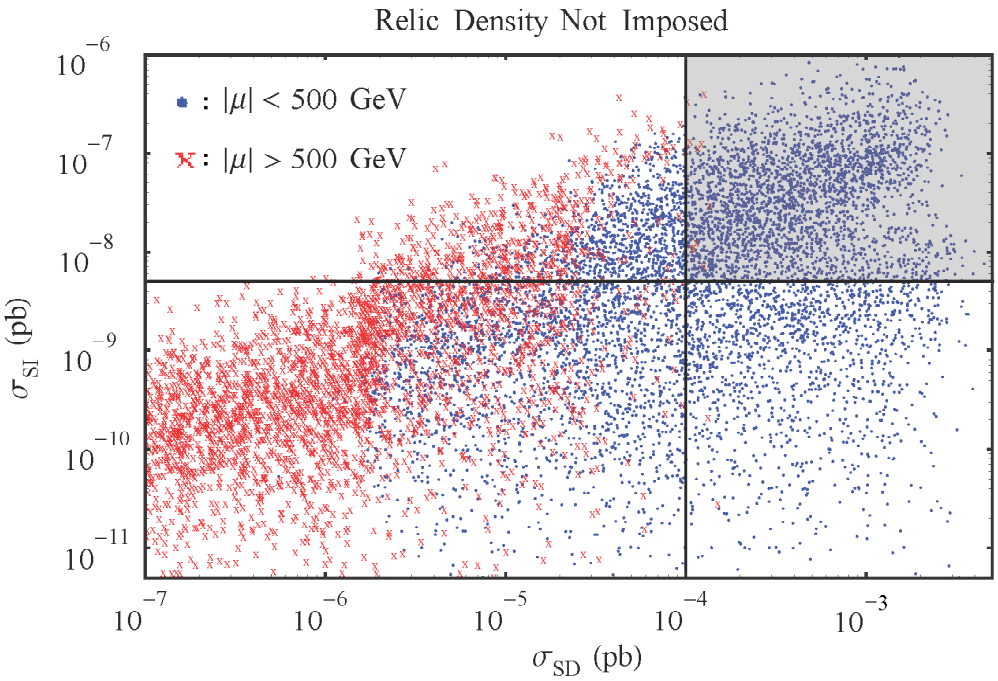

Figure 3.3: The $\max(\sigma^p_{\rm SI}, \sigma^n_{\rm SI})$ vs. $\sigma^p_{\rm SD}$ cross sections in pb for the MSSM. The dots (in blue) and crosses (in red) correspond to $|\mu| < 500$ GeV and $|\mu| > 500$ GeV respectively. The horizontal (vertical) line refers to the projected sensitivity for the next generation of SI (SD) experiments. We have shaded the near-term probeable region. Note that we are neglecting the dependence of this sensitivity on the neutralino mass. We have *not* imposed the thermal relic density constraint. All sfermions have masses of $\mathcal{O}(2$ TeV). If one takes the decoupling limit, there is a maximum value for $\sigma_{\rm SD} = 3 \times 10^{-8}$ pb.

are a few interesting features in Fig. 3.5. The gap which extends along the entire plotted range of SD cross sections is due to a slight cancellation between the various contributions from the light Higgs boson (see Eqs. (III.18) and (III.19)) which can occur at finite t_β ($t_\beta < 50$ in this scan). The small number of points around $\sigma_{\rm SD} = 3 \times 10^{-4}$ pb is due to the opening of the top threshold (see Fig. 3.2). The behavior around $\sigma_{\rm SD} = 2 \times 10^{-5}$ pb is due to the cross over from dominantly Bino to dominantly Higgsino DM, which occurs around $m_\chi = 500\,\text{GeV}$.

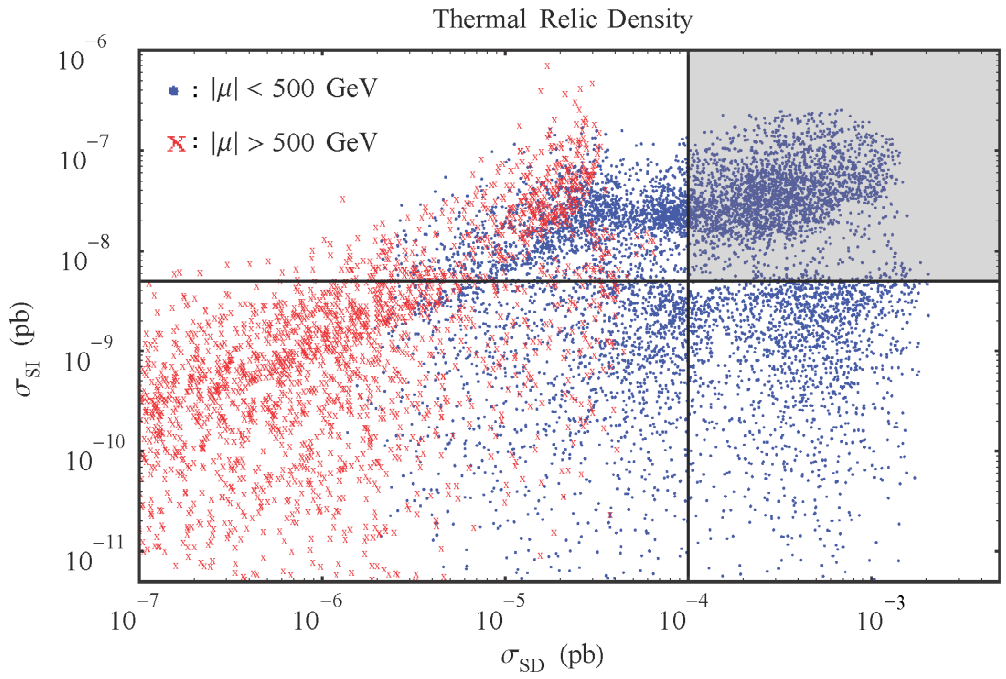

Figure 3.4: The $\max(\sigma^p_{\rm SI}, \sigma^n_{\rm SI})$ vs. $\sigma^p_{\rm SD}$ cross sections in pb for the MSSM. We have imposed that the thermal abundance of the neutralinos is within $\pm 3\,\sigma$ of the WMAP measurement. The dots (in blue) and crosses (in red) correspond to $|\mu| < 500$ GeV and $|\mu| > 500$ GeV respectively. The horizontal (vertical) line refers to the projected sensitivity for the next generation of SI (SD) experiments. We have shaded the near-term probeable region. Note that we are neglecting the dependence of this sensitivity on the neutralino mass. All sfermions have masses of $\mathcal{O}(2$ TeV).

3.5.1 Large SI and Large SD

To have non-zero SI and SD signals, a Bino-Higgsino, Wino-Higgsino or Bino-Wino-Higgsino mix is required. In fact, appreciable SI and large SD signals can be generated as long as the Higgsino fraction is larger than $\mathcal{O}(10\%)$. Note that the $|\mu| < 500\,$GeV points, which correspond to less fine-tuning in m_Z, imply large SD signals. When the gaugino fraction is dominated by Wino rather than Bino, the relative size of g and g' gives a slight enhancement in the SI cross section. There can be further enhancement of the SI cross section if $\mathrm{sgn}(Z_B) \neq \mathrm{sgn}(Z_W)$ (see Eq. (III.18)) which accounts for points with the largest SI values in Figs. 3.3 and 3.4. This cannot occur in models with unified gaugino masses,

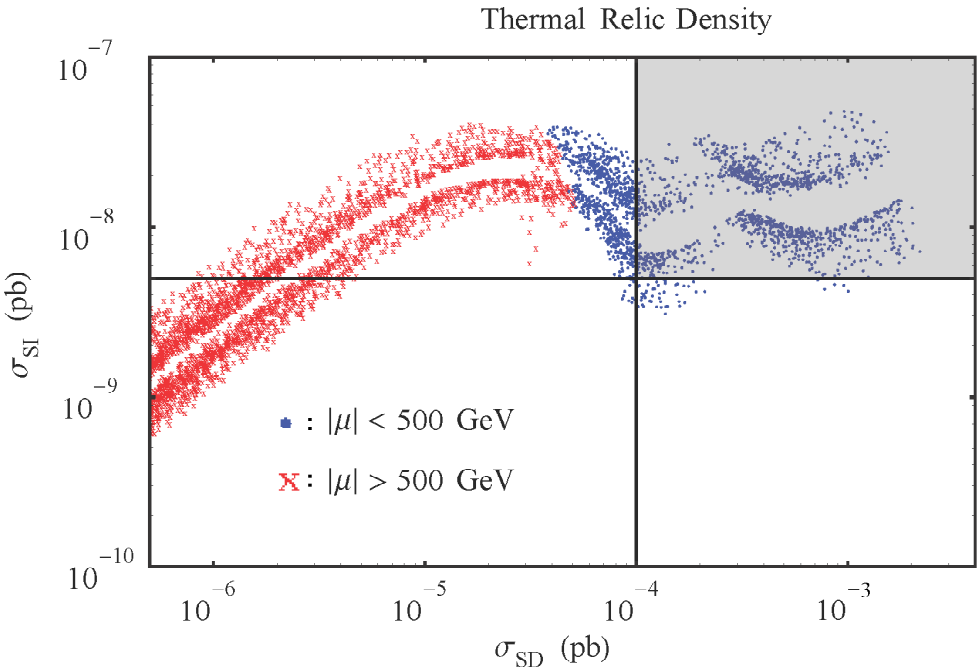

Figure 3.5: The $\max(\sigma^p_{\rm SI}, \sigma^n_{\rm SI})$ vs. $\sigma^p_{\rm SD}$ cross sections in pb for the MSSM with gaugino mass unification. We have imposed that the thermal abundance of the neutralinos is within $\pm 3\,\sigma$ of the WMAP measurement. We have taken the decoupling limit ($m_A = 4\,$TeV). The dots (in blue) and crosses (in red) correspond to $|\mu| < 500$ GeV and $|\mu| > 500$ GeV respectively (see the text for a discussion). The horizontal (vertical) line refers to the projected sensitivity for the next generation of SI (SD) experiments. We have shaded the near-term probeable region. Note that we are neglecting the dependence of this sensitivity on the neutralino mass. All sfermions have masses of $\mathcal{O}(2$ TeV).

where $M_2 \approx 2\,M_1$.

Large SI and SD signals occur as long as there is non-trivial gaugino content in the WIMP. Imposition of the thermal relic density constraint for $m_\chi > m_W$, ensures a minimum required Bino component. If one imposes the large SI and SD condition, $|Z_B|^2 \lesssim 0.7$ and $|Z_B|^2 \lesssim 0.85$ below and above the top threshold respectively. Note that the large SD requirement implies that $m_\chi < 200\,$GeV (see Fig. 3.2). Hence, the assumption of a thermal history is necessary to conclude that the neutralino is a Bino-Higgsino admixture, rather than Wino-Higgsino.

In the next three subsections we will attempt to elucidate the difficulties one encounters

when trying to suppress SI and/or SD. This will allow us to argue that large SI and SD DD signals are the generic prediction for a well-tempered MSSM neutralino, since suppression of either SI or SD or both requires doing some gymnastics. While future data may force these contortions upon us, we conjecture that if the DM is a well-tempered neutralino, it is likely to be discovered in the next generation of DD experiments.

3.5.2 Small SI and Small SD

There are two ways to suppress both SI and SD. The first is to make $|Z_{H_u}| = |Z_{H_d}| = 0$, which is equivalent to the $\mu \to \infty$ limit. This limit leads to fine-tuning of the electroweak scale. To achieve the proper thermal relic abundance in this case requires a Bino-Wino mix. Note that the Bino and Wino only mix indirectly through the Higgsino. Therefore, two insertions of the mixing factor are required, and the resulting mixing is of size $(m_Z/\mu)^2$. One can see the effects of this limit by inspecting the red crosses in Figs. 3.3, 3.4 and 3.5. The upper bound in Figs. 3.3 and 3.4 are from points which are either Bino/Higgsino or fully mixed states while the points with the smallest values for SI are due to either Wino/Bino neutralinos or the cancellations discussed in Sec. 3.5.4.

The second option is to take $M_{1,2} \gg \mu$. This will imply that $Z_{B,W} = 0$, thereby suppressing SI DD, and $|Z_{H_u}| = |Z_{H_d}|$ so that SD DD is also zero. Reproducing the measured relic density then requires $\mu \approx 1$ TeV. When one does impose the thermal relic density as a prior, Fig. 3.2 shows that for DM masses of $\mathcal{O}$(TeV), *i.e.* the region of dominantly Higgsino DM, the SD cross section ranges from $\mathcal{O}(10^{-5}\,\text{pb})$ to 0. Fig. 3.5 shows the corresponding SI cross sections for this range. The trend of SI and SD going to zero in this plot is due to the limit $M_{1,2} \to \infty$. Thermal dark matter in either of these two limits (μ or $M_{1,2} \to \infty$) will have a finely-tuned electroweak scale.

3.5.3 Large SI and Small SD

There are points which have large SI and SD with a nearly maximal gaugino fraction. If one relaxes the requirement of large SD, then the gaugino fraction can be pushed to nearly 100% while keeping the product $Z_{B,W}\, Z_{H_{u,d}}$ approximately fixed, which in turn keeps the SI cross section constant. The relic density constraint can still be satisfied since both Winos and Higgsinos annihilate to $W^{\pm}$ bosons with approximately the same rate.

There is another way to have small SD while allowing large SI. In the context of the SDM, one can take $\lambda = \lambda'$, *i.e.* $t_\beta = 1$ in the MSSM. From the SDM mass matrix (see Appendix B), one can see that mixing between S and D_- will vanish. Since the SD cross section is proportional to this mixing factor, Z_{D_-}, it will be zero as well. This effect accounts for the empty region in Figs. 3.3 and 3.4 since we restricted $t_\beta > 5$ in our numerical scans.

For $\tan\beta \gtrsim 1.5$, we find that for $\sigma_{\rm SI} \sim 5 \times 10^{-9}$ pb the smallest cross section for SD is $\sigma_{\rm SD} \sim 10^{-6}$ pb. If one allows $\sigma_{\rm SI} < 5 \times 10^{-9}$ pb, then as $|Z_{H_{u,d}}| \to 0$, $\sigma_{\rm SD}/\sigma_{\rm SI} \to |Z_{H_{u,d}}|^2 \to 0$. Hence, SD falls off faster then SI. However, this is the $\mu \to \infty$ limit which leads to fine-tuning as described above.

3.5.4 Small SI and Large SD

Large SD requires a well-tempered neutralino, which naively also leads to large SI DD. In this section we will enumerate the various options one has for suppressing SI signals. We will argue that all options require fine-tuning or numerical coincidences.

Here are the options for minimizing $\sigma_{\rm SI}$:

1. One can make m_h and m_H heavy; however $m_h \approx 115$ GeV in the MSSM in the absence of large fine-tunings. Even in SplitSUSY, $m_h \lesssim 160$ GeV.

2. Since $c_{u,d} \sim (Z_W - t_w\, Z_B)$, *i.e* the Higgs couples to the Zino, one could attempt to

restrict the DM to only be a photino-Higgsino admixture. In Appendix C, we show that this is impossible when one restricts M_2 by the LEP bound.

3. One can tune $\left(f_{Tu}^{(N)} + 2\,\frac{2}{27}\,f_{TG}^{(N)}\right)\,\frac{c_u}{m_u}$ against $\left(f_{Td}^{(N)} + f_{Ts}^{(N)} + \frac{2}{27}\,f_{TG}^{(N)}\right)\,\frac{c_d}{m_d}$ by tuning the contribution from H against that from h. As we will discuss below, it is not possible to precisely tune this quantity to zero simultaneously for the proton and the neutron (see Fig. 3.6). However, an approximate realization of this condition is possible – this is the tuning that underlies large SD/small SI points in Figs. 3.3 and 3.4 and reported in the literature (*e.g.* [171]).

4. One can tune the contribution from the proton against the contribution from the neutron. The cancellation would only hold for a specific element. Since all experiments do not use the same elements, we will not pursue this case further.

In what follows, we minimize the SI cross section by tuning the contributions from the h and H against each other (point 3 above). From Eq. (III.19), this cancellation requires (in the decoupling/large t_β limit) $\mathrm{sgn}(Z_{H_u}) = \mathrm{sgn}(Z_{H_d})$. This condition for cancellations to be possible was first noted in [88]. Using DarkSUSY we have confirmed that this is a necessary condition, not just in this limit, but for any values of the pseudo-scalar Higgs mass (m_A) and t_β. This condition only occurs for certain signs of M_1, M_2 and μ. If large SD/small SI were observed for neutralino DM, this would constrain the signs in the neutralino mass matrix.

Let us estimate the maximum allowed suppression. To good approximation[1], the best one can do is to tune away the coupling to (for example) the proton:

$$\frac{c_u}{m_u} = -\left(\frac{f_{Td}^{(p)} + f_{Ts}^{(p)} + \frac{2}{27}\,f_{TG}^{(p)}}{f_{Tu}^{(p)} + 2\,\frac{2}{27}\,f_{TG}^{(p)}}\right)\frac{c_d}{m_d} \equiv -f_{d/u}^{(p)}\,\frac{c_d}{m_d} \approx -1.64\,\frac{c_d}{m_d}. \tag{III.35}$$

[1]From Fig. 3.6 the absolute minimum of the total SI cross section occurs between the region where the coupling to the proton and neutron vanish. Therefore, the following analytic estimate will be off by a factor of a few.

In order for Eq. (III.35) to have a guaranteed solution requires independent control of α and m_H. Since there is a non-trivial relationship between α and m_H (both are determined by m_A), our lower bound provides a conservative estimate. Using Eq. (III.8) to estimate c_q and plugging in the relationship between c_u and c_d from Eq. (III.35) gives $\sigma^p_{\rm SI} = 0$ and

$$\begin{aligned} \sigma_{\rm SI} &= \sigma^n_{\rm SI} = \frac{4}{\pi}\, m_n^2\, \frac{(A-Z)^2}{A^2}\, m_r^2\, y_\chi^2\, \frac{1}{m_h^4} \\ &\left(\left(f^{(n)}_{Tu} + 2\,\frac{2}{27}\, f^{(n)}_{TG}\right)\, f^{(p)}_{d/u} - \left(f^{(n)}_{Td} + f^{(n)}_{Ts} + \frac{2}{27}\, f^{(n)}_{TG}\right)\right)^2 \qquad \text{(III.36)} \\ &\approx 8\times 10^{-13}\,\text{pb}\left(\frac{115\,\text{GeV}}{m_h}\right)^4 \left(\frac{y_\chi}{0.1}\right)^2 \qquad \text{(SI with cancellations).} \qquad \text{(III.37)} \end{aligned}$$

This gives an estimate for how small SI can be, absent taking some of $M_1, M_2, \mu \to \infty$. The effects of the current uncertainties on the hadronic matrix elements described in Sec. 3.1.1 can change change the amount of cancellation allowed (the coefficient in Eq. (III.35)), altering the lower bound in Eq. (III.37) by $\mathcal{O}(50\%)$.

In Fig. 3.6 we show the SI cross section on the proton, the neutron and both as a function of m_A for a 93 GeV neutralino with a thermal relic density of $\Omega_{\rm DM}\, h^2 = 0.1$, $\sigma^p_{\rm SD} = 9\times 10^{-4}$ pb and $\sigma^n_{\rm SD} = 6\times 10^{-4}$ pb. One can clearly see that both contributions to SI DD cannot both be canceled simultaneously. At the minimum, $\sigma^{\rm min}_{\rm SI} = 3\times 10^{-12}$ pb for $m_A = 751$ GeV. For a shift in m_A of $\sim 5\%$, the cross section becomes $\sim 2\times 10^{-10}$ pb – a change of almost 2 full orders of magnitude. This emphasizes the delicacy of the cancellation. Other than in the limited region where the cancellation occurs, the entire range is probeable by the next generation of SI experiments.

Numerically, we find that for $\sigma_{\rm SD} > 10^{-4}$, the smallest $\sigma_{\rm SI}$ can be is $\mathcal{O}(10^{-14}\,\text{pb})$ where the suppression beyond the value in Eq. (III.37) is due to small mixing angles.

Finally , we note that while these kinds of conspiracies are allowed, there is no reason to expect that the SUSY breaking parameters have anything to do with the nuclear matrix elements. We take this as evidence that such cancellations are unlikely.

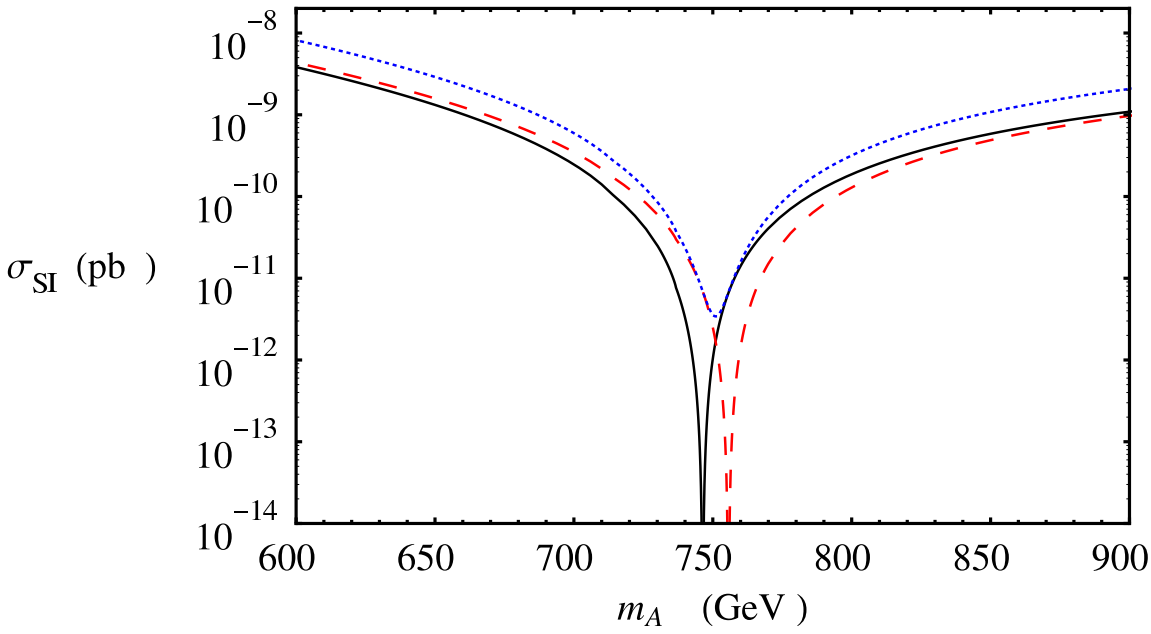

Figure 3.6: Plot of the SI DD cross section for the neutralino scattering off of a proton (solid), a neutron (dashed) and both (dotted) as a function of m_A. For reference, the size of the SD cross section is about 9×10^{-4} pb (proton) and 6×10^{-4} pb (neutron) and $m_\chi = 93$ GeV. The thermal relic density is $\Omega_{\rm DM}\, h^2 = 0.1$. The minimum value for the total SI DD is $\sigma_{\rm SI}^{\rm min} = 3 \times 10^{-12}$ pb for $m_A = 751$ GeV. By changing m_A by 5%, the cross section becomes $\sim 2 \times 10^{-10}$ pb. For small m_A the cross section is on the order of $\sigma_{\rm SI} \sim 10^{-7}$ pb and in the decoupling limit the cross section is on the order of $\sigma_{\rm SI} \sim 10^{-9}$ pb – the entire region where there are not any conspiratorial cancellations is within the reach of the next generation of SI experiments.

To conclude, in this chapter we have explored the physics of SD DD with an emphasis on the correlations with SI experiments. In the process, we have determined some expectations for the SD cross sections. In particular, in the MSSM, $\left(\sigma_{\rm SD}^{\rm SUSY}\right) < 6 \times 10^{-3}\,$pb without making any assumptions about the thermal history. Again, allowing for a non-trivial cosmic history, but imposing the unified gaugino mass condition, we find $\left(\sigma_{\rm SD}^{\rm SUSY}\right) < 4 \times 10^{-3}\,$pb. Finally, $\left(\sigma_{\rm SD}^{\rm SUSY}\right) < 2 \times 10^{-3}\,$pb when a thermal relic density is imposed. These represent important targets for future experiments. We note that if SD cross sections larger then $\sim 6 \times 10^{-3}\,$pb were observed, the DM would not be an MSSM neutralino. This would point to more exotic theories like the SDM or models with light mediators [57]. For models which reproduce the relic density, in the decoupling limit, and unified gaugino masses, a 1-ton

COUPP-like experiment could probe the entire range of SD cross sections up to WIMP masses of $\mathcal{O}(1\,\mathrm{TeV})$.

CHAPTER IV

Annihilations to a new, heavy lepton

If PAMELA positron results are indeed signals of dark matter and the antiproton background corresponds to that of conventional models, the dark matter particle annihilates primarily to leptons. Construction of a dark matter candidate that primarily annihilates directly to leptons is non-trivial. Majorana fermions have helicity suppressed annihilations to light fermions, and Dirac fermions face significant model building challenges [116]. However, one can consider new annihilation modes into non-Standard Model states, which then subsequently decay to leptons. Such models can be divided into two categories. In the first approach, dark matter annihilates to light intermediate particles. If sufficiently light ($\sim$ GeV), the absence of anti-protons can be explained by simple kinematics [67] (see also [25, 184, 174, 65, 175]). A second approach is for the dark matter to preferentially couple to leptons via dynamics [95]. Alternative models have considered the possibility where dark matter decays preferentially to leptons [61, 59, 114, 127, 26, 60, 128, 217, 219].

Here we present a hybrid approach. Dark matter dominantly annihilates to final states involving new, heavy particles. These particles mix with the Standard Model leptons, and so carry lepton number. Following the decay of these new particles, dark matter annihilations produce hard leptons in association with gauge bosons. The annihilation spectra from this model are distinct from those previously included in the literature thus far.

In the next section we discuss the general framework for dark matter annihilations and heavy lepton decays. The scenario is a very simple extension of the Standard Model. In section III, we calculate the cosmic ray fluxes from dark matter annihilations and the boost factor relative to the thermal cross section. We find this scenario can explain the PAMELA excess with a small boost factor. In section IV, we discuss the possible observation of high energy neutrinos from dark matter annihilations. In section V, we discuss the possible production of new vector leptons at the LHC, and their signatures. In section VI we construct extensions of the Standard Model and Supersymmetric Standard Model which realize this scenario. Finally, we conclude.

4.1 Annihilations of dark matter into a New, Heavy Lepton

The PAMELA data do more than confirm the excess seen by HEAT [39] and AMS-01 [11]. The sharp upturn in the positron fraction seems to disfavor annihilations with hadronic modes, because the positrons from a hadronic shower are generally too soft to produce such a spectrum. Furthermore, such showers contain anti-protons, and no excess is observed in this channel. Thus, to reproduce the positron/electron ratio and the antiproton/proton ratio observed by PAMELA, dark matter annihilations should produce a larger ratio of high energy positrons to antiprotons than annihilations to vector bosons [1].

We propose a new mechanism to achieve this. We assume dark matter annihilation proceeds via the processes in Figure 4.1. The dark matter particle, χ, annihilates through new channels which involve heavy vectorlike states, $\Xi/\bar{\Xi}$, which carry lepton number and thus subsequently decay into light leptons and W or Z bosons.

This theory can explain the PAMELA signal. The introduction of new, heavy leptons allows direct annihilation into leptonic states which are not suppressed by a small fermion mass. This can occur either from direct annihilations to heavy leptons alone (i.e. through

[1] See, however, [108] for a discussion of whether uncertainties in propagation parameters might accommodate annihilation to gauge bosons.

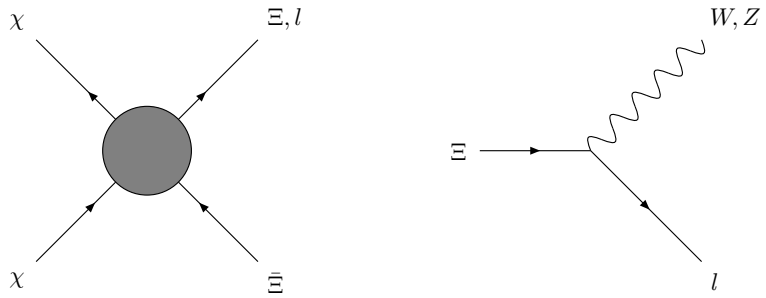

Figure 4.1: *Left:* The annihilation process of the dark matter χ to a heavy $\bar{\Xi}$ lepton and either Ξ or a Standard Model lepton l. The shaded circle represents a model-dependent annihilation mechanism. We discuss possibilities for this in section 4.5. *Right:* Decay of the Ξ into to a lepton and a W or Z boson.

a $\chi\chi\bar{\Xi}\Xi$-type operator) or from a combination of new heavy leptons and light leptons (through a $\chi\chi\bar{\Xi}l_i$-type operator). Because we do not rely upon a helicity flip on the external line, such processes can be large and dominate the annihilation rate. We will not specify the mechanism by which the annihilation proceeds for now, but will revisit this question. (A similar annihilation to a heavy/light pair can occur in RS theories, although with different masses and spectra than we consider here [182].)

Under $SU(2)\times U(1)$ the Ξ can have quantum numbers $(\mathbf{2}\,,\mathbf{1/2})$ (like a Standard Model ℓ), $(\mathbf{1}\,,\mathbf{1})$ (like a Standard Model e^c), or $(\mathbf{1}\,,\mathbf{0})$ (a complete Standard Model singlet, n). Any of these is viable, but they have distinct phenomenology.

In the case where we add vectorlike particles with quantum numbers of e^c or n, decays proceed with comparable rates both through W and Z bosons[2]. Thus, for $\chi\chi\to\Xi\bar{\Xi}$, each annihilation (on average) roughly yields a single charged lepton and two gauge bosons. In contrast, as we shall see, annihilation to a pair of vectorlike heavy doublets ultimately yields final states with charged leptons and gauge bosons in a one to one ratio. Since gauge bosons are a source of anti-protons, taking Ξ as a vectorlike $SU(2)_L$ doublet produces the highest $e^+/\bar{p}$ signal, as is desirable to fit the PAMELA data.

For the study of cosmic ray signals, then, we will focus on the ℓ-like case. For the purpose

[2]We thank Tom Rizzo for a discussion of this point.

of the PAMELA data, the consequence of considering the n- or e^c-like models instead is to multiply the $\bar{p}$ spectrum of the case at hand by a factor of ~ 2, as an increased boost factor would be needed to fit the positron data (see section 4.2).

For concreteness, we begin with a Lagrangian[3]

$$\mathcal{L} = \sum_i y_i \ell_i e_i^c h + \mu \bar{\Xi}\Xi + \epsilon_i \bar{\Xi}\ell_i + \tilde{y}_i \Xi e_i^c h + H.c. \tag{IV.1}$$

Prior to electroweak symmetry breaking, we can do a rotation in $(\ell_i\, \Xi)$ space to remove the ϵ_i terms at the cost of modifying the $\tilde{y}_i$ terms. Subsequent rotations on the ℓ_i and e_i^c allow diagonalization of the 3×3 submatrix. After electroweak symmetry breaking and performing the above rotations, the charged and neutral fermion mass matrices are

$$\text{(IV.2)}\ \mathbf{M_{charged}} = \begin{pmatrix} m_e & 0 & 0 & 0 \\ 0 & m_\mu & 0 & 0 \\ 0 & 0 & m_\tau & 0 \\ \tilde{m}_e & \tilde{m}_\mu & \tilde{m}_\tau & \mu \end{pmatrix}, \qquad \mathbf{M_{neutral}} = \begin{pmatrix} 0 \\ 0 \\ 0 \\ \mu \end{pmatrix}.$$

Physical neutrino masses are sufficiently small that we can neglect them. There is no *a priori* reason why $\tilde{m}_e \leq \tilde{m}_\mu, \tilde{m}_\tau$. In anarchical models[113], they may all be the same, or should Ξ carry a lepton flavor charge, it could even be that $\tilde{m}_e \gg \tilde{m}_\mu, \tilde{m}_\tau$. For future discussion, it is useful to introduce the small parameter $\delta_i \equiv \tilde{m}_i/\mu$.

4.1.1 Decays of the heavy leptons

Let us begin by focusing on the phenomenology of the neutral sector. All neutral states (both Standard Model and the new heavy state) have identical couplings to the gauge bosons. So, when the mass matrix is diagonalized, no off-diagonal couplings to the Z boson are created — the mathematics is identical to that which ensures the absence of FCNCs in the Standard Model. However, the differences in diagonalizing the charged

[3] A similar Lagrangian can be constructed for the situation where Ξ is neutral (see, for instance, [58]).

lepton mass matrices *will* lead to off-diagonal charged current decays. Thus, neutral Ξ states decay to a $W^{\pm}\ell^{\mp}$ final state.

The decay modes of $\Xi^{\pm}$ are more complicated. We assume that the $\Xi^{\pm}$ state is heavier than the Ξ^0 state. The charged state has non-vanishing couplings to three final states: $\Xi^0 W^{\pm *}$, $Z\ell^{\pm}$, and $W^{\pm}\nu$. Typically, the most suppressed of these decays is the decay to $W^{\pm}\nu$. This heavy–light charged current coupling is down by a factor $(m_\ell/\mu)\delta_i$, where m_ℓ is the relevant charged lepton mass. Were m_ℓ to vanish, then the rotation on the left-handed doublet has no effect (just as in the neutrino case above). This is the origin of the suppression. Thus, the two decay modes of potential phenomenological interest are $\Xi^0 W^{*\pm}$ and $Z\ell^{\pm}$. The first of these receives no suppression from small couplings, but receives a large phase space suppression. If no additional couplings are added to the theory, the dominant contribution to the $\Delta m_\Xi \equiv m_{\Xi^\pm} - m_{\Xi^0}$ mass splitting is from the loop effect induced by the Coulomb interaction, analogous to $\pi^\pm - \pi^0$ mass splitting. Because this effect is cut-off by the scale of electroweak symmetry breaking, it is finite and is approximately given by $\Delta m_\Xi \approx \frac{\alpha M_Z}{2} \approx 350$ MeV. There is an additional (subdominant) contribution to the splitting between the charged and neutral states of size $\delta^2\mu$ due to the mixing with the Standard Model states. We will see later that δ is constrained to be $\lesssim 10^{-2}$. For the tiny splittings induced by the Coulomb interactions, decays will proceed to Ξ^0 and a soft charged pion with a rate given by [211]

$$\Gamma_{\pi\Xi^0} = G_F^2 \cos^2\theta_C f_\pi^2 (\Delta m_\Xi)^3 \sqrt{1 - \left(\frac{m_\pi}{\Delta m_\Xi}\right)^2}. \tag{IV.3}$$

The remaining decay, $\Xi^{\pm} \to Z\ell^{\pm}$, is unsuppressed kinematically, but the relevant coupling is proportional to δ. It is given by

$$\Gamma_{\ell Z^0} = \frac{m_\Xi \delta^2 g^2}{64\pi \cos^2\theta_W} \left(1 - \left(\frac{m_Z}{m_\Xi}\right)^2\right)^2 \left(2 + \left(\frac{m_\Xi}{m_Z}\right)^2\right). \tag{IV.4}$$

For $\delta > 10^{-7}$, the kinematic suppression of the charged current decay is more severe, and

the decay via $\Xi^{\pm} \to Z\ell^{\pm}$ dominates. In the remainder of the paper, we will assume that δ is sufficiently large so that $\Xi^{\pm}$ decays in this way.

4.1.2 Spectrum of annihilation products

We first consider the case when the dark matter dominantly annihilates into two heavy states. It is natural to assume the dark matter annihilates equally into $\Xi^{+}\Xi^{-}$ and $\Xi^{0}\Xi^{0}$. Based on the above discussion, these processes yield $\ell^{+}\ell^{-}ZZ$ and $\ell^{+}\ell^{-}WW$ final states. In principle, the mixing of the new vectorlike state can be with any Standard Model lepton family. Not surprisingly, the case where mixing is dominantly into electrons provides the most favorable to fit the PAMELA positron spectrum: it produces the hardest positron spectrum possible for a certain amount of antiprotons. Mixing with μ and τ leptons will require larger boost factors to produce the positron signal and will result in some tension with the anti-proton data.

We now address the spectrum that results from dark matter annihilation. It depends on the masses m_{χ} and m_{Ξ}. In the limit $m_{\Xi} \to m_{\chi}$, the spectrum decomposes into two components: gauge bosons of energy $\sim m_{\chi}/2$ (assuming $m_{\Xi} \approx m_{\chi} \gg m_{V}$) and electrons and positrons of energy $m_{\chi}/2$. Here m_{V} is the mass of the relevant gauge boson. In the opposite limit, $m_{\chi} \to m_{V}$, the energy of the positron from the Ξ decay goes to zero. The most relevant positrons come directly from gauge boson decay will have maximum energy m_{χ}. Finally, one finds the hardest electron/positron spectrum for the lepton from Ξ decay comes for

$$m_{\Xi} = \sqrt{2m_{\chi}m_{V} - m_{V}^{2}}. \tag{IV.5}$$

The spectra for these three limits are shown in Fig. 4.2.

The addition of two hard leptons to every annihilation allows a fit to the observed positron fraction with a smaller boost factor than would be required if annihilation proceeded directly to gauge bosons. This provides a relative suppression of the antiproton

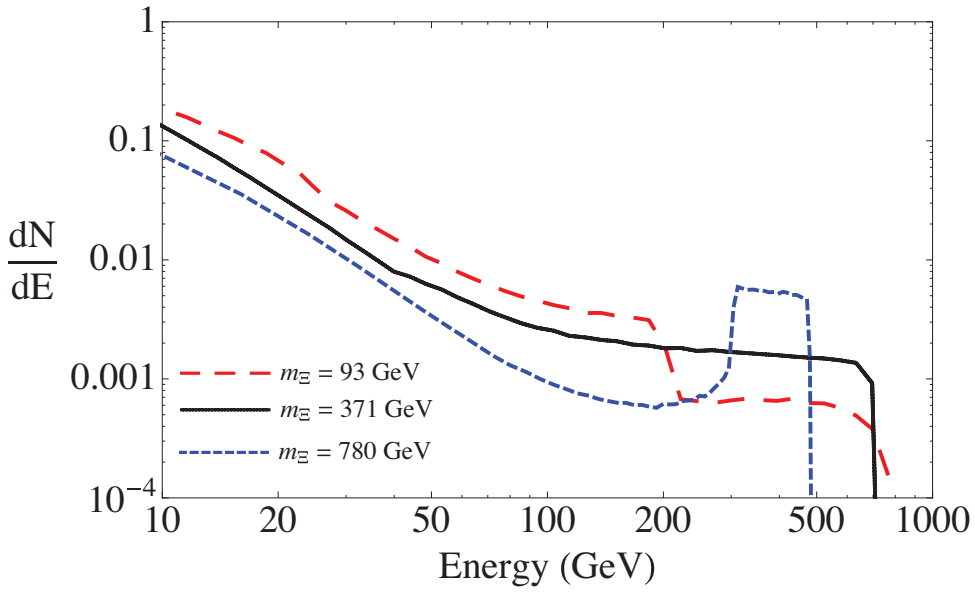

Figure 4.2: Positron spectra from the process $\chi\chi \to \Xi\bar{\Xi}$ for three different Ξ masses for a dark matter mass $m_\chi = 800$ GeV. These injection spectra are shown prior to propagation and correspond to a single annihilation. It is assumed that the Ξ decay via a mixing with electrons.

contribution. This is roughly an order of magnitude change with respect to the case of pure annihilation to gauge bosons. Residual $\bar{p}$'s will still provide a constraint. We will explore this in section 4.2.

Next, we consider the case where dark matter annihilates into one heavy and one light lepton. Similar final states occur in Randall-Sundrum theories of dark matter [182]. Again, the natural assumption is that dark matter annihilation populates the charged and neutral states equally. As long as $m_\Xi \lesssim 2m_\chi$, the Ξ final state is available. In this limit ($m_\Xi \to 2m_\chi$), no kinetic energy will be available for the $\Xi\ell$ final state. Thus, the monochromatic light lepton is soft. Effectively, the final state is a Ξ field at rest, which then decays as described in the previous section. In the opposite limit of a very light Ξ, there is a combination of a hard monochromatic lepton plus a Ξ decay spectrum. We plot the positron injection spectrum in three cases, $m_\Xi = 95$ GeV, $\approx m_\chi$, and $\approx 2m_\chi$ in Fig. 4.3 for the case where the final state lepton is an electron. In this heavy–light case, a monochromatic

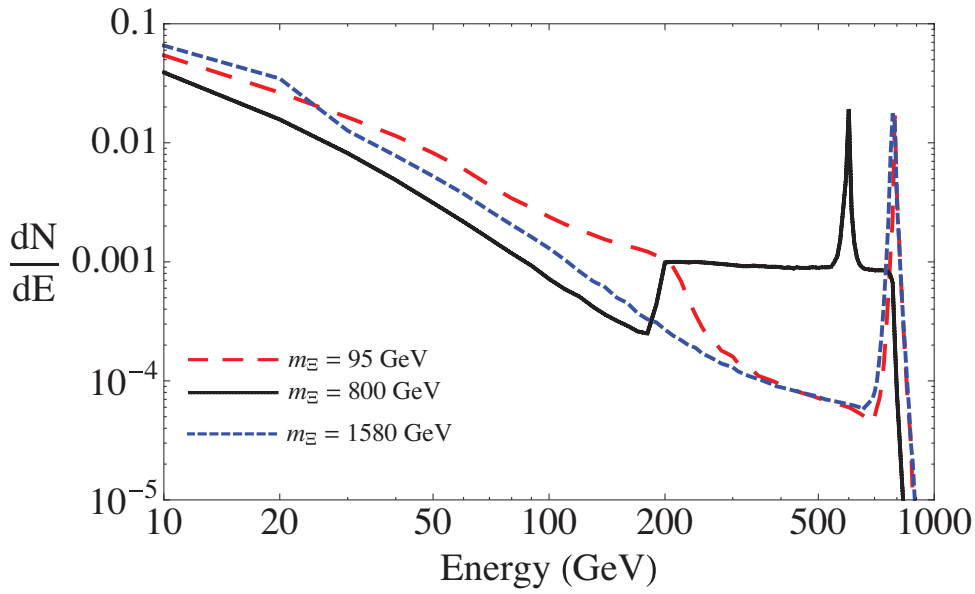

Figure 4.3: Positron spectra from the processes $\chi\chi \to \Xi e$ for a dark matter mass $m_\chi = 800$ GeV and three different Ξ masses. These injection spectra are shown prior to propagation, and correspond to a single annhilation.

neutrino is also produced. We will discuss its consequences in Section IV.

4.1.3 Precision Constraints

Although we introduce new states that mix with Standard Model leptons, it is obvious from the outset that there need be no conflict with precision observables. If the mixing with the Standard Model (as controlled by $\delta = \tilde{m}/\mu$) is sufficiently small, there will be no measurable effect on, *e.g.*, $g-2$, although Ξ will still decay on (cosmologically) short timescales. However, to understand the phenomenology of the heavy states, it is important to consider how large δ can be.

In the case of a vectorlike doublet, there are two relevant classes of constraints. First, if both δ_μ and δ_e are non-zero, a bound arises from the process $\mu \to 3e$. Consistency with the non-observation of this process $BR(\mu \to 3e) < 10^{-12}$ [44] forces $\sqrt{\delta_e \delta_\mu} < 2 \times 10^{-3}$. A weaker constraint arises on this combination from $\mu \to e\gamma$. Second, there are constraints present even if only one δ is non-zero. In particular, there are precision electroweak con-

straints from considering, e.g., the universality of $\Gamma(Z \to \ell\ell)$. This forces $\delta_\ell < 2 \times 10^{-2}$.

Should we choose the vectorlike state to instead have the quantum numbers of a right-handed electron, there is also an important bound that comes from the universality of G_F. In that model, the $SU(2)_L$–singlet exotic is mixed with a standard model lepton and effectively reduces the coupling of this light state to the W. Thus, for the singlet model there is an additional constraint, $\delta_\ell < 4 \times 10^{-3}$.

So, there is a large window (roughly $10^{-7} < \delta < 10^{-2}$), where the decay phenomenology described in the previous section applies and is consistent with all precision constraints. We assume that we are in this window and now move to a detailed discussion of the astrophysical signals of this model.

4.2 Explaining the PAMELA results

While we have presented a simple scheme for generating hard positrons with few antiprotons, it remains to be seen whether we can fit all of the existing data, and what the minimal boost factor above the thermal cross section is required to reproduce a good fit.

To investigate the annihilation spectra, we implemented the processes described in section 4.1 into MadGraph [156]. This allowed the simulation of the annihilation and decays shown in Fig. 4.1. Subsequent decays of the W and Z bosons and hadronization where done with PYTHIA [200]. This produced an injection spectrum of positrons, electrons, antiprotons, and gamma rays. This spectrum was input to GALPROP [205] to propagate the decay products through the galaxy. For concreteness, an NFW profile was used [173]

$$\rho(r) = \rho_\odot \left(\frac{r_\odot}{r}\right) \left(\frac{1 + (r_\odot/r_s)}{1 + (r/r_s)}\right)^2, \tag{IV.6}$$

with $r_s = 20$ kpc, where $r_\odot = 8.5$ kpc is the galactocentric distance of the sun and $\rho_\odot = 0.3$ GeV/cm^3 is the local dark matter density, although the shape of the profile will have little effect on the observed positron fraction. For positron, electron, proton, and antiproton

flux backgrounds, we use the model described in [67] with the Alfvén velocity $v_A = 20$ km/s. The diffusion coefficient is taken to be $D = \beta(5.88 \times 10^{28}\ \mathrm{cm}^2/\mathrm{s})\ (\mathrm{R}/4\ \mathrm{GV})^{1/3}$, where $\beta = v/c$ and R is the rigidity. The height of halo region is set to $L = 4$ kpc.

There are a number uncertainties that enter into the calculation of the rates. In addition to the cross section itself, indirect detection signals are proportional to the number density squared of dark matter particles. The uncertainties associated with this are usually encoded into a "boost factor". We define the boost factor as

$$BF = \frac{1}{V_{CR}} \left(\int d^3x \frac{n^2_{true}(r)}{n^2(r)} \frac{\langle \sigma v \rangle}{\langle \sigma v \rangle_{thermal}} \right). \tag{IV.7}$$

Here $n(r) = \rho(r)/m_\chi$ is the previously mentioned NFW profile with local density $\rho_0 = 0.3\,\mathrm{GeV\ cm}^{-3}$. $n_{true}(r) = \rho_{true}(r)/m_\chi$ is the actual (possibly clumpy) number density of the dark matter particles in the halo, and the integration is over a region V_{CR} defined by cosmic ray propagation.

The integral over the number density contains all of the information on astrophysics and is subject to both uncertainty in the halo profile and uncertainties on propagation. Clumpiness gives an increase in n^2 when compared to a smooth profile. Should the boost factor arise from astrophysics, it is expected that the boost factors could be different for positrons and antiprotons. Depending on the positions of subhalos with respect to the solar position, it could lead $BF_{e^+}/BF_{\bar{p}} \sim 3$ [146] and energy dependent boost factors. We will ignore the possibility of energy dependent boost factors in this work, but will bear in mind the possibility that astrophysical uncertainties might somewhat ameliorate tensions between positrons and anti-protons. Note that uncertainties in the local number density could be a factor of ~ 2 (yielding a boost of ~ 4) [46, 16]. Altogether, boosts of up to ~ 10 arising from astrophysics alone are likely reasonable, while much higher boosts (as we shall find are necessary for heavier WIMPs) likely would rely on a contribution from a non-trivial dark matter cosmology.

It should also be noted that uncertainties in the propagation of antiprotons could suppress the dark matter contribution to the antiproton signal by up to an order of magnitude [82]. The effects of these changes on the positron flux is more modest. So, while in this work we quote a boost factor for the positron signal and naively apply the same the boost factors to the anti-protons, it should be kept in mind that masses that initially appear to be ruled out by the observed $\bar{p}/p$ ratio might be allowed once a full accounting of these uncertainties is made.

We show the results of our analysis in Fig. 4.4. We find that it is possible to fit the PAMELA positron data for a variety of masses. For each set of masses, we find the boost factor (as defined above) that gives the best fit to the data. To avoid the complications of solar modulation [185, 69], we perform a χ^2 fit to only the four highest energy bins of the PAMELA data (where solar modulation is known to have little effect). The results are the boost factors shown in Fig. 4.4. Since PAMELA data were taken during a negative polarity part of the solar cycle, correcting for modulation would reduce positron ratio at lower energies, bringing the curves into qualitatively better agreement with the data.

The smallest dark matter mass found to be consistent with the PAMELA positron data is $m_\chi = 200$ GeV with $m_\Xi \gg m_W$. In this case, the boost factor required is only 6, which could very plausibly be entirely due to astrophysics. Thus, dark matter signals could result from a thermal annihilation cross section with no need for non-thermal production or late time cross section enhancements. As m_χ increases, the boost factor required is increasingly unlikely to be given by astrophysics alone, and an increase in the annihilation cross section beyond the thermal one is likely necessary. This could be consistent, for example, with a cosmological history where the dark matter is produced non-thermally, or if the late-time properties of the dark matter change [70]. If Ξ decays to muons or tau leptons, this will produce a softer positron spectrum and will require boost factors to fit the positron data.

These will come into more tension with the antiproton data. For muons, the difference is roughly a factor of two from the electron case.

Dark matter masses $m_\chi \sim 500$ GeV are in tension with the antiproton data. Keeping in mind the earlier caveats mentioned on astrophysical uncertainties (both propagation and clumpiness), a prediction of this model is that the dark matter have mass less than 500 GeV. A turn-over or plateau in the positron fraction should be imminent. A reasonable fit to both the $\bar{p}$ and positron data is possible in the case where the Ξ dominantly mixes to muons for $m_\chi < 400$ GeV.

When annihilation occurs via $\chi\chi \to \Xi e$, the positron spectra have slightly cuspier shapes than when annihilation proceeds through $\chi\chi \to \Xi\bar{\Xi}$, see Fig. 4.5. The boosts required are similar to the $\Xi\bar{\Xi}$ case, and the fits are comparably good. Annihilations via $\chi\chi \to \Xi\mu$ can also give good fits, but require somewhat larger boosts, leading to some tension with anti-proton results, even for lower dark matter masses. A dark matter mass of $m_\chi = 200$ GeV that decays in this way is marginally consistent with the positron and antiproton observations for a boost factor of 10-20, depending on the Ξ mass.

Finally, if $\chi\chi \to \Xi\bar{\Xi}$ annihilation dominates, a choice of $m_\chi = 800$ GeV and $m_\Xi = 370$ GeV allows a qualitative fit to the shape and position of the Fermi data [3], demonstrated in Fig. 4.6. In this figure, the background is scaled such that it saturates the low energy data. While the signal does not reproduce the Fermi data precisely, we find this qualitative fit encouraging. If the Fermi anomaly is from dark matter, and this model is to explain it, this points to a $m_\chi = 800$ GeV to 1 TeV dark matter particle with a large boost factor, $\sim$35. This is lower than the boost factor required for fits to the PAMELA positron fraction, however it does ease the tension with the antiproton data (Fig. 4.4).

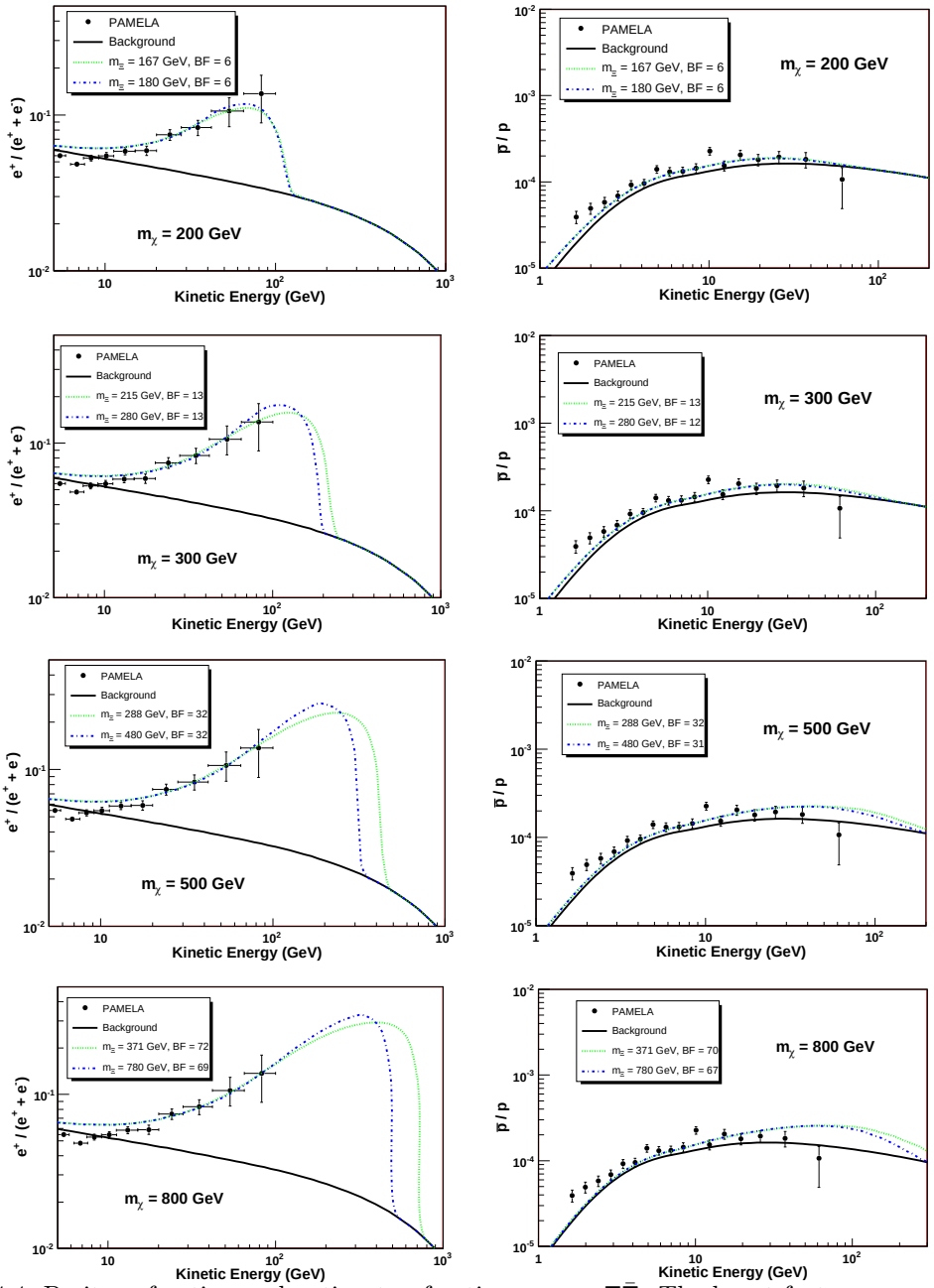

Figure 4.4: Positron fraction and antiproton fractions $\chi\chi \to \Xi\bar{\Xi}$. The boost factors are relative to $3 \times 10^{26}\,\mathrm{cm}^3/\mathrm{s}$, and are found by scaling the positron flux to fit the observed positron fraction. In the m_χ =200, 300 GeV cases, the boost factor required is sufficiently small that the dark matter might have a thermal relic abundance.

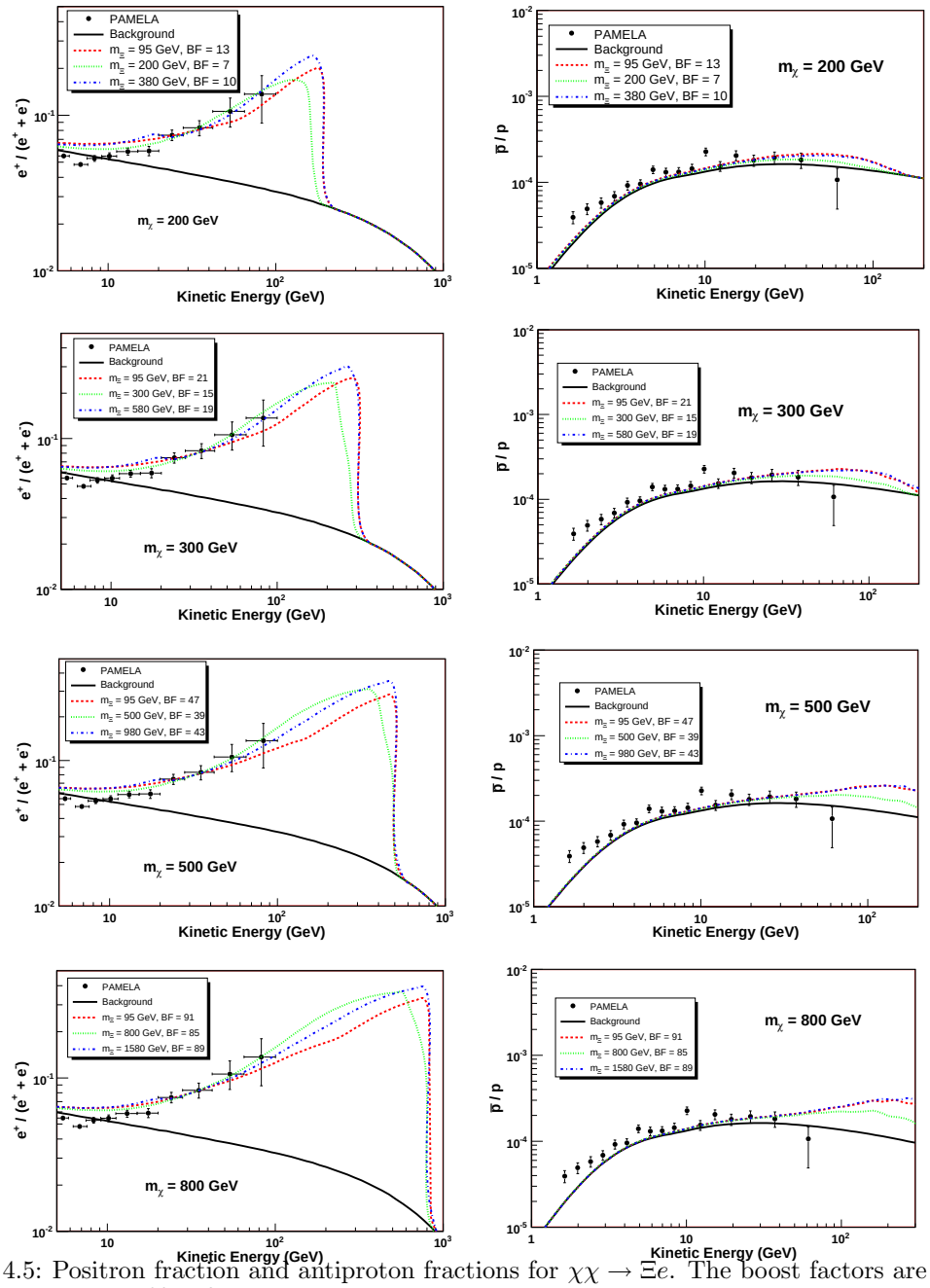

Figure 4.5: Positron fraction and antiproton fractions for $\chi\chi \to \Xi e$. The boost factors are relative to $3 \times 10^{26}\,\mathrm{cm}^3/\mathrm{s}$, and are found by scaling the positron flux to ft the observed positron fraction. In the $m_\chi = 200$ GeV case, the boost factor required is sufficiently small that the dark matter might have a thermal relic abundance.

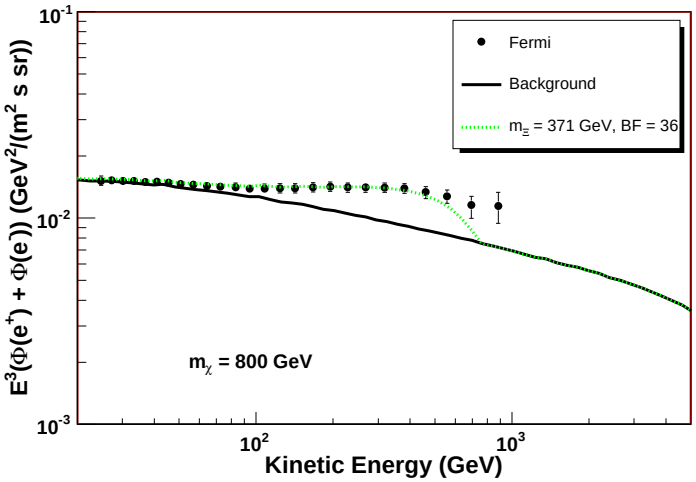

Figure 4.6: ATIC signal for $m_\chi = 800$ GeV and $m_\Xi = 371$ GeV. The background has been scaled to saturate the low energy total flux. The required boost factor is 36, indicating a non-standard cosmological history for the dark matter.

4.3 Neutrino Signals

The detectability of neutrino signals, in particular as related to models to explain PAMELA has recently been studied [40, 118, 151]. Upcoming experiments such as IceCube [14] and ANTARES [10] could potentially show sensitivity.

If annihilation proceeds as $\chi\chi \to \Xi\bar{\Xi}$, with Ξ an electroweak doublet, there are essentially no hard neutrinos produced. However, in the case that annihilations proceed $\chi\chi \to \ell\bar{\Xi}$, such processes will produce equal numbers of monochromatic charged leptons and neutrinos. This monochromatic ν presents an exciting experimental target.

The background from cosmic ray neutrinos [120] can be well modeled by a power law. Following [40], we examine the signal at a neutrino telescope by requiring a signal to background ratio of 1 in a bin from $10^{-.5}m_\chi$ to m_χ when compared with the angular average of $\nu_\mu + \bar{\nu}_\mu$. We assume that oscillations yield 1/3 of all neutrinos as muon flavor. The signal is proportional to the line-of-sight integral of the dark matter density averaged over the relevant solid angle, $J_{\Delta\Omega}$. We calculate $J_{\Delta\Omega}$ of 680 for a 2° region around the

galactic center in an NFW profile. This solid angle corresponds to the angular resolution of ANTARES. Taking this gross analysis requiring S:B=1, we find that a detectable signal can be found for boosts of roughly 320[4].

Such a limit depends only weakly on the dark matter mass (assuming $\mu \ll m_\chi$), although for very large neutrino telescopes where the background statistics are large enough to model the background, the appropriate comparison is naturally $S/\sqrt{B}$ and greater sensitivity would be possible. For reference, in ten years of IceCube running we expect 200 background events from 500-1000 GeV in a 2° region[151]. Thus, without a careful examination of background models, we cannot say how detectable this scenario would be at lower masses. For higher masses, detection will be statistics limited, and the S:B criterion is the right one. This case seems borderline in its detectability. Ruling out this model with neutrinos seems difficult. That said, there is substantial evidence within numerical simulations for many subhalos in the Milky Way[76, 77, 203]. Should one of these provide a larger $J_{\Delta\Omega}$, for instance by being cuspy or very nearby, a positive detection remains tantalizingly possible. IceCube has good angular resolution and could focus on one of these regions in an effort to suppress the atmospheric neutrino background.

In fact, if this substructure is sufficiently generous, then it might be possible to observe the ν's produced in the case where the Ξ is an $SU(2)_L$ singlet, but dark matter annihilations go to $\Xi\bar{\Xi}$. In this case, the neutrinos have a spectrum very similar to that seen for positrons in Fig. 4.2. They have energy roughly a factor of two lower than the case where direct $\Xi\nu$ dominates. Due to the steeply falling power law nature of the background, these neutrinos would have to be visible over a background roughly an order of magnitude higher.

Lastly, we should note that the observability of the galactic center signals rely on cuspy profiles into the inner 2°. Should those profiles extend into the inner $\sim 0.5°$, strong gamma ray limits from HESS may constrain possible neutrino signals [153, 50, 47, 163].

[4]Here the boost refers specifically to the cross section into $\nu\bar{\Xi}$ rather than the total cross section.

4.4 Collider Signals

While dark matter signals are often elusive at a collider, we have the exciting possibility of directly producing the new Ξ states that dominate dark matter annihilation. The cases where the Ξ has quantum numbers of a leptonic doublet or a right-handed electron are interesting. These states will be produced via the Drell-Yan process. The collider phenomenology of the case where the Ξ is a complete Standard Model singlet is uninteresting, simply because it will not be produced at an important level.

First, we consider the doublet case. Production of $\Xi^+\Xi^-$, $\Xi^0\Xi^0$, and $\Xi^\pm\Xi^0$ are possible. The production of $\Xi^+\Xi^-$ leads to a $ZZ\ell^+\ell^-$ final state. The cross section at the LHC for this mode is 27 fb at $m_\Xi = 200$ GeV. In 300 fb^{-1}, we expect ~ 50 six lepton events, with 4 leptons reconstructing to a pair of Z bosons. While very few events are expected, they would be spectacular; irreducible physics backgrounds in this channel are vanishingly small. In addition, one could expect observation in the $(ZZ\ell\ell \to 4\ell + 2j)$ mode and perhaps even the $2\ell+4j$ mode. We estimate the background in the $4\ell+2j$ case to be 9 fb from ALPGEN [159] using the process $ZZjj \to 4\ell jj$. These backgrounds could be substantially reduced by requiring that the jets reconstruct a Z and applying a Z veto on one of the pairs of leptons. Lepton flavor tagging could also additionally suppress backgrounds. Before cuts, we expect ~ 500 4ℓ+2j signal events in 300 fb^{-1} for $m_\Xi = 200$ GeV. Assuming these cuts reduce the background by a factor of a few without compromising the signal, this will give a S:B$\sim$1. The signal would fall to ~ 180 events in 300 fb^{-1} at $m_\Xi = 300$ GeV. At the Tevatron, the cross section for $\Xi^+\Xi^-$ production for $m_\Xi = 200$ GeV is 1 fb, too small to be seen.

If the mixing between the $\Xi^\pm$ and the Standard Model is very weak, then the $\Xi^\pm$ could be long-lived on detector time scales. However, in the doublet case, the existence of the $\Xi^\pm \to \Xi^0\pi^\pm$ decay mode unsuppressed by δ (Eqn. IV.3), means that the tracks do

not extend much more than a centimeter [211]. This makes observation of these events unlikely. This changes in the case where the $\Xi^{\pm}$ is a SU(2) singlet. Then for sufficiently small mixings, a striking long-lived charged track is possible, as all Ξ decays are suppressed by δ. Depending on the size of δ, there is also a possibility [129, 130] that Ξ could solve the primordial lithium problem. For a choice of δ that allows $\Xi^{\pm}$ to decay around BBN, $\Xi^{\pm}$ would clearly be long-lived on detector time scales. The current bound on the production cross section of such a long -lived particle from the D0 experiment is $\lesssim$ 10 fb[1]. This translates to a lower bound on the mass of a $SU(2)$-singlet $\Xi^{\pm}$ of 120 GeV.

Returning to the doublet case, we turn to Drell-Yan production of $\Xi^0\Xi^0$. This produces a $W^+W^-\ell^+\ell^-$ final state. The cross section at the LHC for Drell-Yan production of the Ξ^0 is 93 fb at $m_\Xi = 200$ GeV. In 300 fb^{-1}, we expect ~ 1300 $4\ell + \not{E}_T$ events. While Standard Model diboson production presents an important background, lepton flavor tagging could provide a helpful discriminant: the Standard Model rate for $3\ell\ell'$ is very much suppressed. It might also be possible to observe this final state in the $3\ell + 2j + \not{E}_T$ channel. The Standard Model background ($\sigma\times$ BR) for this state from WZjj is roughly 200 fb. So, it will be important to impose a Z veto. Fakes from top production could also be important, and more study is warranted.

Finally, $\Xi^{\pm}\Xi^0$ can be produced via an intermediate W boson. This state leads to a $ZW^{\pm}\ell^+\ell^-$ final state, which can ultimately yield striking 5ℓ events. For $m_\Xi = 200$ GeV, the production cross section is 756 fb. For $m_\Xi = 300$ GeV, the production cross section is 176 fb, and for $m_\Xi = 600$ GeV, the production cross section is 12 fb. At the Tevatron the cross section for $\Xi^{\pm}\Xi^0$ production for $m_\Xi = 175$ GeV is 76 fb, and $m_\Xi = 200$ GeV is 4 fb. For the lowest masses, a few multilepton events could be observed.

4.5 Models

One of the appealing aspects of our proposal is that it is simply incorporated into the Standard Model and almost any model of new physics. In this section we will outline more concrete models that might realize this scenario, first in extensions of the Standard Model then in extensions to the minimal supersymmetric Standard Model (MSSM). In each case the basic building blocks are the same: namely, the new leptons states themselves, as well as an annihilation mechanism, which is accomplished with the introduction of a new scalar.

4.5.1 Non-supersymmetric implementation

We begin by considering a non-supersymmetric realization. The vectorlike heavy lepton mixes with the Standard Model leptons as in Eq. (IV.1), and decays via a light lepton and Z boson. The Lagrangian is

$$\mathcal{L} = y_X \chi^2 S + y_\Xi \bar{\Xi}\Xi S + \tilde{y}\bar{e}_{Ri}\Xi h + H.c. - V(S), \tag{IV.8}$$

where we have rotated away a potential mass term $\ell\bar{\Xi}H$. We also introduce a complex scalar $S = s + ia$ with potential

$$V(S) = m_S^2 S^\dagger S + \beta S^\dagger S^2 + \beta^* S S^{\dagger 2} + \lambda_S (S^\dagger S)^2, \tag{IV.9}$$

which has a global $U(1)$ symmetry explicitly broken by β. If we allow a vacuum expectation value for S to give mass to the dark matter and Ξ, then a is a pseudo-Goldstone boson with its mass controlled by the symmetry breaking parameter β. We have neglected a possible $S^\dagger S H^\dagger H$ mixing term. The presence of this term could affect the pseudoscalar phenomenology. While this term will be generated at the loop level, the radiatively generated size is suppressed by two powers of $\tilde{m}/\mu$ and a loop-factor – small enough that it has no significant effects.

We consider the case where the dark matter annihilates through the pseudoscalar a^0. This avoids the suppression by the velocity of the dark matter v^2 that occurs in the case

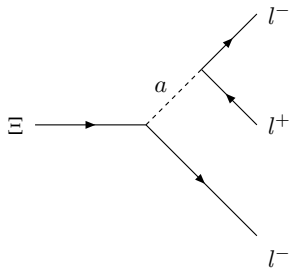

Figure 4.7: Decay of the Ξ into to a lepton and a pseudoscalar a, which subsequently decays to leptons.

of scalar mediation. The annihilation cross section is

$$\langle \sigma v \rangle_{\Xi\Xi} = \frac{y_X^2 y_\Xi^2}{64\pi m_\chi^2} \sqrt{1 - \frac{m_\Xi^2}{m_\chi^2}} \frac{1}{(1 - \frac{m_a^2}{4m_\chi^2})^2 + \frac{m_a^2 \Gamma_a^2}{16 m_\chi^4}}. \tag{IV.10}$$

In the limit that $m_a^2/m_\chi^2 << 1$ and $2m_\Xi \sim m_\chi$,

$$\langle \sigma v \rangle_{\Xi\Xi} \sim \left(5.56 \times 10^{-24} \frac{\mathrm{cm}^3}{\mathrm{s}}\right) y_X^2 y_\Xi^2 \left(\frac{300\,\mathrm{GeV}}{m_\chi}\right)^2. \tag{IV.11}$$

Annihilation into pseudoscalars in this model could also be important, depending on the structure of the model. If this occurs, the annihilation into a with subsequent decays $a \to e^+e^-$ could provide a good fit to the data [67, 25]. However, in the present realization, annihilation into light pseudoscalars is suppressed by v^2 since Majorana fermions can only annihilate into CP-odd states.

A simple modification of the above Lagrangian would realize the heavy/light annihilation scenario of the previous section. For example, suppose S couples as $S\ell\bar{\Xi}$, and $\Xi\bar{\Xi}$ gets a mass from some other source. S no longer gets a vacuum expectaion value, but can still mediate the Dark Matter annihilation.

For light pseudoscalars, a new decay channel $\Xi^\pm \to a e^\pm$ opens, shown in Fig. 4.7. The pseudoscalar subsequently decays to electrons. The decays of Ξ^0 to pseudoscalars vanish in the limit of vanishing neutrino masses. The branching ratio for charged Ξ decays into

light pseudoscalars is given by:

$$BR(\Xi \to ae) = \frac{(1-\frac{m_a^2}{m_\Xi^2})^2}{(1-\frac{m_a^2}{m_\Xi^2})^2 + (\frac{g_2}{c_W})^2 \frac{1}{4y_\Xi^2}(1-\frac{m_Z^2}{m_\Xi^2})^2(2+\frac{m_\Xi^2}{m_Z^2})^2}. \tag{IV.12}$$

This branching fraction is small if $m_a \to m_\Xi$ or if $m_\Xi >> m_Z$. So for a low mass Ξ, the branching fraction to the pseudoscalar will dominate over that to Z bosons until $m_a \sim m_Z$. If this occurs, this will induce a slight modification of the results of the previous section. The net result of $\Xi^\pm \to ae$ dominating is a reduction in both the necessary boost factor and the antiproton contribution. Only the $\Xi^0 \to We$ decays contribute to the antiprotons in this case. This light pseudoscalar will have a very small coupling to electrons proportional to δ_e^2 and thus can easily evade detection at LEP.

4.5.2 A Supersymmetric Case

The supersymmetric generalization is straightforward. We will assume there is a dark matter sector containing the dark matter field X, where the fermionic component is the dark matter, that is coupled to the MSSM by a singlet S. This singlet then couples to a vectorlike heavy lepton. The superpotential is given by

$$W = W_{MSSM} + W_{DM} + W_\Xi, \tag{IV.13}$$

where the dark matter sector superpotential is

$$W_{DM} = y_X XXS + y_\Xi S\Xi\bar{\Xi}, . \tag{IV.14}$$

In this case, the dark matter annihilates via s-channel exchange of the the singlet field, S to a vectorlike lepton. Annihilation via t- and u-channel processes to the singlet S can also be important depending on the relatvie sizes of y_Ξ and y_X.

Should $\bar{\Xi}$ have the quantum numbers of a right-handed neutrinos, we have the mixing superpotential terms

$$W_\Xi = \tilde{y}\ell\bar{\Xi}H_u + \mu\Xi\bar{\Xi}. \tag{IV.15}$$

Then the $\bar{\Xi}$ marries mostly Ξ with a small amount of of the neutral component of the doublet ℓ. The Ξ will decay via mixing with the neutrinos, so possible decays are to the Z boson and a light neutrino or to a light lepton and a W boson. Decays of the Ξ into a light neutrino and a Z boson will produce the cosmic ray spectra of decays of Z bosons. Decays to leptons will produce a hard lepton and the cosmic ray spectra from W boson decays. Essentially identical remarks apply to the analogous superpotential where we give Ξ the quantum numbers of the right-handed electron.

We now focus on the case where the Ξ has the same quantum numbers as the left-handed lepton doublet, most similar to the case discussed in the previous section. After appropriate rotations, the leptonic portion of the superpotential can be brought to the form.

$$W_\Xi = y\ell e_R H_d + \tilde{y} e \Xi H_d + \mu \Xi \bar{\Xi}. \tag{IV.16}$$

This superpotential recovers the scenario of the previous section, assuming that the X particles are the dominant component of the dark matter, and possess a $\mathbb{Z}_2$ symmetry in addition to the usual R-parity of supersymmetric models. For the X fields to dominate the dark matter density, we will need to assume that the neutralino of the MSSM sector is a subdominant component. For example, this could be a light thermally produced wino.

Embedding in a supersymmetric model may lead to possible new signals at the LHC. The LHC will copiously produce particles with $\mathrm{SU}(3)_C$ quantum numbers, which will cascade down to the MSSM lightest supersymmetric particle. Should cascades contain a neutralino with a large bino component, this neutralino could decay to the heavy Ξ and its scalar superpartner $\tilde{\Xi}$. This decay must compete with other decays into light fermions, however, and is likely be phase space suppressed. Whether it is observable depends on the details of the spectrum. Due to the approximate $\mathbb{Z}_2$ symmetry, two Ξs must be produced at the end of any such cascade decay, which could give more lepton-rich signatures.

4.5.3 Realization in the NMSSM

Alternatively, for economy, one might try to embed the supersymmetric scenario in the NMSSM, adding only a pair of vectorlike leptons. The S field is already present to give the μ term, and the lilghtest supersymmetric particle can provide the Dark Matter. Then we have:

$$W_{NMSSM} = y\ell e_R H_d + \tilde{y} e_R \Xi H_d + y_\Xi S \Xi \bar{\Xi} + \kappa S^3 + \lambda S H_u H_d. \tag{IV.17}$$

In this case X is identified with a mixture of higgsino and singlino. For the dark matter annihilation to be primarily into heavy leptons and not into W bosons, the dark matter must have a large singlino component. Achieving a cross section large enough to explain PAMELA requires the lightest pseudoscalar Higgs boson to be primarily singlet [5].

[5] It should be noted that such a large cross section will necessitate some non-thermal mode of production of the dark matter to match the observed relic density.

CHAPTER V

A pulsar description of the WMAP Haze

Inherent in all indirect detection studies is a large uncertainty in the astrophysical backgrounds. The galaxy is a complicated place, so to convince ourselves that a cosmic ray anomaly is from dark matter requires a firm understanding of other astrophysical processes and their cosmic ray signals. Most dark matter models that explain the cosmic ray anomalies require a larger-than-thermal annihilation cross section. If the cross section is thermal and the cosmic ray anomalies are not dark matter, then we will need a detailed understanding of the backgrounds for future searches for dark matter.

One possible explanation of the WMAP Haze is in terms of annihilating dark matter [93]. The charged byproducts of the dark matter annihilations radiate synchrotron photons in the galactic magnetic field. A neutralino from supersymmetric theories annihilating to W^+W^- gives a good fit to the radial distribution of the spectrum for a dark matter halo profile scaling with a radial dependence which is slightly steeper than NFW [125] and a magnetic field in the few μG range. The cross-section of annihilating dark matter needed to produce the haze is consistent with what one would predict from the thermal freeze-out of the WIMP, namely $\sigma v \simeq 3 \times 10^{-26}$ cm^3/s. We urge caution, however, because recent work [72] has claimed that the significance of the WMAP haze may depend on the assumptions about the spatial variation of the synchrotron spectral index.

This signal may be even more interesting in light of the recent observations of an excess

of high energy cosmic ray positrons and electrons. The source of these positrons is unknown, however, there are several possibilities. Like the WMAP haze, they may be explained by annihilating DM (see *e.g.* [68, 66]). An explanation of the signal in terms of annihilating dark matter (DM), however, has multiple obstacles to overcome. First, it must annihilate with a cross-section significantly larger than that suggested by the thermal abundance, $\sigma v \simeq 3 \times 10^{-24-23}$ cm^3/s. Second, the DM candidate prefers leptophilic annihilation to avoid overproducing anti-protons [68, 82] and to produce a steep enough spectrum [66]. Gamma rays and radio measurements also generate significant constraints [68, 47], since the charged SM byproducts of the annihilation may emit either hard final state radiation or synchrotron emission in the galactic magnetic field. In short, if the positron excesses are to be explained in terms of annihilating Weakly Interacting Massive Particle, the WIMP must have non-standard properties. There are possible exceptions to these conclusions in the case that we happen to be nearby a dense clump of dark matter [126], or for non-standard propagation models [108].

Pulsars can also reproduce the PAMELA anomalies. If the rotation axis is perpendicular to our line of sight, we may not be able to observe the pulsar in gamma rays or radio waves. However, the electrons and positrons pair produced in the pulsar's magnetic field will still diffuse outward to our location. To produce a signal in the 100 GeV range, a single pulsar must be within a kiloparsec or so to give the steep rise seen by PAMELA or a combination of pulsars from farther away may conspire to produce the signal [28, 63, 221, 123, 218, 186, 157].

In this chapter we explore the possibility that the WMAP haze may also be generated by e^+e^- pair production in pulsars. Pulsars produce a significant flux of energetic electrons and positrons spread over the disk of the galaxy, which then emit synchrotron radiation as they traverse outward from the disk in the magnetic field of the galaxy. To explain the haze,

the expected signal from pulsars must both reproduce angular dependence of the signal from the galactic center, as well as the frequency dependence through the WMAP bands from 22 to 93 GHz. We show that an energy spectrum which is typical of that necessary for explaining the PAMELA data with pulsars also naturally produces the average variation of WMAP haze with latitude given typical galactic magnetic fields and diffusion parameters. We also discuss reproducing the detailed morphology of the WMAP haze.

In the next section we describe the model for the electron distribution from mature galactic pulsars, and in the following section their propagation through the ISM and the haze calculation.

5.1 Injection spectrum of positrons from pulsars

The mechanism by which pulsars produce electrons and positrons and details about their energy distribution are not very well understood. However, the theoretical models reproduce important characteristics like the observed distribution of spins, ages, and photon fluxes from radio to gamma-rays (e.g., [222]). Here, we wish to demonstrate that with a plausible model for pulsar e^+e^- injection spectra (that is consistent with observations), one can reproduce the WMAP haze. We begin by reviewing the model we utilize for the pulsar e^+e^- injection spectrum.

We consider only pulsars older than 10^5 years as potential sources of the e^+e^- pairs that create the haze. This is based on the expectation that young pulsars are surrounded by a nebula created by the kinetic energy released from the supernova explosion (almost 10^{51} ergs) so that e^+e^- cannot escape from this nebula until the pulsar is sufficiently old. The nebulae have typical sizes in the parsec range, and since a typical pulsar kick at birth is around ~ 500 km/s, it would take the pulsar thousands of years to escape the nebula. In addition, the nebulae themselves thin out in tens of thousands of years. For the mature pulsars, we will assume that the nebulae surrounding pulsars do not play a dominant role

in shaping the energy spectrum and we neglect the contributions from pairs diffusing out of younger pulsar nebulae. The younger pulsars are fewer in number and could contribute significantly to the higher energy end of the e^+e^- spectrum. However, the bulk of the synchrotron radiation in the WMAP bands comes from e^+e^- with energies much less than 100 GeV, which justifies our focus on mature pulsars.

To demonstrate the feasibility of our assertion that pulsars could explain most of the visible WMAP haze, we follow the Cheng and Zhang 2001 model (CZ01 from here on) [221], which relies on the production of highly energetic radiation in the outer magnetosphere gap of a rapidly spinning pulsar [62, 64, 220]. In the CZ01 model, the mean energy of e^+e^- injected into the inter-stellar medium $\overline{E}$ is set by its period, P, which increases with time. For a rotating magnetic dipole (in vacuum) this spin-down is given by

$$P(t) = P_0 \left(1 + \Delta t/\tau_0\right)^{1/2} , \tag{V.1}$$

$$\tau_0 = 1.35 \times 10^4 \mathrm{yr} \left(\frac{P_0}{30\mathrm{ms}}\right)^2 \left(\frac{M}{1.4 M_\odot}\right) \left(\frac{R}{15\mathrm{km}}\right)^4 \left(\frac{B}{10^{12}\mathrm{G}}\right)^{-2} , \tag{V.2}$$

where Δt is time since birth of the pulsar, P_0 is the initial period, M is the mass of the pulsar, R its radius and B is the surface magnetic field. The energy injected into the pairs all comes from the spin-down and the surface magnetic field is assumed to be constant. In the CZ01 model,

$$\overline{E} \simeq 44\,\mathrm{GeV} \left(\frac{\mathrm{P}}{0.1\mathrm{s}}\right)^{-3.6} \left(\frac{\mathrm{B}}{10^{12}\mathrm{G}}\right)^{0.27} \tag{V.3}$$

where P is the period of the pulsar at the time of emission and one of the parameters of the CZ01 model, the fraction of pairs escaping from the light cylinder, is set to 0.01.

The CZ01 model converts a fraction of the available spin-down power for pulsar ages $> 10^5$ yr to pairs. To set the scale we note that in this model, for $P = 0.5$ s and $B = 10^{12}$ G, the differential e^+e^- emission rate is 10^{35}/GeV/s, with mean energy 1 GeV. Only the gamma-ray pulsars are assumed to produce e^+e^- pairs in this model and this introduces

a B dependent upper-limit on the period ($P < 0.25(B/10^{12}\mathrm{G})^{6/13}\mathrm{s}$).

To predict the properties of the pulsar today, we need the initial period and magnetic field, and also the initial kick that the nascent neutron star received when the supernova occurred. The CZ01 study includes a Monte Carlo of these and other parameters that result in present day distributions that are broadly consistent with observations. We note that in the CZ01 model the spatial distribution of the injected e^+e^- will depend somewhat on the energy range of interest if pulsars older than about million years contribute significantly to that energy range. To test this, we repeat the modeling of CZ01, including a description of motion of pulsars in the galactic potential, and compute the final spatial and energy distribution of positrons. Our result for the energy distribution of the positrons agrees with CZ01. In addition, we find that the mean age of the pulsars, weighted by the positron ejection rate, is of order 10^5 years for the energy range of interest. Given the birth velocities, these ages imply that typical pulsars (contributing significantly to the positron flux) have only traveled ~ 100 parsecs from their birth place. We thus use the simple approximation that the spatial distribution of these pulsars is the same as the initial pulsar distribution, which in turn tracks that of the young stars in the stellar disk. Specifically, we adopt [179, 210]

$$\begin{aligned} \rho(\vec{x}) &= N^{-1} e^{-r/r_0 - |z|/z_0}, \quad \text{where} \\ N &= 4\pi z_0 r_0^2 (1 - e^{-r_{disk}/r_0}(1 + r_{disk}/r_0)) \,, \end{aligned} \tag{V.4}$$

where $r_{disk} = 15$ kpc, $r_0 = 4$ kpc and $z_0 = 100$ pc.

The distribution of pulsars close to the center is not well constrained – consequently the value of $r_0 = 4$ kpc that we use should be taken as a very rough estimate. We have chosen this value based on the dynamical models of the thin disk, which assign values for r_0 in the range of 2 to 4 kpc. We have adopted 4 kpc for our fiducial model and later explore the effect on the morphology of making r_0 smaller. In detail, we expect the pulsar

distribution to track the galactic star formation rate in the disk (rather than the thin disk density), but the observational constraints on the star formation in the disk [52] in the inner couple of kpc are weak. One may consider using the observed distribution of pulsars to reconstruct the true pulsar distribution in the galaxy after correcting for incompleteness. The distances to these pulsars are estimated through the dispersion measure, and this depends sensitively on the assumed distribution of electrons. The uncertainties inherent in this procedure makes it hard to pin down the distribution of pulsars in the inner galactic region [152]. We note that most of the pulsars in the distribution assumed in Eq. V.4 are at $r \sim r_0$. This is consistent with one of the two models advocated to explain the observed pulsar distribution in the Parkes multibeam pulsar survey [152]. We do not consider a secondary source of pairs from the pulsars in the bulge given that the bulge is thought to be old and have a low star formation rate (compared to the disk).

The CZ01 Monte Carlo predicts that the energy spectrum of the e^+e^- pairs should be $E^{-1.6}$ above about a GeV up to tens of GeV. The spectrum drops sharply above $E_{\rm cut} \sim 100$ GeV. Both these features (the slope and cut-off energy) are model dependent and we discuss the effect of changing these later on. To keep the discussion more general, we therefore adopt an energy spectrum (number of e^+e^- pairs per unit time per unit energy) given by

$$Q(E) = \dot{N}_{100} Q_0 f_e \left(\frac{E}{\rm GeV}\right)^{-\alpha} e^{-E/E_{\rm cut}} , \tag{V.5}$$

where our baseline model has $\alpha = 1.6$ and $E_{\rm cut} = 100$ GeV, and we allow it to vary later to see how it changes our results. We have separated out a factor f_e, which is the efficiency of converting the spin-down power of the pulsar into e^+e^- pairs (after an age of 10^5 yr), and the factor $\dot{N}_{100}$, which is the number of pulsars created every century.

The normalization Q_0 is fixed by the spin down power of all the pulsars, that is $W_0 = N_p \langle I\Omega^2 \dot{P}/P \rangle$ where N_p is the total number of pulsars and the brackets indicate averaging over the galactic population. We set $N_p = 0.01\dot{N}_{100}(T/{\rm yr} - 10^5) \simeq 1000\dot{N}_{100}T/10^5{\rm yr}$,

where T is the typical age of the pulsar contributing the e^+e^- pairs. The normalization condition for Q_0 is given by

$$\int \dot{N}_{100} Q_0 E^{-\alpha} e^{-E/E_{\rm cut}} E dE \;=\;$$

$$W_0 \;=\; N_p \times 6 \times 10^{38} \frac{\rm GeV}{\rm s} \langle \left(\frac{P}{0.1{\rm s}}\right)^{-4} \left(\frac{B}{10^{12}{\rm G}}\right)^2 \rangle \,, \tag{V.6}$$

$$\Rightarrow Q_0 \;\approx\; 5 \times 10^{40} {\rm GeV}^{-1} {\rm s}^{-1} \frac{100^{\alpha-1.6}\Gamma(0.4)}{\Gamma(2-\alpha)} \left(\frac{100{\rm GeV}}{E_{\rm cut}}\right)^{2-\alpha} \,, \tag{V.7}$$

where E is the electron or positron energy in GeV, and we have assumed median values for the pulsar mass of $1.4 M_\odot$, radius of 15 km, initial period of 20 ms, and surface magnetic field of 2×10^{12}G. For these values, Eq. V.2 shows that $T \gg \tau_0$ and therefore $\dot{P}/P = 1/2T$ for these mature pulsars. This simple estimate for Q_0 agrees with the Monte Carlo results of CZ01, who find $Q(E) = 1.7 \times 10^{39} E^{-1.6} \exp(-E/80)/{\rm GeV/s}$, if we assume $f_e \simeq 0.03$, $\dot{N}_{100} = 1$, $E_{\rm cut} = 80$GeV.

It is important to note that f_e is the fraction of spin down *power* that is injected into pairs *after* the assumed maturity age of 10^5 yr. This efficiency f_e is expected to be large since e^+e^- are the lightest electromagnetically coupled fermions. The fraction of total initial energy injected into the ISM in pairs is very small, $\sim f_e \tau_0/T$. This argument shows that if a significant amount of the spin-down energy released before the assumed maturity age of 10^5yr were to be available in the form of e^+e^- pairs injected into the ISM, then the required efficiency would be very small. We see this by noting that in the approximation that some fraction of all of the spin-down energy is injected into the ISM instantaneously in the form of e^+e^- with spectrum $E^{-1.6}$ and cut-off 100 GeV, we have $W_0 = \dot{N}_{100}(1/2) I \Omega_0^2/100{\rm yr}$, which works out to $Q_0 = 2 \times 10^{41}$ GeV^{-1} s^{-1} if we take (conservatively) $(1/2) I \Omega_0^2 = 10^{52}$GeV. The efficiency required then to get the same normalization as the CZ01 model is a factor of 4 less.

The origin of the $E^{-1.6}$ spectrum in the CZ01 model are the scalings of $\overline{E}$ and the spin

down power with period P. We note that $dn/dE \propto T/P^4/E^2 \propto 1/P^2/E^2$ where we have used the fact that the number of pulsars is proportional to the age and we have used the approximation $P^2 \propto T$. We include the $\overline{E}$ dependence on P to obtain $dn/dE \propto E^{2/3.6-2} \propto E^{-1.4}$, somewhat different from the $E^{-1.6}$ scaling because of the approximations we have made.

The cut-off in the spectrum around 100 GeV is related to our assumption that the pulsars have to be approximately 100 kyr or older to contribute significantly to the haze, and that the mean energy of pairs injected into the ISM depends on the pulsar period in the CZ01 model (see Eq. V.3). This estimate of the cut-off is uncertain both because of our blanket assumption that pulsars younger than 100 kyr do not contribute pairs, and also because in framing the arguments above we have assumed all pulsars are born with spin period of 30 ms. We certainly expect scatter about both these parameters. Including such scatter will change the details of the cut-off significantly but not the main result of the paper. In addition, a small change in the strong dependence of the mean energy on the period would affect the cut-off significantly. This steep dependence arises from processes that accelerate the pairs into the ISM and these processes are not well-understood. We note that the energy spectrum at lower energies ($\sim$ 10GeV) is much less sensitive to the above uncertainties.

At even lower energies, $E < 1$ GeV, pair emission luminosity is influenced by the modeling of a gamma-ray pulsar. This requirement, discussed above, imposes a magnetic field dependent upper limit on the period, which translates to a cut-off in the luminosity at low energies. These model assumptions therefore introduce uncertainties in the GeV range pair emission luminosity, which must be kept in mind when comparing to experiments like HEAT.

The estimates in this section assuming a vacuum dipole rotator model for the mature

pulsars have provided us with the basic features of the positron injection spectrum. We find that the spatial distribution should track that of the young stars in the disk, with an energy spectrum that is less steep than E^{-2} – specifically $E^{-1.6}$ for the model of CZ01 – and a total normalization that requires about 10% of the spin-down power of $\mathcal{O}(10^5\text{yr})$ pulsars to be injected into positrons.

5.2 Pulsars as a Source for the Haze

The positrons pumped into the ISM will lose energy and diffuse outwards, and as they do so, they will produce the synchrotron background. To model this we use the standard diffusion equation that describes the propagation and energy loss for a charged particle:

$$\frac{\partial}{\partial t}\frac{dn}{dE_e}(\vec{x},t,E) = K(E)\nabla^2\frac{dn}{dE_e} + \frac{\partial}{\partial E}B(\vec{x},E)\frac{dn}{dE_e} + Q(\vec{x},t,E)\,, \tag{V.8}$$

where $Q(\vec{x},t,E)$ is the source function, i.e., rate of production of positrons per unit energy with energy E at time t and location $\vec{x}$. It is a sum over all the pulsars in the galaxy. We have assumed that the diffusion coefficient $K(E)$ is spatially constant, as there is no evidence in the cosmic ray or diffuse galactic gamma-ray data to the contrary. In addition, we note that very little is known about the diffusion constant at the center of the galaxy. We will discuss the effect of changing the diffusion constant on the morphology of the haze later.

The synchrotron emission from the positrons along the line of sight receives contributions from a large number of pulsars. Since pulsars are being created on time scales of 100 years in the galaxy and this is much shorter than the diffusion time scale and the assumed 10^5 yr time lag, we expect a steady state calculation to work well. In the limit that the diffusion equation can be solved in a steady state, the source function reduces to

$$Q(\vec{x},E) = \rho(\vec{x})Q(E), \tag{V.9}$$

with $Q(E)$ given by Eq. V.5 and $\rho(\vec{x})$ given by Eq. V.4. This gives us explicitly

$$\begin{aligned} Q(E,\vec{x}) &= 1.5\times10^{-26}\left(\frac{\dot{N}_{100}}{1\text{ century}^{-1}}\right)\left(\frac{f_e}{0.15}\right)\left(\frac{100\text{ GeV}}{E_{\rm cut}}\right)^{2-\alpha} \\ &\times(\Gamma(0.4)/\Gamma(2-\alpha))\,100^{\alpha-1.6}\,(E/\text{GeV})^{-\alpha}\,e^{-E/E_{cut}} \\ &\times e^{-r/(4\text{ kpc})-|z|/(0.1\text{ kpc})}\text{ GeV}^{-1}\text{ s}^{-1}\text{ cm}^{-3}, \end{aligned} \tag{V.10}$$

for our fiducial r_0, z_0 and $r_{\rm disk}$ values.

We use GALPROP [205, 167] to compute the diffusion, and check the results with an ordinary partial differential equation solver. The diffusion coefficient is

$$K(E) = K_0\left(\frac{E}{3\text{ GeV}}\right)^{\delta}, \tag{V.11}$$

where we take $K_0 = 5\times10^{28}$ cm^2/s and the index $\delta = 0.33$ as our fiducial model parameters. We use the diffusive reacceleration scheme in Galprop with Alfvén speed of 36 km/s. These diffusion coefficient values are consistent with those used in the literature to fit cosmic ray data [189]. The energy loss coefficient $B(E,\vec{x})$ is calculated in GALPROP. It is dominated by inverse Compton scattering and synchrotron radiation for electrons and positrons in the energy range of interest. The energy loss due to inverse Compton scattering is calculated using the Klein-Nishina cross section with an interstellar radiation field that comes with the GALPROP package, discussed in [183, 208].

Energy loss due to synchrotron radiation is calculated using an exponential form of the galactic magnetic field,

$$B(r,z) = B_0 f_C(R) + (1-f_C(R))B_\odot e^{-(r-r_\odot)/r_b-|z|/z_b}, \tag{V.12}$$

where $R^2 = r^2+z^2$, B_0 is the magnetic field at the center of the galaxy and $B_\odot = 5\mu$G is the local magnetic field. We choose a characteristic scale $r_b = 10$ kpc and $z_b = 2$ kpc to be consistent with earlier studies aiming to explain the Haslam data and cosmic ray data [208, 54]. The value B_0 and the function $f_C(R)$ encode our ignorance about

the magnetic field at the center of the galaxy. Neither the detailed structure nor the value of the magnetic field in the inner galactic region is well known [115]. We choose $B_0 = 30\,\mu$G as our fiducial value although smaller and larger values also lead to consistent fits to the haze spectrum and its variation with latitude. Since there is no observational guidance on the specific structure of magnetic field within a couple of kpc from the galactic center, we adopt an exponential form, $f_C(R) = \exp(-R/R_C)$ and set $R_C = 1$ kpc. We note that this form for $f_C(R)$ achieves the aim of smoothly transitioning from a spherical magnetic field profile in the inner galactic region to the cylindrical B field profile that are commonly used to fit Haslam data, cosmic ray data and diffuse galactic gamma-ray background [208]. Our adopted magnetic field towards the center of the galaxy is consistent with the average magnetic field deduced on scales of order a kpc about the galactic center from observations of non-thermal radio filaments [145]. The parameters B_0 and $f_C(R)$ will control the morphology of the haze.

We also note that the 408 MHz Haslam maps do not directly constrain the inner galactic magnetic field strengths or structure since the synchrotron signal depends on $n_e B_\perp^{1.8}$ [54], where n_e is the number density of electrons contributing to the 408 MHz signal and $B_\perp$ is the component of the magnetic field perpendicular to the line-of-sight. The pulsars do not contribute significantly to the Haslam map. There must be a different source of e^+e^- with energies at or below GeV that contribute dominantly to the Haslam map. Thus, for an assumed magnetic field spatial distribution, the Haslam maps determine the spatial distribution of these lower energy electrons. It is clear from the Haslam maps that these lower energy electrons must be distributed more diffusely than the pulsar distribution assumed here. More detailed work on this subject would require a computation of the secondary positrons along with primary e^+e^- produced by supernova remnants, away from the galactic disk. The secondary positrons, which are sub-dominant at multi-GeV energies

in the solar neighborhood, will contribute significantly at $\sim$ GeV and lower energies because of their steeper spectrum [209] and there are large uncertainties in these calculations [74].

Our assumptions about energy losses differ from earlier work exploring constraints with the haze [121]. We do not assume a spatially constant ratio of energy density of starlight to the magnetic field energy density to fit the haze data (as discussed also in Ref. [109]); we parametrize our ignorance of the magnetic field in the center of the galaxy directly. This allows us to make more direct contact with studies aiming to fit cosmic ray and diffuse photon backgrounds.

We plot in Fig. 5.1 the electron flux spectrum at various positions with respect to the galactic center. The diffusion softens the spectrum considerably, implying a larger flux in the lower frequency bands of the WMAP haze. The question is then whether the spectrum remains sufficiently hard to explain the WMAP haze in the all frequency bands, from 22 to 93 GHz. We examine this next.

After propagation, at any given point in space, the flux in synchrotron radiation (in erg/s/Hz) in the presence of the magnetic field is computed according to the relation [100]

$$\epsilon(\nu,\gamma) = \frac{4\pi\sqrt{3}e^2\nu_B}{c}x^2\left(K_{4/3}(x)K_{1/3}(x) - \frac{3}{5}x[K^2_{4/3}(x) - K^2_{1/3}(x)]\right) \tag{V.13}$$

with $x = \nu/(3\gamma^2\nu_B)$, $\nu_B = eB/(2\pi m_e)$, and $\gamma(E)$ the electron's boost.

The total flux (in kJy/sr) in a given frequency at a given angle from the galactic center is computed by folding the synchrotron power with the electron distribution at any given point. The flux is then obtained by integrating along the line of sight:

$$\Phi(\nu) = \frac{1}{4\pi}\int_0^{\ell_{\rm max}} d\ell \int_0^\infty dE\, \epsilon(\nu,\gamma(E))\frac{dn}{dE}(r(\ell),z(\ell)), \tag{V.14}$$

where $r(\ell) = |r_e - \ell\cos(\theta)|$ and $z = \ell\sin(\theta)$ if we restrict out attention to angles θ above and below the galactic center, the sun is positioned at $r = r_e = 8$kpc and $z = 0$, and $\ell_{\rm max}$ is set by the height of the diffusion zone. We now turn to presenting our results utilizing

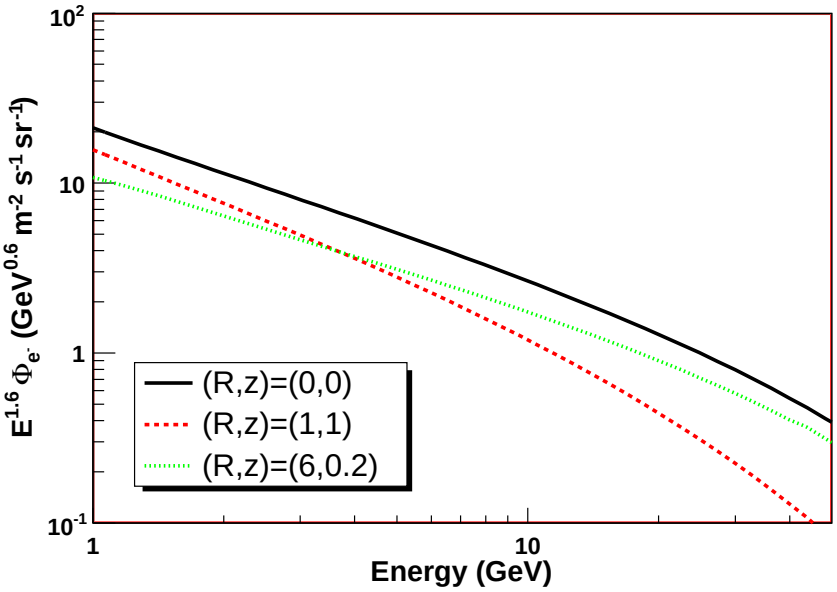

Figure 5.1: The curves show the e^+e^- energy spectrum at different locations in the galaxy that contribute significantly to the haze. We see that at energies below about 10 GeV, the shape of the spectrum depends on the location. For higher energies, the dominant contribution comes from more local pulsars. The energies around 10 GeV are particularly important for the haze and this figure shows that diffusion and energy-loss steepen the energy spectrum index to about -2. We urge caution when comparing these estimates to local e^+e^- measurements as discussed in the text below.

the formalism outlined above.

After propagation, we fit the haze using the flux from Eq. V.14 in the all WMAP bands. The overall normalization of the curve depends on both the magnetic field, B_0 in Eq. V.12, the average pulsar power W_0, and the average pulsar efficiency times pulsar production rate $f_e\dot{N}_{100}$. The range for $\dot{N}_{100}$ is 1-3 per century, following the rate of core collapse of supernovae in our galaxy. [190]. We have taken $\dot{N}_{100} = 2.8$, following [91]. In addition, owing to uncertainties in the subtraction, we also allow a constant background at all angles to be added in the fit.

The index α in Eq. V.5 and $E_{\rm cut}$ are important in fitting the frequency structure of the Haze observed by WMAP. The cutoff energy $E_{\rm cut}$ is required to be above a minimum value $\gtrsim 40$ GeV such that there will be enough radiation into the 93 GHz band, however cutoff energies larger than that will only serve to increase the required average efficiency per pulsar to reproduce the haze. Additionally, a soft spectrum, corresponding to a large α, will not give rise to a large enough amplitude in the high frequency bands to reproduce the haze. Lastly, the fit in the angular direction results by allowing the characteristic distance over which the magnetic field is damped from the galactic center, z_b in Eq. V.12, to vary.

As shown in Fig. 5.2, we find that with reasonable choices of these parameters, a galactic source of pulsars can explain both the amplitude and frequency dependence of the WMAP haze. The plotted synchrotron fluxes are averages over 20 degrees in longitude for below the galactic plane. We find that $z_b = 2$ kpc gives a good fit to the angular distribution. In detail, the shape of the haze depends on both the distribution of the injected pairs as well as the magnetic field profile. Future Planck data might provide an avenue to constrain these distributions better.

The cutoff energy $E_{\rm cut} = 100$ GeV taken from the CZ01 model [221] also fits the frequency band requirements of the haze very well. We show in Fig. 5.3 the results for a

larger choice of $E_{\rm cut}$. Since the parameters W_0, f_e, and $\dot{N}_{100}$ are interchangeable, to get a reasonable efficiency the most likely course is to raise the average pulsar spin down power. In general, the efficiencies noted there can be substantially and easily lowered by taking the power per pulsar W_0 and the magnetic field at the galactic center B_0 to higher, but still reasonable, values. In short, pulsars are a plausible explanation of the haze.

We also note that the choices of parameters we have made are consistent with those utilized in [123, 186] as a means to explain the HEAT, AMS, PAMELA, ATIC and PPB-BETs cosmic ray positron excesses with a single pulsar, or collection of local pulsars, suggesting that cosmic ray anomalies and WMAP haze may naturally have the same source.

We urge caution here that using the local measurements, say from HEAT and PAMELA, to normalize the pulsar synchrotron contribution requires many assumptions.

- Normalizing the distribution of the pulsars to the local density of pulsars and then using an analytic form to extrapolate to the center is not well motivated given the uncertainties in the the deduced pulsar distribution closer to the galactic center.

- For local measurements at energies 5 GeV and higher, the dominant contribution to the flux should come from a few local sources and we cannot use a smooth source spatial distribution to describe this (given the large expected variance).

- In the outer gap model for pulsars we use, the energy spectrum around a GeV and lower is very uncertain because of the cut-off, as discussed earlier. This is not a complicating factor for the haze because most of the contribution comes from approximately 5 GeV and higher, but it is an issue that must be addressed if one is normalizing to lower energy data. In addition, the low energy data is also affected by solar modulation.

- In order to link the haze to local measurements, we need a better understanding of

how the e^+e^- flux is affected by changes in diffusion between the local and central parts of the galaxy.

5.2.1 Morphology

The pulsar contribution to the haze is non-spherical, with the deviation from sphericity determined by a combination of factors including the diffusion coefficient, the structure of the magnetic field, and the spatial distribution of the pulsars. Here we vary each of the these within reasonable range to see their effect on the morphology of the predicted synchrotron signal. In each case, the frequency spectrum as well as the detailed drop in average power as a function of latitude are still good fits to the data. In the top left panel of Fig. 5.4 we show the synchrotron signal at 22 GHz in galactic coordinates for our fiducial parameters. The signal is distinctly elliptical, but judging whether these parameters are disfavored would require an analysis including the noise properties of the haze map. In the plot to its right, we show the signal when the diffusion coefficient is increased by a factor of 2. This is a modest increase for which we do not have strong observational constraints on the diffusion coefficient towards the center of the galaxy. Clearly, the contours look much more spherical. The largest deviations from sphericity occur close to the disk where the reconstruction of the haze has the largest uncertainties. In the bottom left plot we show the signal when r_0 (which governs the radial distribution of the pulsars) is smaller than the fiducial value and equal to 3 kpc.

As mentioned earlier in this section, the population of e^+e^- contributing to the Haslam map is different from the harder pulsar contribution. Further, as we have seen, factors of two change in the diffusion constant have a significant effect on the shape of the synchrotron signal. Thus the behavior of the diffusion constant in the central parts of the galaxy from energies 1 –10 GeV is important in comparing the Haslam and the haze maps. At this level, it is not clear that diffusion along the disk is the same as perpendicular to the disk.

This will affect the shape of the signal contours. Lastly, we note that removing the usual (softer) synchrotron component should also remove some of the more extended features in the predicted haze maps.

It is clear that the morphology depends significantly on parameters that cannot yet be determined from observations. However, this also opens up the possibility of constraining these parameters and perhaps the contribution of the pulsars to the haze with Fermi and Planck data. Note that the ellipticity in the maps trace back both to the distribution of the pulsars and the cylindrical structure of the magnetic field. A more detailed comparison to the data would have to account for the spiral arms and how the galactic magnetic field is observed to trace the spiral structure. Note that even a perfectly spherical source would result in an elliptical haze profile due to the magnetic field. This is shown in the final plot (bottom right) of Fig. 5.4 where we show the signal resulting from dark matter annihilations in a halo with inner density profile scaling as $r^{-1.2}$. For this plot, we have we have set $f_C(R) = 0$, so that the influence of the cylindrical magnetic field structure is clear – it makes the contours elliptical. Conversely, we have shown that the haze morphology depends sensitively on the assumed diffusion parameters and the magnetic field in the inner kpc, such that even if the source of e^+e^- is confined to the disk, the resulting haze can look approximately spherical. While the magnetic field, pulsar distribution, and electrons and positrons after propagation all are expected to trace the galactic disk, small deviations toward a more spherical form can conspire to produce the haze.

If the Fermi haze is a real excess and is from the same population of electrons as the WMAP haze, then the B-field cannot account for a spherical morphology for a pulsar description of the WMAP haze. In this case anisotropies in the diffusion coefficient would be a leading explanation for a pulsar description of the WMAP haze and Fermi haze.

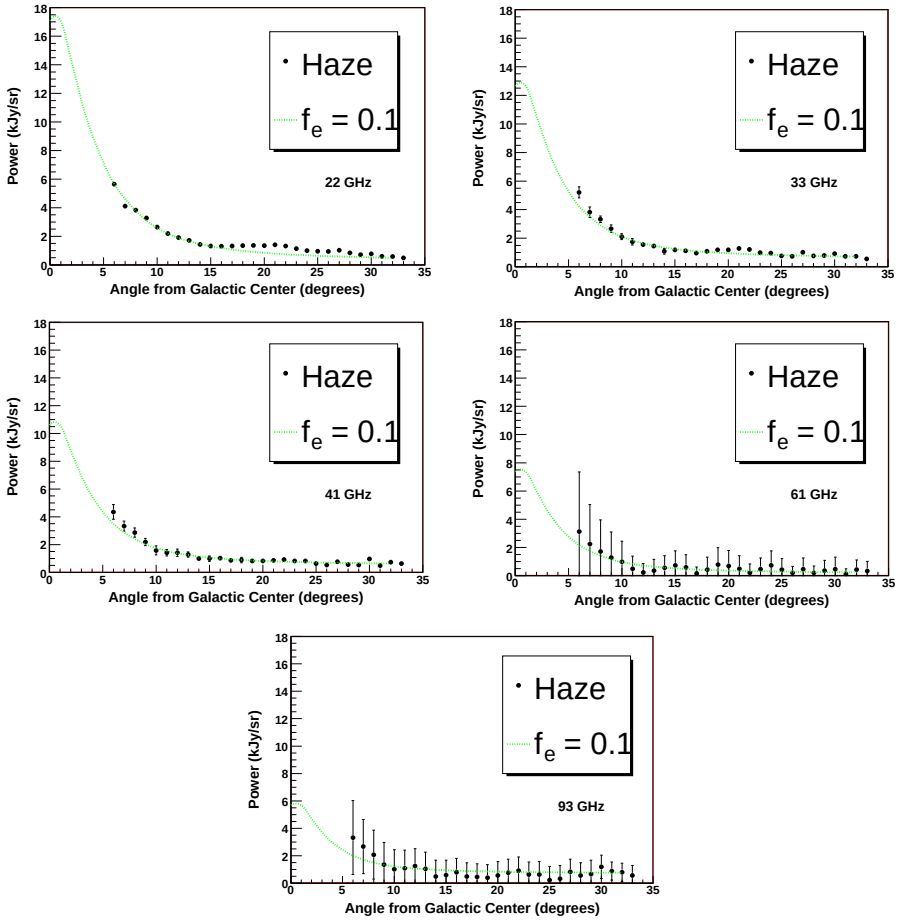

Figure 5.2: WMAP Haze for pulsar injection parameters $\alpha = 1.6$ and $E_{cut} = 100$ GeV and efficiency $f_e = 10\%$ (see eqs. (II.3, V.7) for a definition of efficiency). This efficiency is defined as the fraction of the spin-down power converted to e^+e^- pairs after an assumed maturity age of 10^5yr. The fraction of the total initial pulsar energy required in the form of e^+e^- pairs to explain the haze is 3%. The fits to the data above include a floating constant offset for each channel and the resulting χ^2 per dof is 1.1 within the inner 15^o and 2.1 within the inner 20^o.

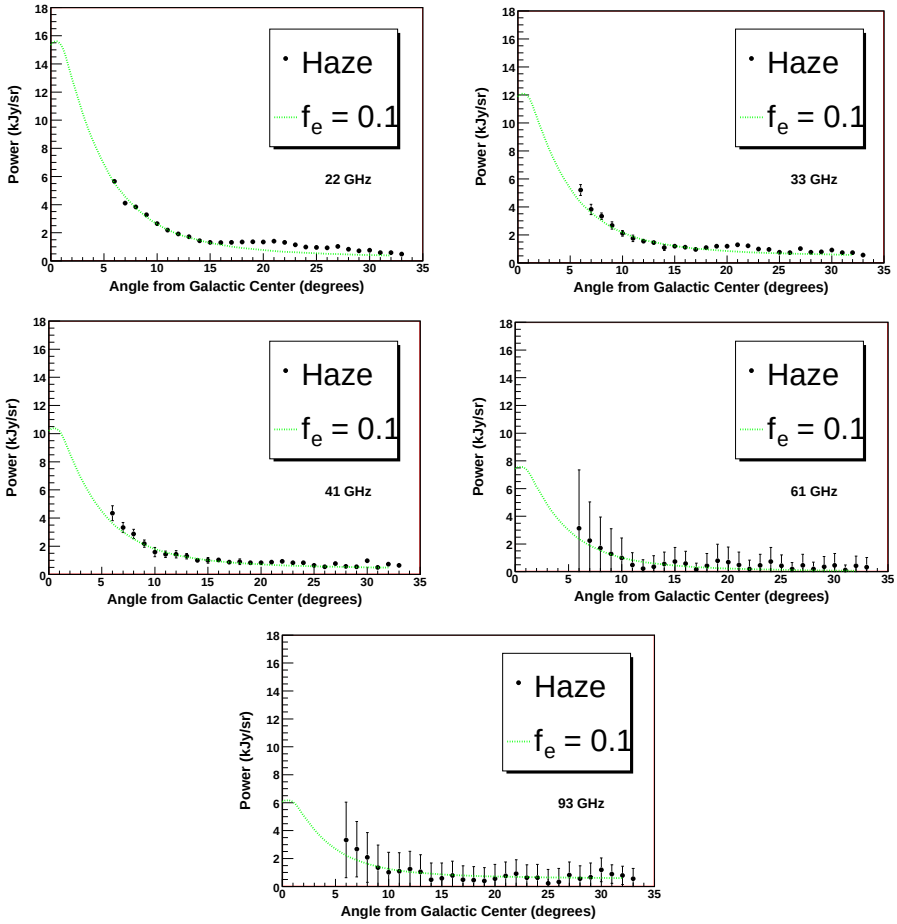

Figure 5.3: WMAP Haze for pulsar injection parameters $\alpha = 1.6$ and $E_{cut} = 500$ GeV and efficiency $f_e = 10\%$ (see eqs. (II.3, V.7) for a definition of efficiency). The larger energy cutoff results in a marginally better fit in the higher frequency bands. The fraction of the total initial pulsar energy required in the form of e^+e^- pairs to explain the haze 3%. The fits to the data above include a floating constant offset for each channel and the resulting χ^2 per dof is 0.9 within the inner 15^o and 2.3 within the inner 20^o.

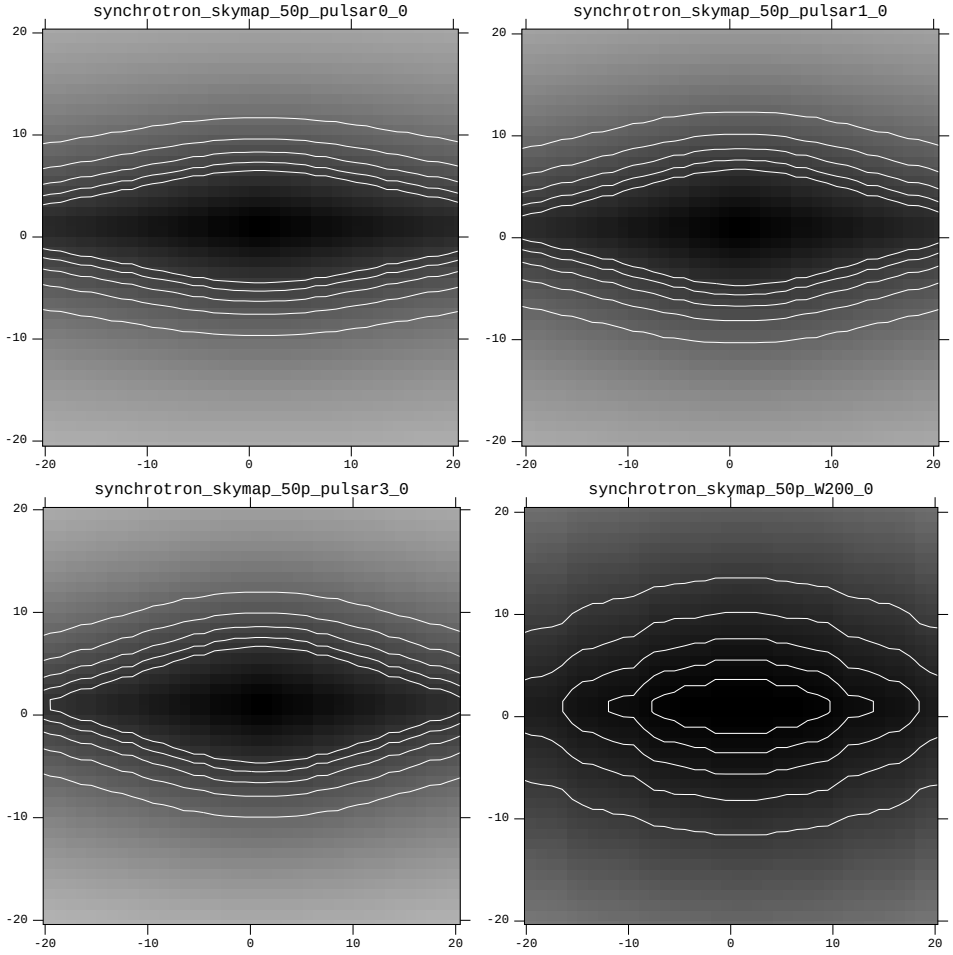

Figure 5.4: 22 GHz skymaps in galactic coordinates of the synchrotron signal predicted for different models. The contours are spaced equally between flux values of 2 and 6 kJy/sr. Note that galactic latitudes within roughly 5 degrees of the center are masked while estimating the haze contribution. The left plot in the top panel is the model with our fiducial parameters. The plot on the right in the top panel utilizes $K_0 = 1 \times 10^{29}$ cm^2/s (twice the fiducial value) as does the plot on the bottom left. The bottom left plot also modifies the source scale radius parameters to $R_0 = 3$ kpc. The plot on the right in the bottom panel is the signal from a model where dark matter is annihilating into e^+e^- pairs in the galaxy assumed to have a spherically symmetric dark matter density profile $\propto r^{-1.2}$ in the inner parts. We have set $f_C(R) = 0$ for the dark matter plot (see eq. (V.12)) so that the effect of the cylindrical galactic magnetic field profile on the signal is clear – the contours are elliptical.

CHAPTER VI

Conclusions

Now is an exciting time in the search for dark matter. If indirect hints of dark matter are to be taken at face value, then there is some new dynamics happening in the dark sector that is responsible for the steep rise in the PAMELA positron fraction favoring electrons and positrons over hadrons. If the satellite data has an astrophysical origin, then the picture is still rosy because then direct searches for DM nuclear interactions through Z or Higgs bosons could detect dark matter in the next few years. Finally, as the LHC turns on there will be an active search for dark matter created in the laboratory, and there will be a chance to directly measure its couplings to other particles.

In this thesis we explored the implications of dark matter in the MSSM. Supersymmetry is a leading candidate for physics beyond the Standard Model. If dark matter is a neutralino and supersymmetry is realized at the TeV scale, the LHC, nuclear recoil, and cosmic ray experiments would rapidly converge to measure the dark matter properties.

A non-thermally produced wino is a well-motivated candidate for the dark matter observed in our universe. Although there are apparent conflicts with anti-protons and gamma-rays, given the astrophysical uncertainties it is likely premature to assume the wino interpretation is completely excluded. Its large annihilation cross section could potentially allow it to explain the suggestion of an excess from PAMELA with a non-standard propagation model. However, to avoid conflict with bounds from gamma rays (and perhaps synchrotron

radiation), the dark matter distribution cannot be too highly peaked towards the center. There is already some tension in the case of an NFW profile. This fact suggests that if the PAMELA excess in positrons comes from Wino dark matter, Fermi should follow with a confirmation.

Any candidate detection by PAMELA and Fermi will need to be examined in the context of direct detection experiments. Adding an admixture of Higgsino to the neutralino allows an increase in the direct detection cross section (via the $\tilde{w} - \tilde{h} - h$ coupling). An increased Higgsino content also increases the capture cross section on the sun, allowing for a possible indirect detection via neutrinos. Thus, signals in these types of experiments could help to probe the Higgsino content of the LSP.

At the LHC, a pure wino of a few hundred GeV by itself may be difficult to observe via direct production. However, it may be possible to find it in decays or associated production. The sensitivity of this modes depends on the mass of the lightest colored mode. In minimal models of anomaly mediation [191, 103], the ratio of the wino mass to the gluino mass is a factor of nine. So a 200 GeV wino implies a 1.8 TeV gluino, which might preclude an early discovery. However, if the mass difference is smaller, as occurs in some models of non-thermal production then it might be possible to determine the wino nature of the LSP by looking for charged tracks, as recently studied in [27]. More generally, several LHC signatures will depend on the mass and type of the LSP, so we expect that careful studies will be able to test whether a candidate seen in indirect data is also present in LHC data.

While the Wino could explain the Cosmic Ray anomalies, it would require a non-thermal production mechanism to explain the current amount of dark matter in the universe. If the dark matter is of thermal origin, we have argued that given the experimental constraints from LEP, neutralino DM is likely to be well-tempered with possible signals for the next generation of SI and SD DD experiments. In fact, any model (such as the singlet-doublet

model) which interacts with the SM via a light Higgs boson can imply a signal in SI experiments and any model of Majorana fermions with non-trivial couplings to the Z^0 can imply a signal in SD experiments. There are ways to avoid these arguments, but these options involve some new source of tuning, so we take them to be disfavored. With available methods we should be able to probe the majority of the natural range for the SI and SD DD signals of both thermal and non-thermal neutralino DM.

In this work we have explored the physics of SD DD with an emphasis on the correlations with SI experiments. In the process, we have determined some expectations for the SD cross sections. In particular, in the MSSM, $\left(\sigma_{\rm SD}^{\rm SUSY}\right) < 6 \times 10^{-3}\,{\rm pb}$ without making any assumptions about the thermal history. Again, allowing for a non-trivial cosmic history, but imposing the unified gaugino mass condition, we find $\left(\sigma_{\rm SD}^{\rm SUSY}\right) < 4 \times 10^{-3}\,{\rm pb}$. Finally, $\left(\sigma_{\rm SD}^{\rm SUSY}\right) < 2 \times 10^{-3}\,{\rm pb}$ when a thermal relic density is imposed. These represent important targets for future experiments. We note that if SD cross sections larger then $\sim 6 \times 10^{-3}\,{\rm pb}$ were observed, the DM would not be an MSSM neutralino. This would point to more exotic theories like the SDM or models with light mediators [57]. For models which reproduce the relic density, in the decoupling limit, and unified gaugino masses, a 1-ton COUPP-like experiment could probe the entire range of SD cross sections up to WIMP masses of $\mathcal{O}(1\,{\rm TeV})$.

The sharp rise in the PAMELA signal and the lack of an antiproton excess calls out for new thinking in terms of the dark matter annihilation processes. We have proposed a simple scenario which realizes the positron excess in PAMELA without exceeding the antiproton data. This required the introduction of a new heavy vectorlike lepton state that mixes with the lighter Standard Model leptons. We found that in addition to reproducing the PAMELA signal, this vectorlike lepton could be produced in Drell-Yan production at the LHC. Even if no missing energy signals are seen at the LHC, the observation of a

vectorlike lepton, when combined with astrophysical observations might still illuminate the dark matter sector.

Most dark matter modes that explain the cosmic ray anomalies require a larger than thermal cross section. Establishing the annihilation cross section is important information about the dark sector. This requires a thorough understanding of the astrophysical backgrounds of indirect detection. We have proposed a plausible astrophysical source for the WMAP haze. We have shown that e^+e^- pairs injected into the interstellar medium by the galactic pulsars may contribute significantly to the WMAP haze. The models of pair emission and galactic magnetic fields we investigated showed that pulsars could easily account for all of the haze and successfully reproduce both its angular and frequency distributions observed in the WMAP data. The parameters for the input e^+e^- spectrum, the magnetic field and inverse Compton energy losses that we employed to fit the haze towards the galactic center are also consistent with those that have recently been used to fit the cosmic ray positron excess from a local distribution of pulsars [123, 186]. These facts suggest that both the haze and the positron excesses may have the same underlying source. We also considered the morphology of the haze in detail and pointed out that in it may be possible to use the deviation from sphericity to bound the contribution of e^+e^- from galactic pulsars to the haze. This would be an important background to the dark matter contribution to the haze.

The possibility that the cosmic ray anomalies are due to annihilating dark matter is exciting and it behooves us to search for alternative astrophysical explanations. Correlating various signals of dark matter annihilation (positrons, anti-protons, anti-deuteron, gamma-rays, haze, etc) may enable progress in this direction.

There are three notable experiments that are taking data now or will be taking data soon which could clean up the cosmic ray dark matter story. The Fermi Gamma Ray

Telescope is looking for photons directly from dark matter annihilations. If a signal is found in an area free of backgrounds, such as a satellite galaxy, this would be proof of the WIMP hypothesis. It may also discover evidence of dark matter annihilation products in our own galaxy, such as the Fermi Haze. Modeling the gamma-ray backgrounds with a diffusion model would confirm if the Fermi Haze [79] is a real effect.

The Planck Satellite will more precisely measure the cosmic microwave background. This could help to nail down the spectrum of the WMAP haze in higher frequency bands. In addition, it could show evidence of DM annihilations at the time of recombination [201]. Although this could be mimicked by inflationary models with a running spectral index, it would also serve as evidence of a larger than thermal DM annihilation cross section.

Finally, the AMS experiment will put a detector on the International Space Station. This could confirm the PAMELA experiment, as well as gather better statistics on the electron, positron, anti-proton, and anti-deuteron spectra.

This is an exciting time for direct detection experiments as well. The CDMS II experiment [12] has provided two tantalizing events. XENON100 will determine if these are dark matter collisions in the coming months. For spin dependent scattering, in addition to IceCube with DeepCore[14], a new generation of terrestrial experiments such as COUPP and PICASSO will push the spin dependent cross section limits down by orders of magnitude in the near term.

While direct and indirect experiments may discover dark matter, the LHC startup will help to measure the DM properties. Precise measurements of the mass and couplings of the dark matter could determine if it is a thermal relic and if it is responsible for the cosmic ray signals. Confirming that missing energy signals are indeed the dark matter of our universe would be a triumph of the LHC.

APPENDICES

APPENDIX A

Squark Contributions to Direct Detection

The neutralino can scatter off of quarks via s-channel squark exchange, giving contributions to $\mathcal{O}_q^{\rm SI}$ or $\mathcal{O}_q^{\rm SD}$. Only squarks that couple to the light quarks (u, d, s) will be able to contribute to the SI and SD cross sections since only the light quarks have non-negligible nuclear matrix elements.

A non-zero "left-right" squark mixture is required since SI scattering converts a left-handed quark into a right-handed quark. Though a Bino/Wino mixture maximizes the coupling between the quarks and the neutralino, the scattering cross section for a pure Bino is of the same order.

If one makes the standard assumption that left-right squark mixing (*i.e.* a-terms) are proportional to yukawa couplings, then the squark mixing angle is proportional to $m_q/\tilde{m}_q$. Therefore, all SI couplings will be proportional to a quark mass and there is no enhancement for the light squarks over Higgs boson exchange. The maximum cross section is

$$\left(\sigma_{\rm SI}^{\rm squark}(\chi\, N \to \chi\, N)\right)_{\rm max} = 6 \times 10^{-9}\ {\rm pb} \left(\frac{200\ {\rm GeV}}{\tilde{m}_s}\right)^4, \tag{A.1}$$

for a Bino-Wino mix. This is subdominant to the Higgs boson exchange contribution barring the cancellations discussed in Sec. 3.5.4[1].

The maximum $\sigma_{\rm SD}(\chi\, p \to \chi\, p)$ contribution from squark exchange is for a "left-handed"

[1] If exceptionally large left-right in the squark sector is allowed (perhaps through abnormally large a-terms) a contribution to $\sigma_{\rm SI}(\chi\, N \to \chi\, N)$ of $\mathcal{O}(10^{-3}$ pb) may be obtained.

up-type squark coupling to a pure Wino, due to the larger $SU(2)$ gauge coupling:

$$\left(\sigma_{\rm SD}^{\rm squark}(\chi\, p \to \chi\, p)\right)_{\rm max} = 3 \times 10^{-4}\ {\rm pb} \left(\frac{200\ {\rm GeV}}{\tilde{m}_u}\right)^4 . \tag{A.2}$$

This is typically subdominant to the Z^0 contribution to SD DD. Thus, we will focus on the effects of Z^0 exchange in our discussions of the expected SD cross section.

APPENDIX B

The Bino/Higgsino and Wino/Higgsino Limits

In the limit of large M_1 (M_2) the neutralino is dominantly a Wino/Higgsino (Bino/Higgsino) admixture. We can explore this effective 3 state system using the SDM defined as (see Eq. (III.26) above):

$$\mathcal{L}_{\rm SDM} \ni \mu_D\, D\, \bar{D} + \lambda\, \boldsymbol{h}\, S\, D + \lambda'\, \boldsymbol{h}^*\, S\, \bar{D} + \frac{\mu_S}{2}\, S^2. \tag{B.1}$$

The resulting lightest eigenstate (χ) is specified by

$$\chi \equiv Z_S\, S + Z_D\, D + Z_{\bar{D}}\, \bar{D}. \tag{B.2}$$

Following [21], it is useful to write this system in a basis defined by S and $D_\pm \equiv \frac{1}{\sqrt{2}}\,(D \pm \bar{D})$. Note that the labels $\pm$ have nothing to do with electric charge. The mass matrix is then, in the (S, D_+, D_-) basis,

$$\mathcal{M}_{\rm SDM} = \begin{pmatrix} \mu_S & \frac{1}{\sqrt{2}}\,(\lambda+\lambda')\,v & \frac{1}{\sqrt{2}}\,(\lambda-\lambda')\,v \\ \frac{1}{\sqrt{2}}\,(\lambda+\lambda')\,v & \mu_D & 0 \\ \frac{1}{\sqrt{2}}\,(\lambda-\lambda')\,v & 0 & -\mu_D \end{pmatrix},$$

with the resulting lightest eigenstate,

$$\chi \equiv Z_S\, S + Z_{D_+}\, D_+ + Z_{D_-}\, D_-. \tag{B.3}$$

Since we are interested in the SD DD cross section, our goal is to extract the coupling

of χ to the Z^0. The coefficient of the operator $\mathcal{O}_q^{\rm SD}$ of Eq. (III.10) is given by

$$d_q = -\frac{g^2}{4\,m_Z^2\,c_w^2}\,|2\,Z_{D_+}\,Z_{D_-}|^2\,T_3^q. \tag{B.4}$$

Note that $|2\,Z_{D_+}\,Z_{D_-}| \equiv |Z_D|^2 - |Z_{\bar{D}}|^2$. One can find analytic expressions for the mass eigenstates and the combination $|2\,Z_{D_+}\,Z_{D_-}|$ in various useful limits. To second order in v, for $|\mu_D|$, $|\mu_S|$, $(|\mu_D| - |\mu_S|) \gg \lambda\,v$, $\lambda'\,v$

$$m_\chi = \mu_S - \frac{2\,\lambda\,\lambda'\,v^2}{\mu_D} - \frac{(\lambda^2+\lambda'^2)\,v^2\,\mu_S}{\mu_D^2} \tag{B.5}$$

$$|2\,Z_{D_+}\,Z_{D_-}| = \frac{(\lambda'^2-\lambda^2)\,v^2}{\mu_D^2-\mu_S^2}, \tag{B.6}$$

and for $|\mu_D| = |\mu_S| \gg \lambda\,v$, $\lambda'\,v$,

$$m_\chi = \mu_S - \frac{1}{\sqrt{2}}\,|\lambda+\lambda'|\,|v| + \frac{(\lambda-\lambda')^2\,v^2}{8\,\mu_S} \tag{B.7}$$

$$|2\,Z_{D_+}\,Z_{D_-}| = \frac{(\lambda'-\lambda)\,v}{2\,\sqrt{2}\,|\mu_S|} + \frac{(\lambda'^2-\lambda^2)\,v^2}{8\,\mu_S^2}. \tag{B.8}$$

Perturbing away from the limit of exact degeneracy gives corrections to these expressions of $\mathcal{O}((\mu_S - \mu_D)/\mu_D)$. Note we have assumed that there is no CP violation for simplicity. In order to apply these expressions to the MSSM one can make the identifications

SDM	Bino/Higgsino	Wino/Higgsino
μ_S	M_1	M_2
μ_D	μ	μ
$\lambda\,v$	$-m_Z\,s_w\,c_\beta$	$m_Z\,c_w\,c_\beta$
$\lambda'\,v$	$-m_Z\,s_w\,s_\beta$	$m_Z\,c_w\,s_\beta$

where we neglect terms of $\mathcal{O}(1/M_2)$ for the Bino/Higgsino system and $\mathcal{O}(1/M_1)$ for the Wino/Higgsino system.

Explicitly making the substitutions for the MSSM we have

$$(\text{B.9}) \quad |Z_{H_d}|^2 - |Z_{H_u}|^2 = \begin{cases} \frac{c_{2\beta}\, s_w^2\, m_Z^2}{\mu^2 - M_1^2} \\ \qquad \text{for } |M_1|,\, |\mu|,\, |\mu| - |M_1| > m_Z,\, M_2 \to \infty \\ \frac{c_{2\beta}\, c_w^2\, m_Z^2}{\mu^2 - M_2^2} \\ \qquad \text{for } |M_2|,\, |\mu|,\, |\mu| - |M_2| > m_Z,\, M_1 \to \infty, \end{cases}$$

and

$$(\text{B.10}) \qquad |Z_{H_d}|^2 - |Z_{H_u}|^2 = \begin{cases} \frac{(s_\beta - c_\beta)\, s_w\, m_Z}{2\sqrt{2}\,|\mu|} + \frac{(s_\beta^2 - c_\beta^2)\, s_w^2\, m_Z^2}{8\,\mu^2} \\ \qquad \text{for } |M_1| = |\mu| > m_Z,\, M_2 \to \infty \\ \frac{(s_\beta - c_\beta)\, c_w\, m_Z}{2\sqrt{2}\,|\mu|} + \frac{(s_\beta^2 - c_\beta^2)\, c_w^2\, m_Z^2}{8\,\mu^2} \\ \qquad \text{for } |M_2| = |\mu| > m_Z,\, M_1 \to \infty. \end{cases}$$

APPENDIX C

No-go Theorem for photino-Higgsino Dark Matter

The neutralino mass matrix in the $(\tilde{\gamma}, \tilde{Z}, \tilde{H}_d, \tilde{H}_u)$ basis is given by

$$\mathcal{M} = \begin{pmatrix} M_1\, c_w^2 + M_2\, s_w^2 & (M_1 - M_2)\, c_w\, s_w & -m_Z\, s_{2w}\, c_\beta & m_Z\, s_{2w}\, s_\beta \\ (M_1 - M_2)\, c_w\, s_w & M_1\, s_w^2 + M_2\, c_w^2 & m_Z\, c_{2w}\, c_\beta & -m_Z\, c_{2w}\, s_\beta \\ -m_Z\, s_{2w}\, c_\beta & m_Z\, c_{2w}\, c_\beta & 0 & -\mu \\ m_Z\, s_{2w}\, s_\beta & -m_Z\, c_{2w}\, s_\beta & -\mu & 0 \end{pmatrix}.$$

Is it possible to generate a large SD/SI ratio by having DM which is only a mixture of photino and Higgsino? The Higgsino component is required for a non-trivial coupling to the Z^0 and the an admixture of photino (and not Zino) will allow $(|Z_{H_d}|^2 - |Z_{H_u}|^2) \neq 0$ without introducing a coupling to the Higgs. We show that current phenomenological bound preclude this possibility.

There are two potential options. The first is decoupling the Zino by making it heavy while tuning the photino mass to be $\sim \mu$. This implies taking the limit where M_1 and M_2 are large while the combination $M_1\, c_w^2 + M_2\, s_w^2$ stays small, which requires $\mathrm{sgn}(M_1) \neq \mathrm{sgn}(M_2)$. Then the Zino-photino mixing will go like $(M_1 - M_2)/m_{\tilde{Z}} > \mathcal{O}(1)$. Note that we are free to take $M_1 < m_Z$ to suppress this mixing, but due to the LEP bound on the chargino mass, $M_2 > m_Z$. The second option is to try to eliminate the photino-Zino mixing by taking $M_1 = M_2$. Then the Zino and photino have the same mass and the Higgsino

will mix with both, resulting in a DM state which is an equal admixture of all 4 gauge eigenstates. Therefore, a neutralino cannot be a mixture of only photino and Higgsino.

BIBLIOGRAPHY

BIBLIOGRAPHY

[1] V. M. Abazov et al. Search for Long-Lived Charged Massive Particles with the D0 Detector. *Phys. Rev. Lett.*, 102:161802, 2009.

[2] R. Abbasi et al. Limits on a muon flux from neutralino annihilations in the Sun with the IceCube 22-string detector. *Phys. Rev. Lett.*, 102:201302, 2009.

[3] Aous A. Abdo et al. Measurement of the Cosmic Ray e+ plus e- spectrum from 20 GeV to 1 TeV with the Fermi Large Area Telescope. *Phys. Rev. Lett.*, 102:181101, 2009.

[4] K. Abe et al. Measurement of cosmic-ray low-energy antiproton spectrum with the first BESS-Polar Antarctic flight. *Phys. Lett.*, B670:103–108, 2008.

[5] Bobby Samir Acharya, Konstantin Bobkov, Gordon L. Kane, Jing Shao, and Piyush Kumar. The G_2-MSSM - An M Theory motivated model of Particle Physics. *Phys. Rev.*, D78:065038, 2008.

[6] Bobby Samir Acharya et al. Non-thermal Dark Matter and the Moduli Problem in String Frameworks. *JHEP*, 06:064, 2008.

[7] Bobby Samir Acharya, Gordon Kane, Scott Watson, and Piyush Kumar. A Non-thermal WIMP Miracle. *Phys. Rev.*, D80:083529, 2009.

[8] O. Adriani et al. A new measurement of the antiproton-to-proton flux ratio up to 100 GeV in the cosmic radiation. *Phys. Rev. Lett.*, 102:051101, 2009.

[9] Oscar Adriani et al. An anomalous positron abundance in cosmic rays with energies 1.5.100 GeV. *Nature*, 458:607–609, 2009.

[10] : M. Ageron. Performance of the First ANTARES Detector Line. 2008.

[11] M. Aguilar et al. Cosmic-ray positron fraction measurement from 1-GeV to 30- GeV with AMS-01. *Phys. Lett.*, B646:145–154, 2007.

[12] Z. Ahmed et al. Results from the Final Exposure of the CDMS II Experiment. 2009.

[13] Z. Ahmed et al. Search for Weakly Interacting Massive Particles with the First Five-Tower Data from the Cryogenic Dark Matter Search at the Soudan Underground Laboratory. *Phys. Rev. Lett.*, 102:011301, 2009.

[14] J. Ahrens et al. Sensitivity of the IceCube detector to astrophysical sources of high energy muon neutrinos. *Astropart. Phys.*, 20:507–532, 2004.

[15] Baris Altunkaynak, Michael Holmes, and Brent D. Nelson. Solving the LHC Inverse Problem with Dark Matter Observations. *JHEP*, 10:013, 2008.

[16] C. Amsler et al. Review of particle physics. *Phys. Lett.*, B667:1, 2008.

[17] J. Angle et al. First Results from the XENON10 Dark Matter Experiment at the Gran Sasso National Laboratory. *Phys. Rev. Lett.*, 100:021303, 2008.

[18] J. Angle et al. Limits on spin-dependent WIMP-nucleon cross-sections from the XENON10 experiment. *Phys. Rev. Lett.*, 101:091301, 2008.

[19] E. Aprile et al. New Measurement of the Relative Scintillation Efficiency of Xenon Nuclear Recoils Below 10 keV. *Phys. Rev.*, C79:045807, 2009.

[20] S. Archambault et al. Dark Matter Spin-Dependent Limits for WIMP Interactions on 19-F by PICASSO. *Phys. Lett.*, B682:185–192, 2009.

[21] N. Arkani-Hamed, A. Delgado, and G. F. Giudice. The well-tempered neutralino. *Nucl. Phys.*, B741:108–130, 2006.

[22] N. Arkani-Hamed, S. Dimopoulos, G. F. Giudice, and A. Romanino. Aspects of split supersymmetry. *Nucl. Phys.*, B709:3–46, 2005.

[23] Nima Arkani-Hamed and Savas Dimopoulos. Supersymmetric unification without low energy supersymmetry and signatures for fine-tuning at the LHC. *JHEP*, 06:073, 2005.

[24] Nima Arkani-Hamed, Savas Dimopoulos, and Shamit Kachru. Predictive landscapes and new physics at a TeV. 2005.

[25] Nima Arkani-Hamed, Douglas P. Finkbeiner, Tracy R. Slatyer, and Neal Weiner. A Theory of Dark Matter. *Phys. Rev.*, D79:015014, 2009.

[26] Asimina Arvanitaki et al. Astrophysical Probes of Unification. *Phys. Rev.*, D79:105022, 2009.

[27] Shoji Asai, Takeo Moroi, and T. T. Yanagida. Test of Anomaly Mediation at the LHC. *Phys. Lett.*, B664:185–189, 2008.

[28] A. M. Atoian, F. A. Aharonian, and H. J. Volk. Electrons and positrons in the galactic cosmic rays. *Phys. Rev.*, D52:3265–3275, 1995.

[29] Howard Baer, Azar Mustafayev, Eun-Kyung Park, and Xerxes Tata. Target dark matter detection rates in models with a well- tempered neutralino. *JCAP*, 0701:017, 2007.

[30] E. A. Baltz et al. Pre-launch estimates for GLAST sensitivity to Dark Matter annihilation signals. *JCAP*, 0807:013, 2008.

[31] Edward A. Baltz, Marco Battaglia, Michael Edward Peskin, and Tommer Wizansky. Determination of dark matter properties at high-energy colliders. *Phys. Rev.*, D74:103521, 2006.

[32] Edward A. Baltz and Joakim Edsjo. Positron Propagation and Fluxes from Neutralino Annihilation in the Halo. *Phys. Rev.*, D59:023511, 1998.

[33] Edward A. Baltz, Joakim Edsjo, Katherine Freese, and Paolo Gondolo. The cosmic ray positron excess and neutralino dark matter. *Phys. Rev.*, D65:063511, 2002.

[34] Edward A. Baltz, Joakim Edsjo, Katherine Freese, and Paolo Gondolo. The positron excess and supersymmetric dark matter. 2002.

[35] Riccardo Barbieri, M. Frigeni, and G. F. Giudice. DARK MATTER NEUTRALINOS IN SUPERGRAVITY THEORIES. *Nucl. Phys.*, B313:725, 1989.

[36] Vernon Barger, Wai-Yee Keung, and Gabe Shaughnessy. Spin Dependence of Dark Matter Scattering. *Phys. Rev.*, D78:056007, 2008.

[37] M. Barnabe-Heider et al. Improved Spin Dependent Limits from the PICASSO Dark Matter Search Experiment. *Phys. Lett.*, B624:186–194, 2005.

[38] S. W. Barwick et al. Cosmic ray positrons at high-energies: A New measurement. *Phys. Rev. Lett.*, 75:390–393, 1995.

[39] S. W. Barwick et al. Measurements of the cosmic-ray positron fraction from 1- GeV to 50-GeV. *Astrophys. J.*, 482:L191–L194, 1997.

[40] John F. Beacom, Nicole F. Bell, and Gregory D. Mack. General upper bound on the dark matter total annihilation cross section. *Phys. Rev. Lett.*, 99:231301, 2007.

[41] J. J. Beatty et al. New measurement of the cosmic-ray positron fraction from 5-GeV to 15-GeV. *Phys. Rev. Lett.*, 93:241102, 2004.

[42] E. Behnke et al. Improved Spin-Dependent WIMP Limits from a Bubble Chamber. *Science*, 319:933–936, 2008.

[43] G. Belanger, E. Nezri, and A. Pukhov. Discriminating dark matter candidates using direct detection. *Phys. Rev.*, D79:015008, 2009.

[44] U. Bellgardt et al. Search for the Decay mu+ → e+ e+ e-. *Nucl. Phys.*, B299:1, 1988.

[45] L. Bergstrom, J. Edsjo, Michael Gustafsson, and P. Salati. Is the dark matter interpretation of the EGRET gamma excess compatible with antiproton measurements? *JCAP*, 0605:006, 2006.

[46] Lars Bergstrom. Non-baryonic dark matter: Observational evidence and detection methods. *Rept. Prog. Phys.*, 63:793, 2000.

[47] Lars Bergstrom, Gianfranco Bertone, Torsten Bringmann, Joakim Edsjo, and Marco Taoso. Gamma-ray and Radio Constraints of High Positron Rate Dark Matter Models Annihilating into New Light Particles. *Phys. Rev.*, D79:081303, 2009.

[48] Lars Bergstrom, Piero Ullio, and James H. Buckley. Observability of gamma rays from dark matter neutralino annihilations in the Milky Way halo. *Astropart. Phys.*, 9:137–162, 1998.

[49] G. Bertone, David G. Cerdeno, J. I. Collar, and Brian C. Odom. WIMP identification through a combined measurement of axial and scalar couplings. *Phys. Rev. Lett.*, 99:151301, 2007.

[50] Gianfranco Bertone, Marco Cirelli, Alessandro Strumia, and Marco Taoso. Gamma-ray and radio tests of the e+e- excess from DM annihilations. *JCAP*, 0903:009, 2009.

[51] M. Boezio et al. First Results from the PAMELA Space Mission. 2008.

[52] S. Boissier and N. Prantzos. Chemo-spectrophotometric evolution of spiral galaxies - 1. The model and the Milky Way. *Mon. Not. Roy. Astron. Soc.*, 307:857–876, 1999.

[53] Michal Brhlik, Daniel J. H. Chung, and Gordon L. Kane. Weighing the universe with accelerators and detectors. *Int. J. Mod. Phys.*, D10:367, 2001.

[54] A. Broadbent, T.C.G. Haslam, and L.J. Osborne. A Detailed Model of the Synchrotron Radiation in the Galactic Disk. *International Cosmic Ray Conference*, 3:229, 1990.

[55] Alessandro Cesarini, Francesco Fucito, Andrea Lionetto, Aldo Morselli, and Piero Ullio. The galactic center as a dark matter gamma-ray source. *Astropart. Phys.*, 21:267–285, 2004.

[56] J. Chang et al. An excess of cosmic ray electrons at energies of 300.800 GeV. *Nature*, 456:362–365, 2008.

[57] Spencer Chang, Aaron Pierce, and Neal Weiner. Momentum Dependent Dark Matter Scattering. *JCAP*, 1001:006, 2010.

[58] Spencer Chang and Neal Weiner. Nonstandard Higgs Decays with Visible and Missing Energy. *JHEP*, 05:074, 2008.

[59] Chuan-Ren Chen, Mihoko M. Nojiri, Fuminobu Takahashi, and T. T. Yanagida. Decaying Hidden Gauge Boson and the PAMELA and ATIC/PPB- BETS Anomalies. *Prog. Theor. Phys.*, 122:553–559, 2009.

[60] Chuan-Ren Chen, Fuminobu Takahashi, and T. T. Yanagida. Gamma rays and positrons from a decaying hidden gauge boson. *Phys. Lett.*, B671:71–76, 2009.

[61] Chuan-Ren Chen, Fuminobu Takahashi, and T. T. Yanagida. High-energy Cosmic-Ray Positrons from Hidden-Gauge-Boson Dark Matter. *Phys. Lett.*, B673:255–259, 2009.

[62] K. S. Cheng, C. Ho, and Malvin A. Ruderman. Energetic Radiation from Rapidly Spinning Pulsars. 1. Outer Magnetosphere Gaps. 2. Vela and Crab. *Astrophys. J.*, 300:500–539, 1986.

[63] X. Chi, E. C. M. Young, and K. S. Cheng. Pulsar-wind origin of cosmic ray positrons. *Astrophys. J.*, 459:L83–L86, 1995.

[64] James Chiang and Roger W. Romani. An Outer gap model of high-energy emission from rotation powered pulsars. 1994.

[65] Ilias Cholis, Douglas P. Finkbeiner, Lisa Goodenough, and Neal Weiner. The PAMELA Positron Excess from Annihilations into a Light Boson. 2008.

[66] Ilias Cholis, Lisa Goodenough, Dan Hooper, Melanie Simet, and Neal Weiner. High Energy Positrons From Annihilating Dark Matter. 2008.

[67] Ilias Cholis, Lisa Goodenough, and Neal Weiner. High Energy Positrons and the WMAP Haze from Exciting Dark Matter. *Phys. Rev.*, D79:123505, 2009.

[68] Marco Cirelli, Mario Kadastik, Martti Raidal, and Alessandro Strumia. Model-independent implications of the e+, e-, anti-proton cosmic ray spectra on properties of Dark Matter. *Nucl. Phys.*, B813:1–21, 2009.

[69] J Clem et al. Solar Modulation of Cosmic Electrons. *Astrophysical Journal*, 464:507, 1996.

[70] Timothy Cohen, David E. Morrissey, and Aaron Pierce. Changes in Dark Matter Properties After Freeze-Out. *Phys. Rev.*, D78:111701, 2008.

[71] Timothy Cohen, Daniel J. Phalen, and Aaron Pierce. On the Correlation Between the Spin-Independent and Spin- Dependent Direct Detection of Dark Matter. 2010.

[72] Daniel T. Cumberbatch, Joe Zuntz, Hans Kristian Kamfjord Eriksen, and Joe Silk. Can the WMAP Haze really be a signature of annihilating neutralino dark matter? 2009.

[73] W. de Boer, C. Sander, V. Zhukov, A. V. Gladyshev, and D. I. Kazakov. The supersymmetric interpretation of the EGRET excess of diffuse Galactic gamma rays. *Phys. Lett.*, B636:13–19, 2006.

[74] T. Delahaye et al. Galactic secondary positron flux at the Earth. *Astron. Astrophys.*, 501:821–833, 2009.

[75] S. Desai et al. Search for dark matter WIMPs using upward through-going muons in Super-Kamiokande. *Phys. Rev.*, D70:083523, 2004.

[76] Jurg Diemand, Michael Kuhlen, and Piero Madau. Dark matter substructure and gamma-ray annihilation in the Milky Way halo. *Astrophys. J.*, 657:262, 2007.

[77] Jurg Diemand, Michael Kuhlen, and Piero Madau. Formation and evolution of galaxy dark matter halos and their substructure. *Astrophys. J.*, 667:859, 2007.

[78] Abdelhak Djouadi, Manuel Drees, and Jean-Loic Kneur. Neutralino dark matter in mSUGRA: Reopening the light Higgs pole window. *Phys. Lett.*, B624:60–69, 2005.

[79] Gregory Dobler, Douglas P. Finkbeiner, Ilias Cholis, Tracy R. Slatyer, and Neal Weiner. The Fermi Haze: A Gamma-Ray Counterpart to the Microwave Haze. 2009.

[80] Scott Dodelson, Dan Hooper, and Pasquale D. Serpico. Extracting the Gamma Ray Signal from Dark Matter Annihilation in the Galactic Center Region. *Phys. Rev.*, D77:063512, 2008.

[81] F. Donato, Nicolao Fornengo, D. Maurin, and P. Salati. Antiprotons in cosmic rays from neutralino annihilation. *Phys. Rev.*, D69:063501, 2004.

[82] F. Donato, D. Maurin, P. Brun, T. Delahaye, and P. Salati. Constraints on WIMP Dark Matter from the High Energy PAMELA $\bar{p}/p$ data. *Phys. Rev. Lett.*, 102:071301, 2009.

[83] Fiorenza Donato, Nicolao Fornengo, David Maurin, Pierre Salati, and Richard Taillet. Cosmic ray antiprotons from relic neutralinos in a diffusion model. 2003.

[84] Manuel Drees and Mihoko M. Nojiri. The Neutralino relic density in minimal $N = 1$ supergravity. *Phys. Rev.*, D47:376–408, 1993.

[85] A. K. Drukier, K. Freese, and D. N. Spergel. Detecting Cold Dark Matter Candidates. *Phys. Rev.*, D33:3495–3508, 1986.

[86] John R. Ellis, Toby Falk, and Keith A. Olive. Neutralino-Stau Coannihilation and the Cosmological Upper Limit on the Mass of the Lightest Supersymmetric Particle. *Phys. Lett.*, B444:367–372, 1998.

[87] John R. Ellis, Toby Falk, Keith A. Olive, and Mark Srednicki. Calculations of neutralino stau coannihilation channels and the cosmologically relevant region of MSSM parameter space. *Astropart. Phys.*, 13:181–213, 2000.

[88] John R. Ellis, Andrew Ferstl, and Keith A. Olive. Re-evaluation of the elastic scattering of supersymmetric dark matter. *Phys. Lett.*, B481:304–314, 2000.

[89] John R. Ellis, Andrew Ferstl, and Keith A. Olive. Exploration of elastic scattering rates for supersymmetric dark matter. *Phys. Rev.*, D63:065016, 2001.

[90] John R. Ellis, Keith A. Olive, and Christopher Savage. Hadronic Uncertainties in the Elastic Scattering of Supersymmetric Dark Matter. *Phys. Rev.*, D77:065026, 2008.

[91] Claude-Andre Faucher-Giguere and Victoria M. Kaspi. Birth and Evolution of Isolated Radio Pulsars. *Astrophys. J.*, 643:332–355, 2006.

[92] Douglas P. Finkbeiner. Microwave ISM Emission Observed by WMAP. *Astrophys. J.*, 614:186–193, 2004.

[93] Douglas P. Finkbeiner. WMAP microwave emission interpreted as dark matter annihilation in the inner Galaxy. 2004.

[94] N. Fornengo, L. Pieri, and S. Scopel. Neutralino annihilation into gamma-rays in the Milky Way and in external galaxies. *Phys. Rev.*, D70:103529, 2004.

[95] Patrick J. Fox and Erich Poppitz. Leptophilic Dark Matter. *Phys. Rev.*, D79:083528, 2009.

[96] Daniel Z. Freedman, David N. Schramm, and David L. Tubbs. The Weak Neutral Current and Its Effects in Stellar Collapse. *Ann. Rev. Nucl. Part. Sci.*, 27:167–207, 1977.

[97] R. J. Gaitskell. Direct detection of dark matter. *Ann. Rev. Nucl. Part. Sci.*, 54:315–359, 2004.

[98] Graciela B. Gelmini and Paolo Gondolo. Neutralino with the right cold dark matter abundance in (almost) any supersymmetric model. *Phys. Rev.*, D74:023510, 2006.

[99] Gianfranco Gentile, P. Salucci, U. Klein, D. Vergani, and P. Kalberla. The cored distribution of dark matter in spiral galaxies. *Mon. Not. Roy. Astron. Soc.*, 351:903, 2004.

[100] C. Ghisellini, P.W. Guilbert, and R. Svensson. The Synchrotron Boiler. *Astrophys. J.*, 334:L5, 1988.

[101] Joel Giedt, Anthony W. Thomas, and Ross D. Young. Dark matter, the CMSSM and lattice QCD. 2009.

[102] G. F. Giudice and A. Romanino. Split supersymmetry. *Nucl. Phys.*, B699:65–89, 2004.

[103] Gian F. Giudice, Markus A. Luty, Hitoshi Murayama, and Riccardo Rattazzi. Gaugino Mass without Singlets. *JHEP*, 12:027, 1998.

[104] Gian Francesco Giudice, Edward W. Kolb, and Antonio Riotto. Largest temperature of the radiation era and its cosmological implications. *Phys. Rev.*, D64:023508, 2001.

[105] P. Gondolo et al. DarkSUSY: Computing supersymmetric dark matter properties numerically. *JCAP*, 0407:008, 2004.

[106] P. Gondolo et al. DarkSUSY 4.00 neutralino dark matter made easy. *New Astron. Rev.*, 49:149–151, 2005.

[107] Mark W. Goodman and Edward Witten. Detectability of certain dark-matter candidates. *Phys. Rev.*, D31:3059, 1985.

[108] Phill Grajek, Gordon Kane, Dan Phalen, Aaron Pierce, and Scott Watson. Is the PAMELA Positron Excess Winos? *Phys. Rev.*, D79:043506, 2009.

[109] Phill Grajek, Gordon Kane, Daniel J. Phalen, Aaron Pierce, and Scott Watson. Neutralino Dark Matter from Indirect Detection Revisited. 2008.

[110] Kim Griest and David Seckel. Three exceptions in the calculation of relic abundances. *Phys. Rev.*, D43:3191–3203, 1991.

[111] Howard E. Haber and Gordon L. Kane. The Search for Supersymmetry: Probing Physics Beyond the Standard Model. *Phys. Rept.*, 117:75–263, 1985.

[112] Lawrence J. Hall, Karsten Jedamzik, John March-Russell, and Stephen M. West. Freeze-In Production of FIMP Dark Matter. 2009.

[113] Lawrence J. Hall, Hitoshi Murayama, and Neal Weiner. Neutrino mass anarchy. *Phys. Rev. Lett.*, 84:2572–2575, 2000.

[114] Koichi Hamaguchi, Satoshi Shirai, and T. T. Yanagida. Cosmic Ray Positron and Electron Excess from Hidden- Fermion Dark Matter Decays. *Phys. Lett.*, B673:247–250, 2009.

[115] Jin-Lin Han. Magnetic fields in our Galaxy: How much do we know? III. Progress in the last decade. 2006.

[116] Roni Harnik and Graham D. Kribs. An Effective Theory of Dirac Dark Matter. *Phys. Rev.*, D79:095007, 2009.

[117] C. G. T. Haslam, U. Klein, C. J. Salter, H. Stoffel, W. E. Wilson, M. N. Cleary, D. J. Cooke, and P. Thomasson. A 408 MHz all-sky continuum survey. I - Observations at southern declinations and for the North Polar region. *Astronomy and Astrophysics*, 100:209–219, July 1981.

[118] Junji Hisano, Masahiro Kawasaki, Kazunori Kohri, and Kazunori Nakayama. Neutrino Signals from Annihilating/Decaying Dark Matter in the Light of Recent Measurements of Cosmic Ray Electron/Positron Fluxes. *Phys. Rev.*, D79:043516, 2009.

[119] Junji Hisano, Kazunori Nakayama, and Masato Yamanaka. Implications of CDMS II result on Higgs sector in the MSSM. 2009.

[120] Morihiro Honda, T. Kajita, K. Kasahara, S. Midorikawa, and T. Sanuki. Calculation of atmospheric neutrino flux using the interaction model calibrated with atmospheric muon data. *Phys. Rev.*, D75:043006, 2007.

[121] Dan Hooper. Constraining Supersymmetric Dark Matter With Synchrotron Measurements. *Phys. Rev.*, D77:123523, 2008.

[122] Dan Hooper and Edward A. Baltz. Strategies for Determining the Nature of Dark Matter. *Ann. Rev. Nucl. Part. Sci.*, 58:293–314, 2008.

[123] Dan Hooper, Pasquale Blasi, and Pasquale Dario Serpico. Pulsars as the Sources of High Energy Cosmic Ray Positrons. *JCAP*, 0901:025, 2009.

[124] Dan Hooper and Brenda L. Dingus. Limits on supersymmetric dark matter from EGRET observations of the galactic center region. *Phys. Rev.*, D70:113007, 2004.

[125] Dan Hooper, Douglas P. Finkbeiner, and Gregory Dobler. Evidence Of Dark Matter Annihilations In The WMAP Haze. *Phys. Rev.*, D76:083012, 2007.

[126] Dan Hooper, Albert Stebbins, and Kathryn M. Zurek. Excesses in cosmic ray positron and electron spectra from a nearby clump of neutralino dark matter. *Phys. Rev.*, D79:103513, 2009.

[127] Alejandro Ibarra and David Tran. Decaying Dark Matter and the PAMELA Anomaly. *JCAP*, 0902:021, 2009.

[128] Koji Ishiwata, Shigeki Matsumoto, and Takeo Moroi. Cosmic-Ray Positron from Superparticle Dark Matter and the PAMELA Anomaly. *Phys. Lett.*, B675:446–449, 2009.

[129] Karsten Jedamzik. Did something decay, evaporate, or annihilate during big bang nucleosynthesis? *Phys. Rev.*, D70:063524, 2004.

[130] Karsten Jedamzik, Ki-Young Choi, Leszek Roszkowski, and Roberto Ruiz de Austri. Solving the cosmic lithium problems with gravitino dark matter in the CMSSM. *JCAP*, 0607:007, 2006.

[131] Tesla Jeltema. Searches for Dark Matter Annihilation in Dwarf Spheroidal Galaxies with Fermi. *Talk at TeVPA*, 2009.

[132] Gerard Jungman, Marc Kamionkowski, and Kim Griest. Supersymmetric dark matter. *Phys. Rept.*, 267:195–373, 1996.

[133] Marc Kamionkowski and Michael S. Turner. THERMAL RELICS: DO WE KNOW THEIR ABUNDANCES? *Phys. Rev.*, D42:3310–3320, 1990.

[134] Gordon Kane, Ran Lu, and Scott Watson. PAMELA Satellite Data as a Signal of Non-Thermal Wino LSP Dark Matter. *Phys. Lett.*, B681:151–160, 2009.

[135] Gordon Kane and Scott Watson. Dark Matter and LHC: What is the Connection? *Mod. Phys. Lett.*, A23:2103–2123, 2008.

[136] Gordon L. Kane, Lian-Tao Wang, and Ting T. Wang. Supersymmetry and the cosmic ray positron excess. *Phys. Lett.*, B536:263–269, 2002.

[137] Gordon L. Kane, Lian-Tao Wang, and James D. Wells. Supersymmetry and the positron excess in cosmic rays. *Phys. Rev.*, D65:057701, 2002.

[138] David E. Kaplan, Markus A. Luty, and Kathryn M. Zurek. Asymmetric Dark Matter. *Phys. Rev.*, D79:115016, 2009.

[139] Manoj Kaplinghat, Daniel J. Phalen, and Kathryn M. Zurek. Pulsars as the Source of the WMAP Haze. *JCAP*, 0912:010, 2009.

[140] Boaz Katz, Kfir Blum, and Eli Waxman. What can we really learn from positron flux 'anomalies'? 2009.

[141] Ryuichiro Kitano and Yasunori Nomura. A solution to the supersymmetric fine-tuning problem within the MSSM. *Phys. Lett.*, B631:58–67, 2005.

[142] Ryuichiro Kitano and Yasunori Nomura. Dark matter before the LHC in a natural supersymmetric standard model. *Phys. Lett.*, B632:162–166, 2006.

[143] Edward W. Kolb and Michael S. Turner. The Early universe. *Front. Phys.*, 69:1–547, 1990.

[144] E. Komatsu et al. Five-Year Wilkinson Microwave Anisotropy Probe (WMAP) Observations:Cosmological Interpretation. *Astrophys. J. Suppl.*, 180:330–376, 2009.

[145] T. N. LaRosa et al. Evidence for a Weak Galactic Center Magnetic Field from Diffuse Low Frequency Nonthermal Radio Emission. *Astrophys. J.*, 626:L23–L28, 2005.

[146] J. Lavalle, Q. Yuan, D. Maurin, and X. J. Bi. Full Calculation of Clumpiness Boost factors for Antimatter Cosmic Rays in the light of ΛCDM N-body simulation results. 2007.

[147] Benjamin W. Lee and Steven Weinberg. Cosmological lower bound on heavy-neutrino masses. *Phys. Rev. Lett.*, 39:165–168, 1977.

[148] H. S Lee. et al. Limits on WIMP-nucleon cross section with CsI(Tl) crystal detectors. *Phys. Rev. Lett.*, 99:091301, 2007.

[149] Ilan Levine. *Private Communication*, 2009.

[150] Ilan Levine. The COUPP Dark Matter Search Experiment. *Talk at DPF*, 2009.

[151] Jia Liu, Peng-fei Yin, and Shou-hua Zhu. Prospects for Detecting Neutrino Signals from Annihilating/Decaying Dark Matter to Account for the PAMELA and ATIC results. *Phys. Rev.*, D79:063522, 2009.

[152] D. R. Lorimer et al. The Parkes multibeam pulsar survey: VI. Discovery and timing of 142 pulsars and a Galactic population analysis. *Mon. Not. Roy. Astron. Soc.*, 372:777–800, 2006.

[153] Gregory D. Mack, Thomas D. Jacques, John F. Beacom, Nicole F. Bell, and Hasan Yuksel. Conservative Constraints on Dark Matter Annihilation into Gamma Rays. *Phys. Rev.*, D78:063542, 2008.

[154] T. Maeno et al. Successive measurements of cosmic-ray antiproton spectrum in a positive phase of the solar cycle. *Astropart. Phys.*, 16:121–128, 2001.

[155] Rakhi Mahbubani and Leonardo Senatore. The minimal model for dark matter and unification. *Phys. Rev.*, D73:043510, 2006.

[156] Fabio Maltoni and Tim Stelzer. MadEvent: Automatic event generation with MadGraph. *JHEP*, 02:027, 2003.

[157] Dmitry Malyshev, Ilias Cholis, and Joseph Gelfand. Pulsars versus Dark Matter Interpretation of ATIC/PAMELA. *Phys. Rev.*, D80:063005, 2009.

[158] Vuk Mandic, Aaron Pierce, Paolo Gondolo, and Hitoshi Murayama. The Lower bound on the neutralino nucleon cross-section. 2000.

[159] Michelangelo L. Mangano, Mauro Moretti, Fulvio Piccinini, Roberto Pittau, and Antonio D. Polosa. ALPGEN, a generator for hard multiparton processes in hadronic collisions. *JHEP*, 07:001, 2003.

[160] Stephen P. Martin. A Supersymmetry Primer. 1997.

[161] Antonio Masiero, Stefano Profumo, and Piero Ullio. Neutralino dark matter detection in split supersymmetry scenarios. *Nucl. Phys.*, B712:86–114, 2005.

[162] H. A. Mayer-Hasselwander et al. High-energy gamma ray emission from the galactic center. *Astron. Astrophys.*, 335:161–172, 1998.

[163] Patrick Meade, Michele Papucci, and Tomer Volansky. Dark Matter Sees The Light. 2009.

[164] David Merritt, Julio F. Navarro, Aaron Ludlow, and Adrian Jenkins. A Universal Density Profile for Dark and Luminous Matter? *Astrophys. J.*, 624:L85–L88, 2005.

[165] Takeo Moroi and Lisa Randall. Wino cold dark matter from anomaly-mediated SUSY breaking. *Nucl. Phys.*, B570:455–472, 2000.

[166] Aldo Morselli. Search for dark matter in the sky. *AIP Conf. Proc.*, 1178:83–89, 2009.

[167] I. V. Moskalenko and A. W. Strong. Production and propagation of cosmic-ray positrons and electrons. *Astrophys. J.*, 493:694–707, 1998.

[168] Igor Moskalenko. Private Communication.

[169] Igor V. Moskalenko, S. W. Digel, T. A. Porter, O. Reimer, and A. W. Strong. Understanding limitations in the determination of the diffuse Galactic gamma-ray emission. *Nucl. Phys. Proc. Suppl.*, 173:44–47, 2007.

[170] Igor V. Moskalenko, Troy A. Porter, and Andrew W. Strong. Attenuation of VHE gamma rays by the Milky Way interstellar radiation field. *Astrophys. J.*, 640:L155–L158, 2006.

[171] Emmanuel Moulin, F. Mayet, and D. Santos. Supersymmetric dark matter search via spin-dependent interaction with He-3. *Phys. Lett.*, B614:143–154, 2005.

[172] Julio F. Navarro et al. The Diversity and Similarity of Cold Dark Matter Halos. 2008.

[173] Julio F. Navarro, Carlos S. Frenk, and Simon D. M. White. A Universal Density Profile from Hierarchical Clustering. *Astrophys. J.*, 490:493–508, 1997.

[174] Ann E. Nelson and Christopher Spitzer. Slightly Non-Minimal Dark Matter in PAMELA and ATIC. 2008.

[175] Yasunori Nomura and Jesse Thaler. Dark Matter through the Axion Portal. *Phys. Rev.*, D79:075008, 2009.

[176] J. Olzem, H. Gast, and S. Schael. Cosmic-ray positron identification through bremsstrahlung conversion. *Nucl. Phys. Proc. Suppl.*, 173:51–55, 2007.

[177] Jan Olzem. Signatures of SUSY dark matter at the LHC and in the spectra of cosmic rays. 2007.

[178] S. Orito et al. Precision measurement of cosmic-ray antiproton spectrum. *Phys. Rev. Lett.*, 84:1078–1081, 2000.

[179] B. Paczynski. A Test of the Galactic Origin of Gamma-Ray Bursts. *Astrophys. J.*, 348:485, 1990.

[180] Michael Edward Peskin and James Daniel Wells. How can a heavy Higgs boson be consistent with the precision electroweak measurements? *Phys. Rev.*, D64:093003, 2001.

[181] Daniel J. Phalen, Aaron Pierce, and Neal Weiner. Cosmic Ray Positrons from Annihilations into a New, Heavy Lepton. *Phys. Rev.*, D80:063513, 2009.

[182] Eduardo Ponton and Lisa Randall. TeV Scale Singlet Dark Matter. *JHEP*, 04:080, 2009.

[183] Troy A. Porter and A. W. Strong. A new estimate of the Galactic interstellar radiation field between 0.1 microns and 1000 microns. 2005.

[184] Maxim Pospelov and Adam Ritz. Astrophysical Signatures of Secluded Dark Matter. *Phys. Lett.*, B671:391–397, 2009.

[185] M.S. Potgieter, R.A. Burger, and S.E.S. Ferreira. Modulation of Cosmic Rays in the Heliosphere From Solar Minimum to Maximum:a Theoretical Perspective. *Space Sci. Rev.*, 97:295–307, 2001.

[186] Stefano Profumo. Dissecting Pamela (and ATIC) with Occam's Razor: existing, well-known Pulsars naturally account for the 'anomalous' Cosmic-Ray Electron and Positron Data. 2008.

[187] Stefano Profumo and Tesla E. Jeltema. Extragalactic Inverse Compton Light from Dark Matter Annihilation and the Pamela Positron Excess. *JCAP*, 0907:020, 2009.

[188] Stefano Profumo and Piero Ullio. The role of antimatter searches in the hunt for supersymmetric dark matter. *JCAP*, 0407:006, 2004.

[189] V. S. Ptuskin, Igor V. Moskalenko, F. C. Jones, A. W. Strong, and V. N. Zirakashvili. Dissipation of Magnetohydrodynamic Waves on Energetic Particles: Impact on Interstellar Turbulence and Cosmic Ray Transport. *Astrophys. J.*, 642:902–916, 2006.

[190] Georg G. Raffelt. Supernova neutrino observations: What can we learn? 2007.

[191] Lisa Randall and Raman Sundrum. Out of this world supersymmetry breaking. *Nucl. Phys.*, B557:79–118, 1999.

[192] Marco Regis and Piero Ullio. Multi-wavelength signals of dark matter annihilations at the Galactic center. *Phys. Rev.*, D78:043505, 2008.

[193] Leszek Roszkowski, Roberto Ruiz de Austri, and Takeshi Nihei. New cosmological and experimental constraints on the CMSSM. *JHEP*, 08:024, 2001.

[194] Vera C. Rubin and W. Kent Ford, Jr. Rotation of the Andromeda Nebula from a Spectroscopic Survey of Emission Regions. *Astrophys. J.*, 159:379–403, 1970.

[195] Robert J. Scherrer and Michael S. Turner. On the Relic, Cosmic Abundance of Stable Weakly Interacting Massive Particles. *Phys. Rev.*, D33:1585, 1986.

[196] David J. Schlegel, Douglas P. Finkbeiner, and Marc Davis. Maps of Dust IR Emission for Use in Estimation of Reddening and CMBR Foregrounds. *Astrophys. J.*, 500:525, 1998.

[197] E. S. Seo and V. S. Ptuskin. Stochiastic Reacceleration of Cosmic Rays in Interstellar medium. *Astrophys. J.*, 431:705, 1994.

[198] Geraldine Servant and Timothy M. P. Tait. Elastic scattering and direct detection of Kaluza-Klein dark matter. *New J. Phys.*, 4:99, 2002.

[199] Mikhail A. Shifman, A. I. Vainshtein, and Valentin I. Zakharov. Remarks on Higgs Boson Interactions with Nucleons. *Phys. Lett.*, B78:443, 1978.

[200] Torbjorn Sjostrand, Stephen Mrenna, and Peter Skands. PYTHIA 6.4 Physics and Manual. *JHEP*, 05:026, 2006.

[201] Tracy R. Slatyer, Nikhil Padmanabhan, and Douglas P. Finkbeiner. CMB Constraints on WIMP Annihilation: Energy Absorption During the Recombination Epoch. *Phys. Rev.*, D80:043526, 2009.

[202] D. N. Spergel et al. First Year Wilkinson Microwave Anisotropy Probe (WMAP) Observations: Determination of Cosmological Parameters. *Astrophys. J. Suppl.*, 148:175–194, 2003.

[203] Volker Springel et al. The Aquarius Project: the subhalos of galactic halos. *Mon. Not. Roy. Astron. Soc.*, 391:1685–1711, 2008.

[204] F. W. Stecker, S. D. Hunter, and D. A. Kniffen. The Likely Cause of the EGRET GeV Anomaly and its Implications. *Astropart. Phys.*, 29:25–29, 2008.

[205] A. W. Strong and I. V. Moskalenko. Propagation of cosmic-ray nucleons in the Galaxy. *Astrophys. J.*, 509:212–228, 1998.

[206] A. W. Strong and I. V. Moskalenko. Galactic cosmic rays & gamma rays: a synthesis. 1999.

[207] Andrew W. Strong, Igor V. Moskalenko, and Vladimir S. Ptuskin. Cosmic-ray propagation and interactions in the Galaxy. *Ann. Rev. Nucl. Part. Sci.*, 57:285–327, 2007.

[208] Andrew W. Strong, Igor V. Moskalenko, and Olaf Reimer. Diffuse continuum gamma rays from the Galaxy. *Astrophys. J.*, 537:763–784, 2000.

[209] Andrew W. Strong, Igor V. Moskalenko, and Olaf Reimer. Diffuse Galactic continuum gamma rays. A model compatible with EGRET data and cosmic-ray measurements. *Astrophys. J.*, 613:962–976, 2004.

[210] S.J. Sturner and C.D. Dermer. 'Statistical Analysis of Gamma-Ray Properties of Rotation-powered Pulsars. *Astrophys. J.*, 461:872, 1996.

[211] Scott D. Thomas and James D. Wells. Phenomenology of Massive Vectorlike Doublet Leptons. *Phys. Rev. Lett.*, 81:34–37, 1998.

[212] S. Torii et al. High-energy electron observations by PPB-BETS flight in Antarctica. 2008.

[213] D. Walsh, R. F. Carswell, and R. J. Weymann. 0957 + 561 A, B - Twin quasistellar objects or gravitational lens. *Nature*, 279:381–384, 1979.

[214] James D. Wells. PeV-scale supersymmetry. *Phys. Rev.*, D71:015013, 2005.

[215] Christopher Wiebusch et al. Physics Capabilities of the IceCube DeepCore Detector. 2009.

[216] W. M. Yao et al. Review of particle physics. *J. Phys.*, G33:1–1232, 2006.

[217] Peng-fei Yin et al. PAMELA data and leptonically decaying dark matter. *Phys. Rev.*, D79:023512, 2009.

[218] Hasan Yuksel, Matthew D. Kistler, and Todor Stanev. TeV Gamma Rays from Geminga and the Origin of the GeV Positron Excess. *Phys. Rev. Lett.*, 103:051101, 2009.

[219] Juan Zhang et al. Discriminating different scenarios to account for the cosmic e + /- excess by synchrotron and inverse Compton radiation. *Phys. Rev.*, D80:023007, 2009.

[220] L. Zhang and K.S. Chang. High-Energy Radiation from Rapidly Spinning Pulsars with Thick Outer Gaps. *Astrophys. J.*, 487:370, 1997.

[221] L. Zhang and K. S. Cheng. Cosmic-ray positrons from mature gamma-ray pulsars. *Astron. Astrophys.*, 368:1063, 2001.

[222] L. Zhang, K. S. Cheng, Ze-Jun Jiang, and P. Leung. Gamma-ray Luminosity and Death Lines of Pulsars with Outer Gaps. *Astrophys. J.*, 604:317–327, 2004.

[223] V.N. Zirakashvili et al. Magnetohydrodynamic wind driven by cosmic rays in a rotating galaxy. *Astronomy and Astrophysics*, 311:113, 1996.

[224] F. Zwicky. Spectral displacement of extra galactic nebulae. *Helv. Phys. Acta*, 6:110–127, 1933.